THE EFFECT OF POST WELD HEAT TREATMENT ON THE CORROSION BEHAVIOUR OF A AA2050T34-FSW

By ALESSANDRO FENDONI

A thesis submitted to
The University of Birmingham
for the degree of
MRes in Science and Engineering of Materials

School of Metallurgy and Materials
University of Birmingham
October 2009

Acknowledgements

This work was sponsored by Alcan Centre de Recherches de Voreppe and University of Birmingham.

Firstly I would like to thank my supervisor Dr. A. J. Davenport for providing valuable support and constant ecouragement.

Special thanks to Christine Henon at Alcan Centre de Recherches de Voreppe for her assitance and precious advices.

Many thanks to everyone in the electrochemistry laboratory.

I’m finally grateful to my family for the constant support.

CONTENTS

CHAPTER 1 - Introduction

In the 1970s, the increase in fuel costs and the consequent interest in the development of fuel efficiency and high-performance aircraft produced a strong interest in materials with low weight and high specific proprieties. Among the candidate materials, aluminium-lithium appeared attractive, since lithium addition to aluminium alloys simultaneously increased the Young's modulus and decreased density without compromising toughness and corrosion resistance. In some applications, these alloys have been used in place of traditional high strength alloys of the 2xxx and 7xxx series with the advantage that components can be produced with the same technologies. This advantage makes Al-Li alloys very competitive compared with new materials, such as fibre-reinforced composites, which are still characterized by high production costs.

The first two generations of Al-Li alloys, have encountered technical problems, particularly their poor fracture toughness and the excessive anisotropy of mechanical proprieties. A third generation with lower lithium content and with the addition of other elements has been developed and employed in important applications. Alloy AA2195 replaced AA2219 and enabled a 3400 kg weight reduction on the 34500 kg tank of the space shuttle (Fig. 1.1). Considering that the cost of launching payloads into low Earth orbit has been estimated to be approximately $US8000 per kg [1], this allows a saving of millions of dollars. There is a strong interest in a further development of this new generation of Al-Li alloys, in order to find an increasing number of applications where, these low-density materials, may successfully replace traditional alloys, thanks to their higher specific mechanical proprieties and superior crack growth resistance.

Fig. 1.1 Space Shuttle Super Light External Fuel Tank (SLWT) [2]

Friction Stir Welding (FSW) is a relatively new solid state joining process that has been successfully used to weld highly alloyed 2xxx and 7xxx aluminium alloys, which are considered non-weldable through conventional welding techniques. Being a solid-state process, FSW produces virtually defect-free welds, therefore the properties of the metal in the joined area are better than those from fusion welding and distortions are minimized. Nevertheless the heat input and plastic deformation that the welding region is subjected to lead to a modification in microstructure and, therefore, a change in the corrosion behaviour must be expected. FSW is an important improvement in aluminium manufacturing technology and a further contribution to weight saving in aerospace application, through the elimination of weld wire filler or

mechanically fastened structures.

Despite the increasing interest in developing the third generation of Al-Li alloys to obtain high strength and high toughness, and the successful application of the FSW process to aluminium alloys containing lithium, to date relatively little research has been conducted on the corrosion behaviour of Al-Cu-Li FSW, which is still far being completely understood.

The main aim of this work has been to contribute to the understanding of the post weld ageing treatment on the corrosion behaviour of FSW AA2050-T34. Five different ageing conditions have been evaluated using polarization techniques and immersion tests in different chloride containing solutions.

CHAPTER 2 – Literature Review

2.4. Metallurgy of aluminium alloys containing lithium

Since the early 1920s, aluminium alloys have been the primary material in the aircraft industry, owing to a combination of properties including low density, corrosion resistance, ductility and specific strength and stiffness [3-5].

In aircraft design, weight saving, associated with fuel efficiency, represents an important contributor in the improvement of the performance and the reduction of operating costs. For these reasons, low density Al-Li alloys are very attractive to the aerospace industry [6, 7]. In many applications, Al-Li alloys have replaced conventional alloys of the 2xxx and 7xxx series, without additional costs, owing to the fact that they can be produced by the same technologies.

Li is the lightest metallic element, with a density of 0.54 g/cm^3; it has a high solid solubility in aluminium, with a maximum of approximately 4% wt. at 610°C. In aluminium alloys, lithium simultaneously increases the elastic modulus and decreases the density: each 1% of Li reduces alloy density by about 3% and increases Young's modulus by about 6% [1].

AA2020 (Al-4%Cu-1.1%Li-0.5%Mn-0.2%Cd), produced in the United States in the 1950s, was the first aluminium alloy containing lithium (first generation of Al-Li alloys). The production of this alloy was abandoned because of the low-tensile elongation and the poor fracture toughness.

A second generation of Al-Li alloys was developed in order to improve the properties of the previous one (grade 01420 for the system Al-Li-Mg, grade AA2090, AA2091 and AA8090 for the system Al-Li-Cu-Mg). Grade 01420 was highly corrosion resistant but with moderate strength; grades AA2090, AA2091 and AA8090 showed better properties than AA2020 but still suffered from excessive anisotropy of mechanical properties and a low stress-corrosion threshold.

Recently, a third generation of Al-Li alloys has been developed for military and aerospace applications, with lower Li/Cu ratios compared with the previous generation. The first grade was the ultra-high strength alloy Weldalite 049®, Al-(4.5-6.3)%Cu-1.3%Li-0.4%Mg-0.4%Ag-0.14%Zr. Similar to this alloy, but with a lower copper content, is AA2195 (Al-4%Cu-1Li-0.5%Mg-0.4%Ag-0.1%Zr). This alloy has been used for the U.S. Space Shuttle Super-Light external fuel tank [8]. Other recent grades of the third generation of Al-Li alloys are AA2094, AA2096, AA2097, AA2099, AA2196, AA2197, AA2198 and AA2050. These alloys belong to the Al-Cu-Li-(Mg)-(Ag)-Zr system. Compared with the traditional aluminium alloys used in aircraft applications they show higher static strength and damage tolerance [9].

2.4.5. Metallurgy of Al-Li alloys

Aluminium alloys containing lithium are heat treatable: strength can be increased by solution heat treatment and subsequent ageing treatment. Alloys of the Al-Li-X system have complex precipitation sequences of several metastable phases. The heat treatment involves three main steps:

- Solution treatment at high temperature to dissolve the alloying elements and obtain a single-phase
- Quenching to obtain a super-saturated solid solution (SSSS)
- Decomposition of the SSSS with an ageing treatment

Depending on the alloy composition, the precipitation sequence during ageing can involve the formation of several phases; the precipitation of the equilibrium phases is preceded by the formation of Guiner-Preston (GP) zones and intermediate precipitates. GP zones are ordered solute-rich groups of atoms that are a few atom planes in thickness and are coherent with the matrix.

In binary AlLi alloys, the precipitation sequence has been shown to be [10]:

SSSS → δ' (Al_3Li) → δ (AlLi)

Al-Li alloys are strengthened by the precipitation of spherical δ' (Al_3Li)

particles, that preferentially nucleate at dislocations [11]. The spherical shape is due to the similar crystallographic parameters and small lattice mis-match between the matrix and the δ' phase, which is coherent with the matrix, and is shearable by dislocations. During plastic straining, crystallographic slip tends to concentrate on a few planes and the resulting strain localization leads to low ductility and fracture toughness of this alloy [12].

During artificial ageing, coarsening of δ' particles is accompanied by two other phenomena:

- Precipitation of equilibrium δ (AlLi) particles

  These particles are reported to precipitate at grain boundaries for lower ageing temperatures and in the matrix on dislocations at higher temperatures [13]. Embrittlement of this alloy and stress corrosion cracking susceptibility is also associated with this equilibrium phase [14, 15].
- Formation of Precipitate Free Zones (PFZ) along the grain boundaries [16, 17].

  The growth of PFZs occurs by a solute depletion mechanism [17], and the solute is consumed during the growth of equilibrium δ phase at the grain boundaries.

  Since these regions are weaker than the matrix they can lead to strain localization.

Increasing the ageing time leads to the coarsening of precipitates, while an increase in lithium in the alloy leads to an increase in volume fraction of δ' [18, 19]. The presence of δ' phase and PFZ are shown in Fig. 2.1 for an Al-2.4%Li alloy that has been aged for 1 week at 200 °C.

The presence of shearable precipitates (δ') and precipitates at the grain boundary (δ) with associated PFZs make this alloy brittle and susceptible to Stress Corrosion Cracking (SCC). For these reasons, binary Al-Li alloys and some ternary alloys Al-Li-X (like Al-Cu-Li alloy AA2020) have not found commercial use and other alloying elements are generally added in order to modify type and sequence of precipitates.

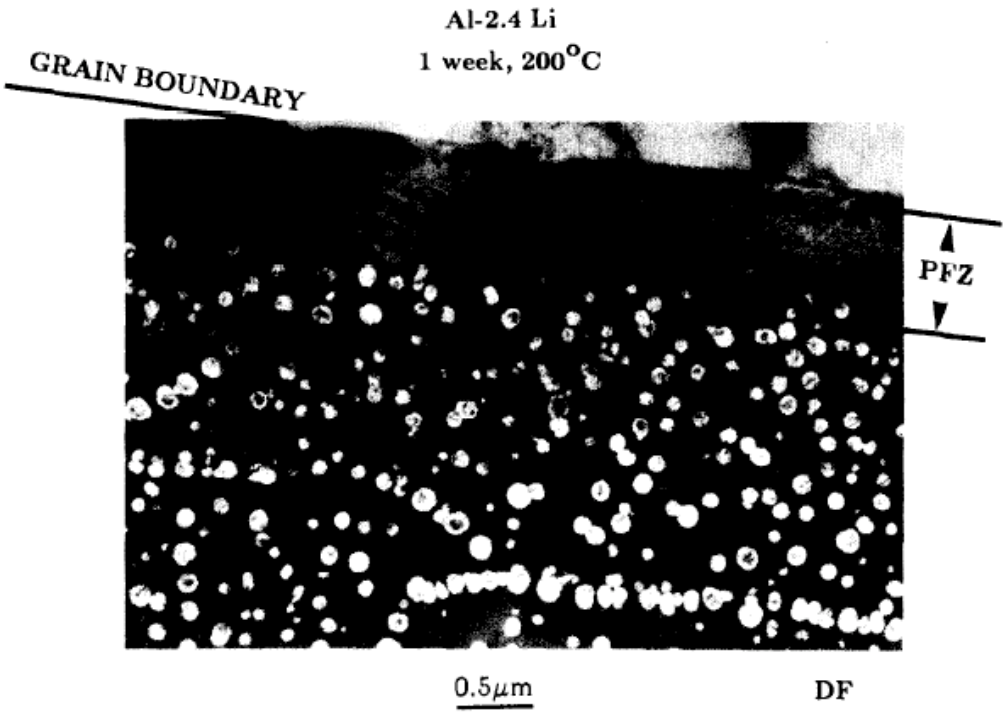

Fig. 2.1 TEM micrograph showing the presence of a grain boundary PFZ and large δ' associated with dislocation in Al-2.4%Li alloy, aged for 1 week at 200 °C [19].

2.1.3. Metallurgy of Al-Li-X systems

The addition of elements to the Al-Li system leads to the following effects [20]:

- Formation of new strengthening precipitates
- Formation of co-precipitates with δ' phase
- Formation of dispersoids that control recrystallization and thus grain size

The precipitation sequences of Al-Li-X systems are quite complex. The various phases that can be found are shown in Fig. 2.2 [21].

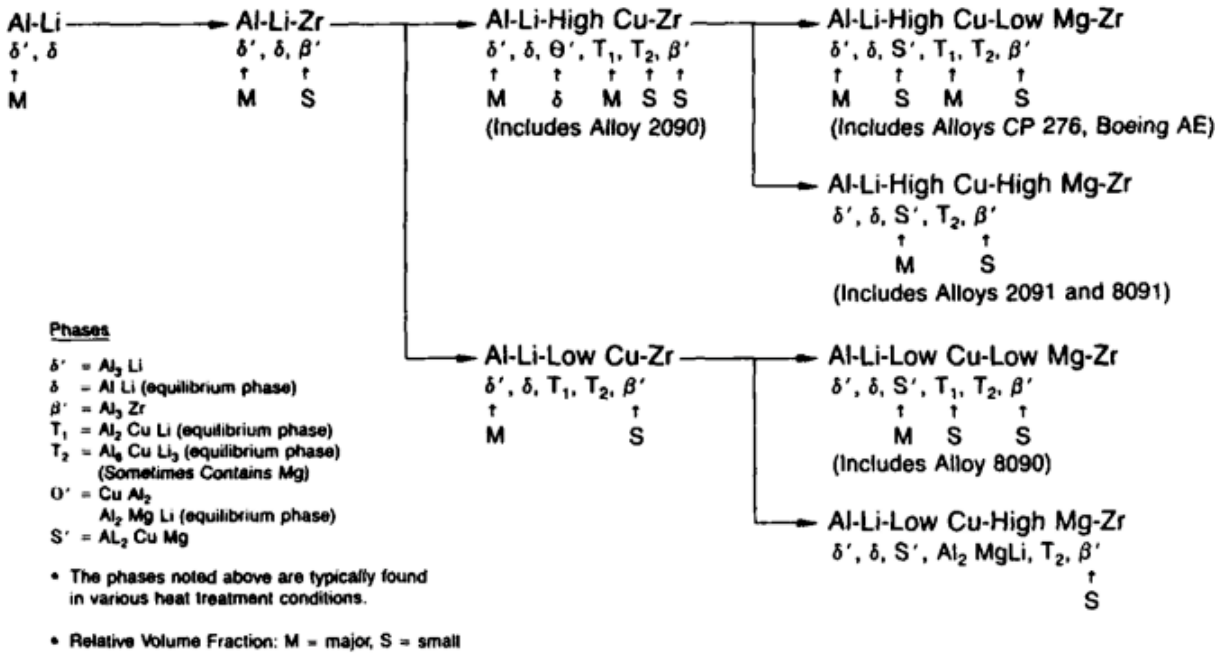

Fig. 2.2 Schematic illustration of the precipitate phases in Al-Li-X system [21]

2.1.4. Al-Li-Cu system

The effect of copper is to reduce the lithium solubility and promote δ' precipitation and co-precipitation of other phases such G.P. zones and θ' (Al_2Cu). The precipitation sequence of this system is a function of the Li/Cu ratio.

For the Al-Li-Cu system, the precipitation follows the sequence [10]:

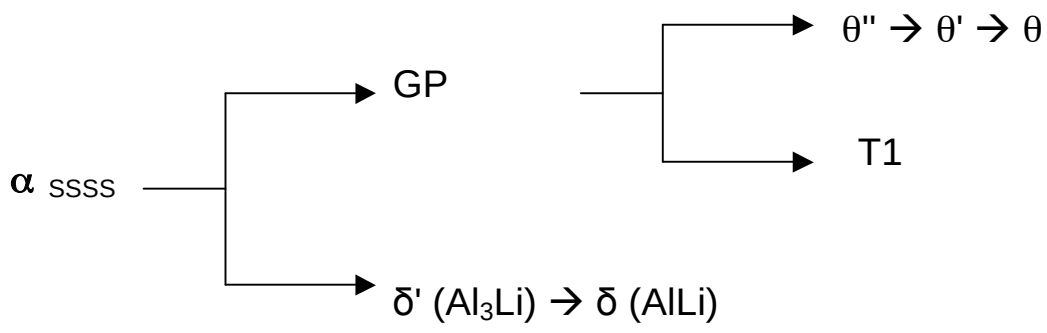

During the ageing treatment of Al-Li-Cu commercial alloys, the first precipitate to form is δ' followed by θ' and T1 (Al_2LiCu). The precipitation of the last two phases reduces the volume fraction of δ'. The reduction of volume fraction of δ' has a beneficial effect on the degree of strain concentration [12]. In AA2090, based on this system, the equilibrium phase T1 is reported to be the predominant strengthening precipitate and the metastable phase θ' (the primary strengthening phase in the system Al-Cu) may also be present [21].

2.1.5. Al-Li-Cu-Mg system

Magnesium reduces the solubility of lithium in aluminium at all temperatures [10]. Commercial alloys of this system are AA2091, AA8090 and AA8091. These alloys are strengthening by the co-precipitation of T1 and S' (Al_2MgCu). The Mg addition in Al-Cu-Li alloys is therefore beneficial in terms of density reduction and strength improvement.

The strengthening phases observed in this system, for different alloy compositions, were identified by Flower and Gregson [22]. The metastable phase composition for the Al-Cu-Mg system containing 2-3%Li is shown in Fig. 2.3 When the Mg/Cu ratio is increased, S' is the dominant precipitate, followed by δ' and small amount of T1 [23]. When the concentration of magnesium exceeds the copper concentration, Al_2MgLi may precipitate in addition to the S' phase [21].

The nucleation of T1 and S' is difficult and preferentially occurs at dislocations. For this reason, commercial alloys in this system are normally used in the T8 temper (cold worked before ageing) [1].

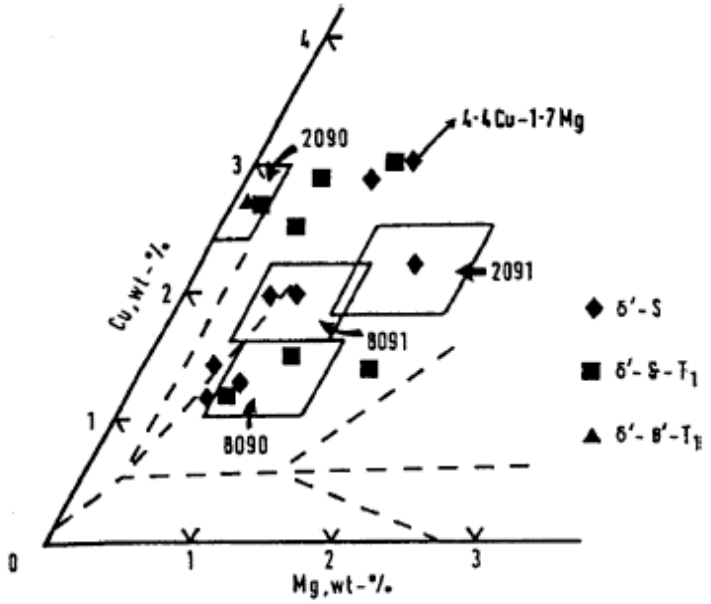

Fig. 2.3 Precipitate phases reported in Al-Cu-Mg-Li alloys on ageing at 190ºC [23]

2.1.6. Al-Cu-Li-Mg-Ag-Zr system

The third generation of aluminium alloys containing lithium, corresponding to the Al-Cu-Li-Mg-Ag-Zr system, has been developed in the last 20 years.

The microstructure and hardness of Al-4.0%Cu-0.3%Mg-0.4%Ag, with progressive addition of Li in the range of 0% to 2.5%, aged at 200°C, was studied by Polmear and Chester [24]. The alloy with 1% Li showed a higher age hardening level, owing to a fine dispersion of three different precipitates that form on different crystal planes and resist shearing by dislocations: Ω (precipitated on the {111} planes, with stoichiometry unknown but thought to be an orthorhomic form of the θ phase), θ' and S'. Starting from these observations, a family of Al-Li-Cu alloys, known as Weldalite®, has been developed [25]. Weldalite 049® exhibits a potent ageing response to natural and artificial ageing. High strength can be achieved with and without prior cold work [26]. In the Li percentage range of 0% to 2%, maximum strength was reached with 1.3% Li addition [27]. In AA2195, developed from Weldalite® family, T1 phase is reported to be the dominant strengthening precipitate [28].

Gayle et al. [29] evaluated the tensile properties, fracture toughness and microstructure for different alloys in the Al-Cu-Li-Mg-Ag-Zr system. For 0 - 1.4% Li and 0.4% - 1.2% Mg, in all the alloys, coherent platelets of T1 and Ω precipitates (both formed on {111} habit planes) were found; the first is predominant at higher lithium contents, the latter in lithium-free alloys. S' and θ' were also found. Increasing the Mg% caused the S' volume fraction to increase. Huang and Zheng [30] also studied the effect of Li content on AA2195 baseline aluminium alloy. For the peak-aged condition at 180°C and for a nominal lithium composition of 1%, T1 was observed as the main strengthening phase; it precipitates heterogeneously, with high density at subgrains boundaries and more homogeneously distributed in the matrix. In the matrix θ' was also found.

In Table 2.1, the composition of some commercial aluminium-lithium alloys is shown.

Table 2.1 Chemical composition limits of commercial aluminium-lithium alloys [31]

Alloy designation	***Major alloying elements***					
	Li	**Cu**	**Mg**	**Mn**	**Zr**	**Ag**
2090	1.9-2.6	2.4-3.0	0.25	0.05	0.08-0.15	-
2091	1.7-2.3	1.8-2.5	1.1-1.9	0.10	0.04-0.16	-
8090	2.2-2.7	1.0-1.6	0.6-1.3	0.10	0.04-0.16	-
8091	2.4-2.8	1.6-2.2	0.50-1.2	0.10	0.04-0.16	-
2094	0.7-1.4	4.4-5.2	0.25-0.8	0.25	0.04-0.18	0.25-0.6
2095	0.7-1.5	3.9-4.6	0.25-0.8	0.25	0.04-0.18	0.25-0.6
2195	0.8-1.2	3.7-4.3	0.25-0.8	0.25	0.08-0.16	0.25-0.6
2196	1.4-2.1	2.5-3.3	0.25-0.8	0.35	0.04-0.18	0.25-0.6
2197	1.3-1.7	2.5-3.1	0.25	0.10-0.50	0.08-0.15	
2198	0.8-1.1	2.9-3.5	0.25-0.8	0.50	0.04-0.18	0.10-0.50
2050	0.7-1.3	3.2-3.9	0.20-0.6	0.20-0.50	0.06-0.14	0.20-0.7

2.1.6.1. Effect of Zr

Transition elements such Zr (or Mn and Cr) are added to aluminium to form dispersoids that act as recrystallization inhibitors [32]. Zirconium precipitates coherently as β' (Al_3Zr) during homogenisation of the cast billets. In the third generation of aluminium-lithium alloys, the zirconium solute level is typically 0.10-0.20% [31].

Alloys containing zirconium have a finer microstructure and better fatigue properties [33]. When homogenisation treatment leads to a large number of dispersoids, uniformly distributed as small particles, the effect on the recrystallization control is optimised [34].

Dispersoids can also provide a site for the nucleation of δ' particles [35].

2.1.6.2. Effect of Mn

Manganese is an effective strengthener at 0.5 atomic% or less. It tends to produce intermetallic phases that are insoluble at homogenization temperatures, so that only 0.2-0.3% remains in solution. These compounds do not contain lithium and therefore they have no influence on the precipitation sequence. In Al-Li alloys containing manganese, $MnAl_6$ dispersoids can provides sites for the nucleation of δ' particles [15].

2.1.6.3. Effect of Ag and Mg

In the Al-Cu system, minor additions of Ag and Mg promote the precipitation of the Ω phase on {111} habit planes [36]. Addition of these elements (~ 0.4%), in the Al-Li-Cu-Zr system, have been demonstrated to have a strong effect on the precipitation response, improving the tensile properties [25]. In the same system, addition of 1.3% Li with Mg and Ag can double the yield strength compared with an alloy without these elements [27]. In Al-Cu-Li-(Mg)-(Ag)-Zr-Ti alloys, independent Mg addition promotes T1 precipitation and favours GP formation and θ'

precipitation, while independent Ag addition stimulates T1 precipitation and the lengthening of T1 and θ' precipitates. Addition of both elements, improves and accelerates the nucleation of T1 [37].

2.1.6.4. Effect of ageing conditions

T1 precipitates are difficult to nucleate therefore Al-Li-Cu alloys are generally used in T8 temper condition (with prior cold work), since dislocations provide favourable low energy nucleation sites.

Cassada et al. [38] have demonstrated that in Al-2.45%Li-2.45%Cu-0.18Zr, stretching prior to ageing increases the strength of the alloy by up to 20-25%; the peak strength is achieved much more quickly (up to 5 times faster than the un-stretched material). In the stretched materials, the volume fraction of T1 and the number of nucleation sites are greatly increased.

The strengthening response of Al-Cu-Li-Mg-Ag-Zr alloys has been investigated by several authors, with and without stretching prior to ageing [39-44]. These alloys show excellent tensile properties after artificial ageing due to a fine and homogeneous precipitation of T1, θ' and S' phases and some authors [36] also reported the presence of an unidentified precipitate ν. In the overaged condition, θ' and S' are dissolved and T1 is the only strengthening phase present.

For Weldalite 049®, the microstructural evolution and the hardness achieved as a function of ageing (in un-stretched material) is summarised in Fig. 2.4 [39]

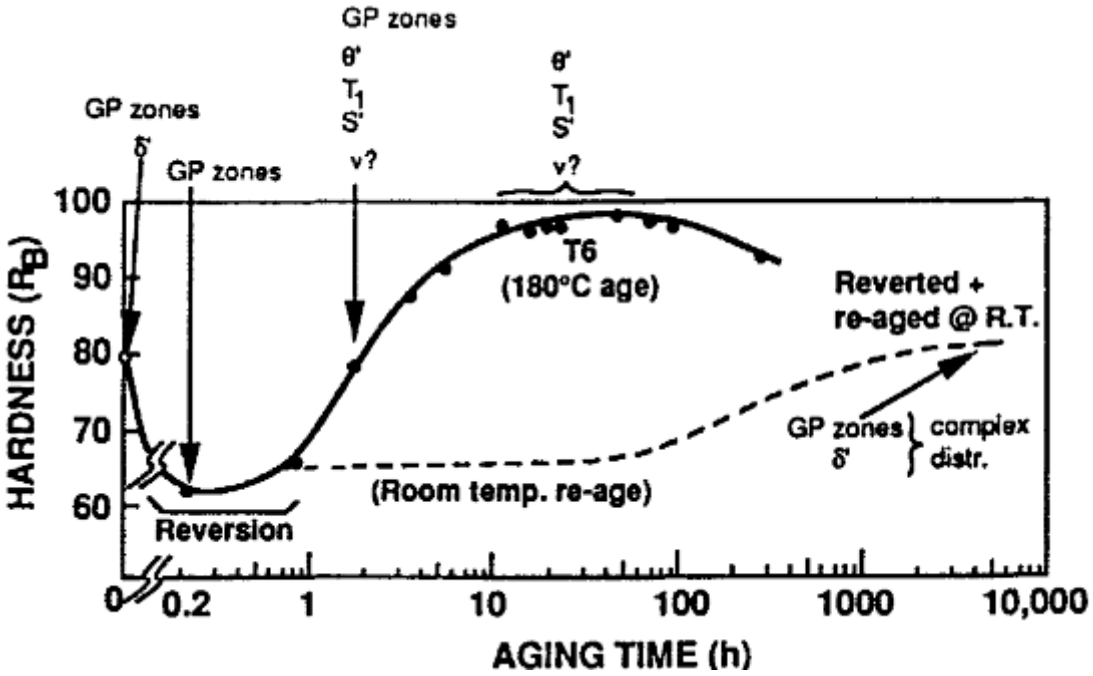

Fig. 2.4 Ageing curves and precipitates in Weldalite 049 alloy in T6 and T4 conditions [39]

The natural ageing resulted in precipitation of GP zones and δ' and in very high hardness. In the early stage of ageing a reversion was observed, due to dissolution of δ' and coarsening of GP zones.

Chen and Bhat [42] investigated the Time-Temperature-Precipitation behaviour in AA2195 (stretched 3%) and found that, in the range of 138 °C – 260 °C, T1 was the predominant precipitate, growing preferentially at subgrain boundaries. In the same range of temperature θ', θ'' forms in the matrix at the expense of GP zones. Ageing at higher temperatures (in the range of 316-371°C) results in the rapid precipitation of θ and θ'. A long treatment (> 10 h) at temperatures above 427°C leads to the formation of equiaxed precipitates of T_B ($Al_{7.5}LiCu_4$). Two TTP (Time Temperature Precipitation) diagrams were proposed for the matrix and grain boundaries (Fig. 2.5).

T1 tends to nucleate at subgrain boundaries, which affects the fracture toughness at cryogenic temperatures. To avoid this, a multi-step ageing treatment has been developed [43, 44]. This ageing treatment, proposed for the AA2195 alloy by Chen and Stanton consist of a permanence of 20 h at 132 °C, followed by 40 h at 138 °C [43].

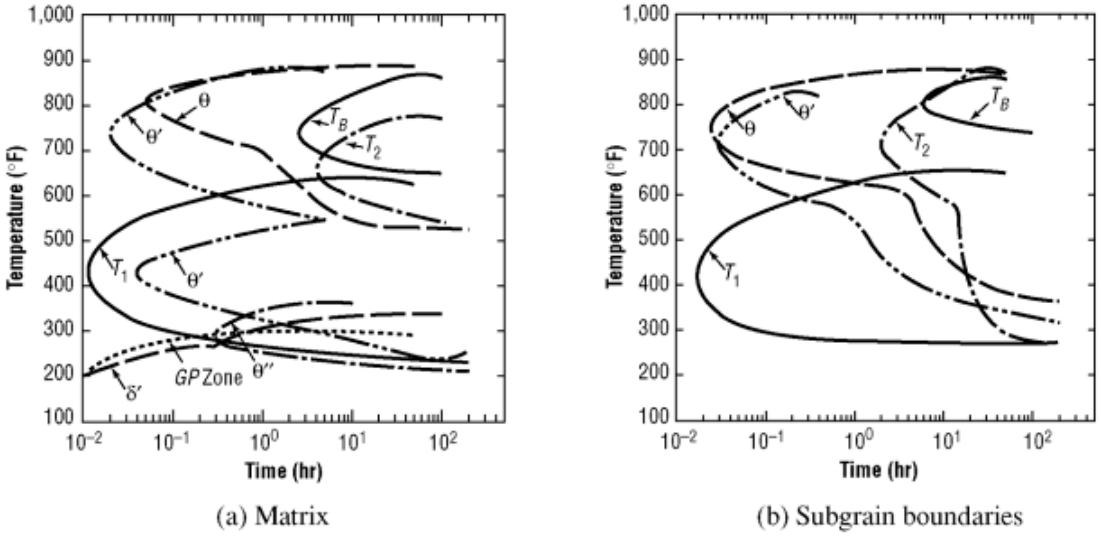

Fig. 2.5 TTP diagrams for AA2195 solution heat treated at 510 °C for 1 h and stretched 3% [42]

The hardness variation as a function of heat treatment temperature and ageing time is shown in Fig. 2.6. Peak ageing condition has been reported in the range of 300-500 ºF (149-260 ºC) due to the precipitation of the main strengthening phase T1.

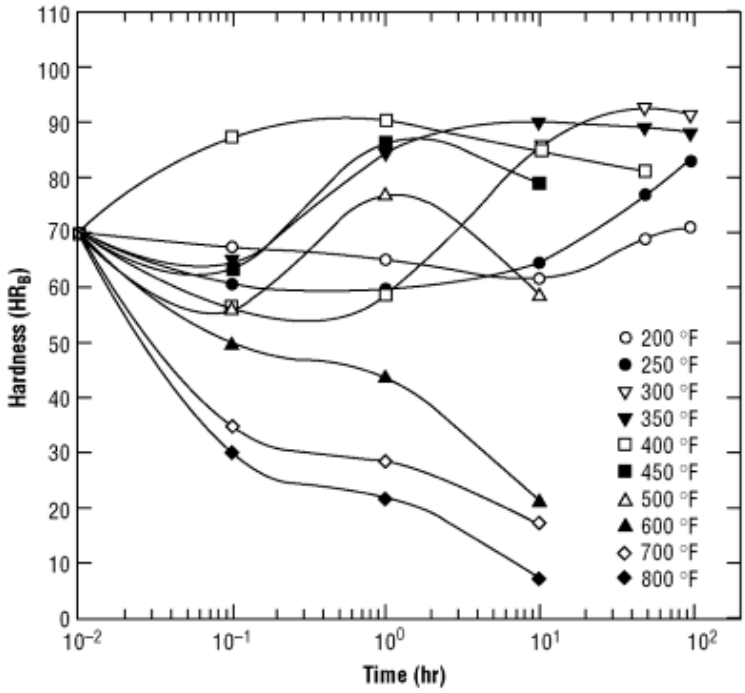

Fig. 2.6 Hardness variations as a function of heat-treatment conditions AA2195 solution heat treated at 510 °C for 1 h and stretched 3% [42]

Shukla and Baeslack found that the main precipitates in AA2195 T8 are T1, θ' and S' [45]. T1 is the predominant strengthening phase, present as plates on {111} planes in the matrix (Fig. 2.7 a) with an average length of about 60 nm; at sub-grains boundaries T1 precipitates with high density and the plates are shorter and thicker (Fig. 2.7 b); θ' is present as plates on {100}with length in the range of 70 to 140 nm (Fig. 2.7 c).

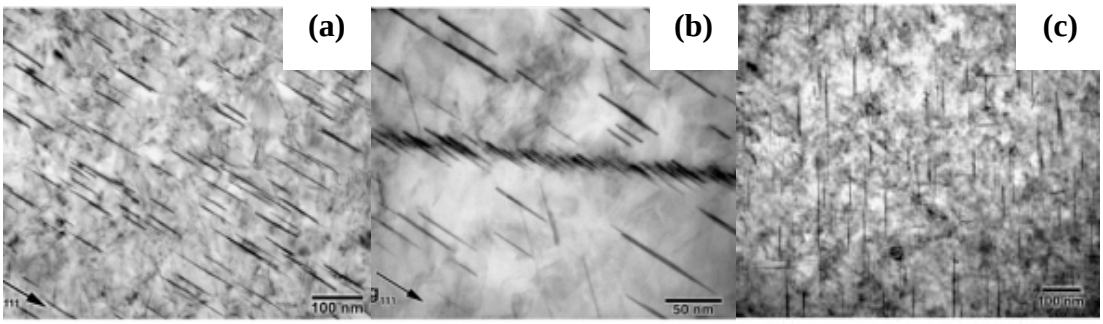

Fig. 2.7 TEM images of the AA2195-T8: (a) fine T1 precipitates; (b) high magnification image showing smaller T1 precipitates at subgrain boundaries; (c) TEM-BF image showing fine θ' precipitates [45]

2.5. Friction stir welding (FSW)

In many applications, Al-Li alloys are joined by Friction Stir Welding (FSW), a solid-state process that operates by generating frictional heat between a rotating tool and the work-piece. Invented at The Welding Institute in 1991, this process has been applied for a number of aluminium alloys, including some highly alloyed grades of the 2XXX and 7XXX series that are difficult to weld with the traditional fusion techniques

2.5.5. FSW processing

During the process of FSW, which is schematically shown in Fig 2.8, a non-consumable rotating tool is plunged into the joint line between two pieces of plate material.

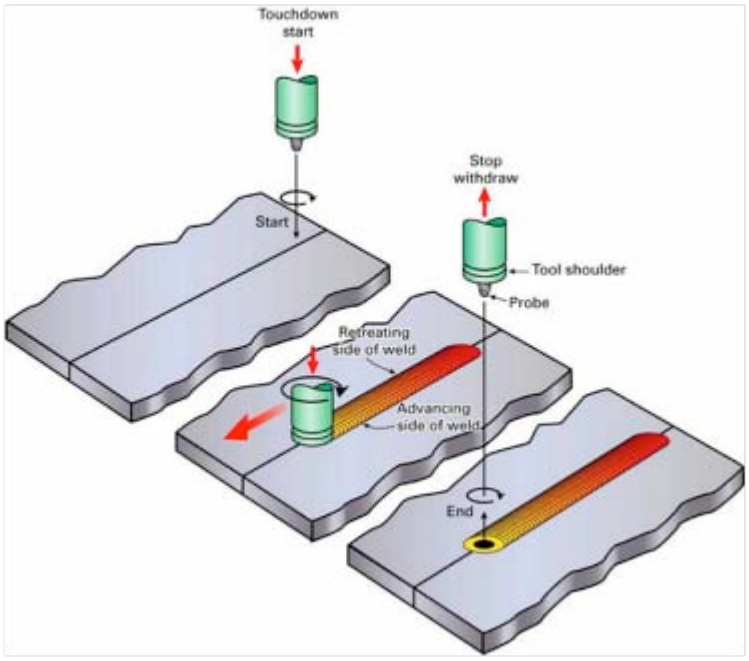

Fig. 2.8 Friction stir welding process [46]

The tool is designed with a profiled pin (probe) that stirs the material into a plastic state and a large concentric shoulder. The frictional heat, needed to plasticize the material, is created by the wear-resistant rotating probe and by the contact

between the shoulder and the material of the work pieces. The shoulder also prevents expulsion of metal from the joint during the welding.

At one side of the weld, the travel direction and the rotation of the tool are in the same direction and the toolpiece encounters fresh metal (Advancing Side) while on the other side they are in opposite directions and the toolpiece enters already processed metal (Retreating Side) Fig. 2.9. The resulting microstructure is different and, therefore, the weld produced is asymmetric.

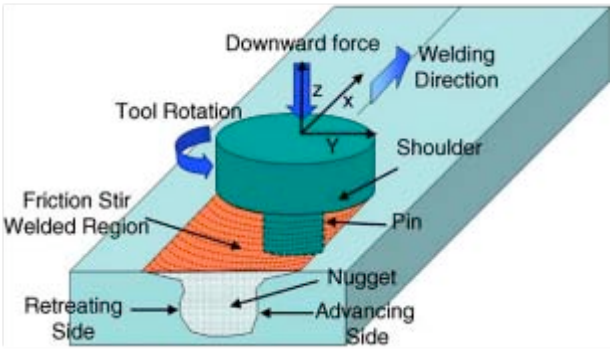

Fig. 2.9 Schematic drawing showing sides of a friction stir weld [47]

The microstructure of the weld, the grain size, the size and the distribution of the precipitates and the resulting mechanical properties are influenced by the temperature distribution. The maximum temperature reached has been estimated from the microstructure observed in the weld [48] or recorded using thermocouples embedded in the region close to the nugget [49-51]. A schematic illustration of FSW zone microstructures, precipitate distributions, and temperature ranges for 7075 is shown in Fig. 2.10.

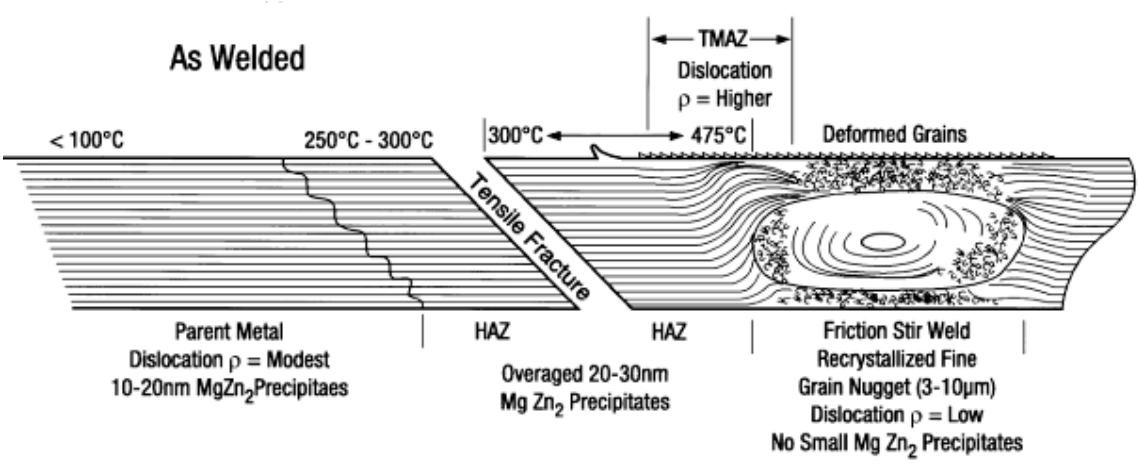

Fig. 2.10 Illustration of FSW in 7075 T651 zone microstructures, precipitate distribution and temperature range [49]

FSW has been successfully adopted in important aerospace applications, for example the Space Shuttle fuel external tank [52] and the Eclipse 500 aircraft [53], and has the potential to be applied in a broad field of applications. Nevertheless the influence of welding parameters and base material properties and conditions on mechanical and corrosion properties of the weld is still far from being completely understood.

2.5.6. Microstructure of FSW aluminium alloys

In the fiction stir weld, no solidification products are present. The nugget is characterized by equiaxed and highly refined grains. Three distinct regions have been identified:

- the recrystallised nugget (stir zone)
- the Thermo-Mechanical Affected Zone (TMAZ), next to the nugget; in this region the grains are highly deformed and heat affected
- the Heat Affected Zone (HAZ): the grain structure undergoes thermal heating but is not mechanically affected

Microstructural differences in these regions are shown in Fig. 2.11.

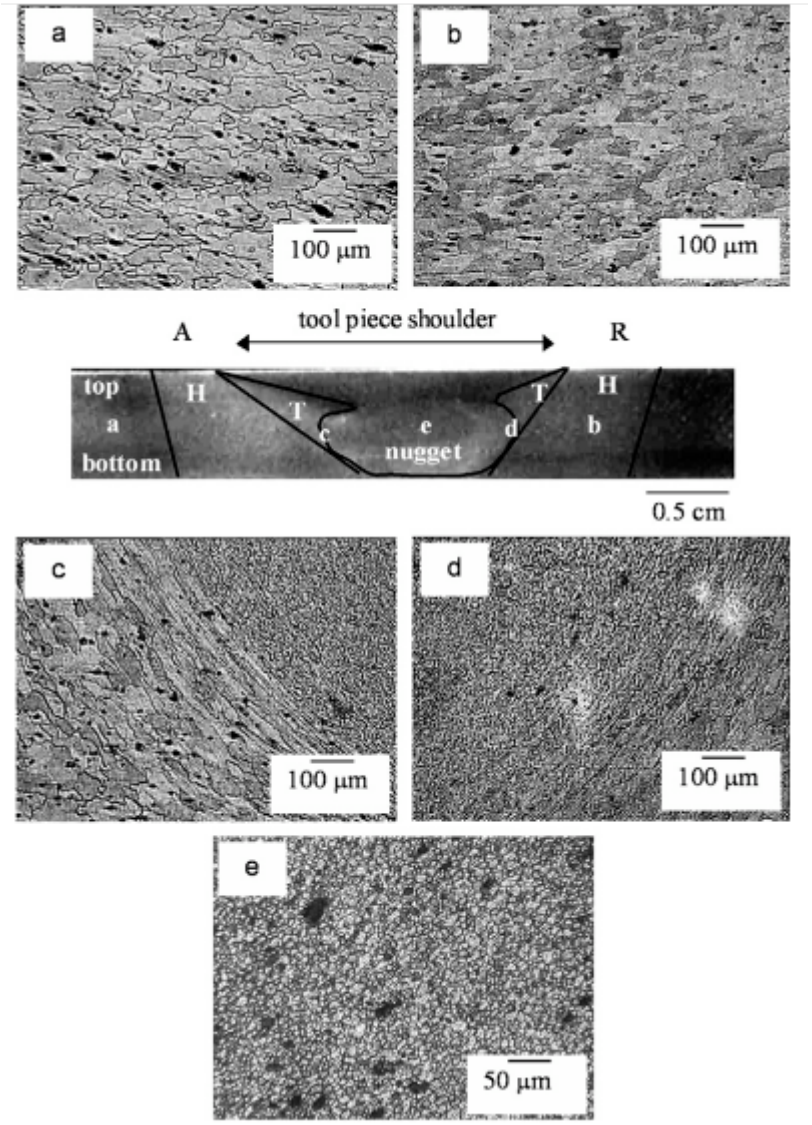

Fig. 2.11 Typical microstructure of the cross section at different regions of FSW AA2024 T351 [51]

2.2.2.1. Nugget

The nugget is the central weld region where the tool-piece pin passes through the material: it is subjected to a high level of plastic deformation and frictional heating. The nugget size is typically slightly greater than the pin diameter. The resulting dynamic recrystallisation process produces fine, equiaxed grains with a size in the range of 1-15 mm [48, 54-57]. The FSW parameters and conditions, the tool geometry, the composition of the material and the temperature of the workpiece, affect the grain size [58, 59]. Mishra and Ma [60] have reported a summary of grain size values for different aluminium alloys and different process conditions.

The peak temperature generated in the nugget region has been reported, from several authors, to be in the range of 450-540°C [56]. Depending on the alloy composition and on the peak temperature reached within the nugget, precipitates can coarsen or dissolve [61, 62]. In some cases, precipitates can go into solution and re-precipitate on dislocations and Al_3Zr dispersoids [57].

In the weld nugget, the large (micron-sized) constituent intermetallic particles are often found to be different in size and distribution compared with those found in the base alloy [57, 63].

The microstructural evolution following FSW of AA2195-T81 has been studied using SEM and TEM [45, 64, 65]. FSW on a AA2195-T81 plate 8.2 mm thick was studied by Schneider et al. [64]. In this study T1 and θ' were identified as the precipitates present in the base material. In the nugget, mixed precipitates of T1, θ' and T_B (Al_7Cu_4Li) or only T_B alone were observed in different locations (Fig.2.12). According to the observations and Time-Temperature-Precipitation diagram proposed by Chen and Bhat [42], the following precipitate sequences were proposed for the nugget:

$T1 + \theta' \rightarrow T1 + \theta' + \theta + T_B$ Fig. 2.12(a)

$T1 + \theta' \rightarrow T_B$ Fig. 2.12(b)

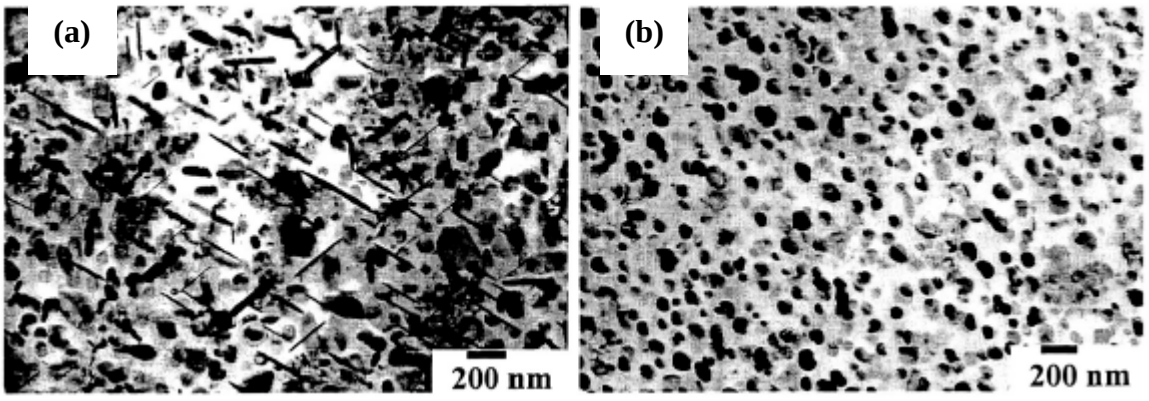

Fig. 2.12 Typical TEM images of microstructure in the nugget AA2195-T81. Mixed T1, θ' and T_B (a) or only T_B (b) [64]

In contrast, the work of Scheneider, Shukla and Baeslack [45] has shown for a FSW on a AA2195-T8 plate 1 mm thick, complete dissolution in the nugget of the

precipitates present in the base material (T1, θ' and S'), while the microstructure of the base material predominantly contained T1 precipitates with an average length of 63 nm in the matrix and, with high density, at subgrain boundaries. Some δ' was found, perhaps due to the natural re-precipitation. Complete dissolution of T1 precipitates in the nugget, has been observed also by Oertelet et al. [65] in the same AA2195-T8 alloy, while large particles reach in Cu and Fe were identified at the grain boundary (Fig. 2.13).

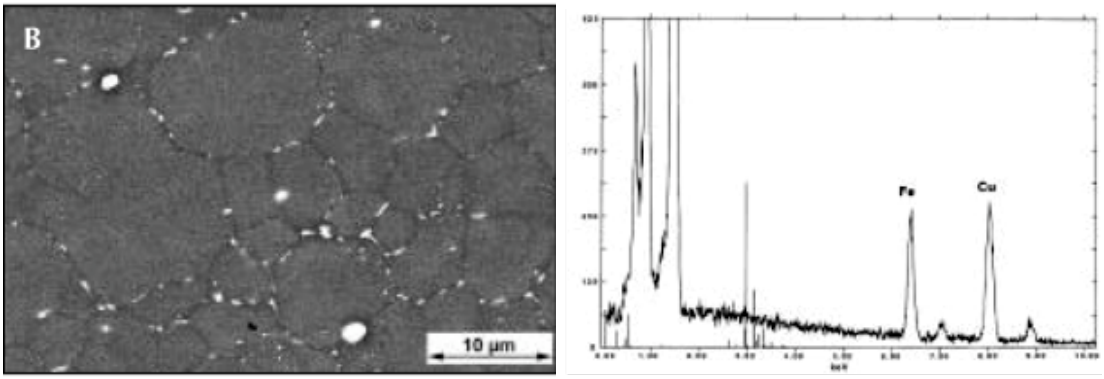

Fig. 2.13 Backscattering image of large grain boundary precipitate in the nugget and EDS spectrum of the GB precipitates (FSW AA2195 T8) [65]

2.2.2.2. TMAZ

The TMAZ is the region, adjacent to the nugget, in which the grains are highly deformed but, due to the lower temperature and the lesser degree of deformation, recrystallization has not taken place [66].

The peak temperature has been reported in the range of 350-450°C [49, 56]. These temperatures are sufficiently high to dissolve some precipitates [67].

In some case, large precipitate present in the parent material may be unaffected, while small precipitate can coarsen and Precipitate Free Zone (PFZ) may also be present [48].

2.2.2.3. HAZ

The Heat Affected Zone is the region, adjacent to the TMAZ, that has been subjected to thermal heating but not plastic deformation. There is no sharp transition from TMAZ to HAZ and from HAZ to the base material because the change in microstructure is gradual [62].

The peak temperature has been reported in the range of 250-350°C [49, 56]. At these temperatures the coarsening of precipitates at the grain boundary and PFZ has been observed (Fig. 2.14) [57, 62].

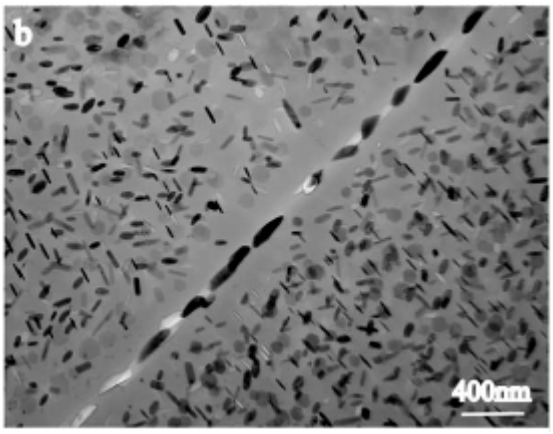

Fig. 2.14 TEM image of precipitates in the HAZ (FSW AA7050 T651) [57]

In the work of Shukla and Baeslack [45], 2 different positions in the HAZ were studied:

- Next to the TMAZ, T1 precipitates were found partially dissolved in the matrix and coarsened at the subgrain boundary, where PFZs were also observed. In the same region, dissolution of θ’ and S’ and re-precipitation of some δ' have been observed.
- Next to the base material the precipitate microstructure consisted essentially of T1. A decrease in the length and density of T1 precipitates, and dissolution of θ’ and S’ has been observed, compared with the base material.

In the 3 heat-affected regions of the weld, the temperature at which precipitates can dissolves, strongly depends from the precipitates size in the base material [68].

2.2.3. Mechanical properties of FSW

The alteration in the microstructure, due to the FSW process, creates a hardness drop across aluminium alloy FSWs [45, 54, 55, 58, 62, 63, 65, 69, 70]. The drop in hardness has been reported to be associated with the coarsening and the dissolution of the strengthening precipitates [45, 64]. For the AA6063 T5 FSW, Sato et al. reported that, rather than the grain size the precipitate distribution plays the main role in the hardness profile [69].

For a FSW in AA2195-T8, a typical hardness profile is shown in Fig. 2.15 [69].

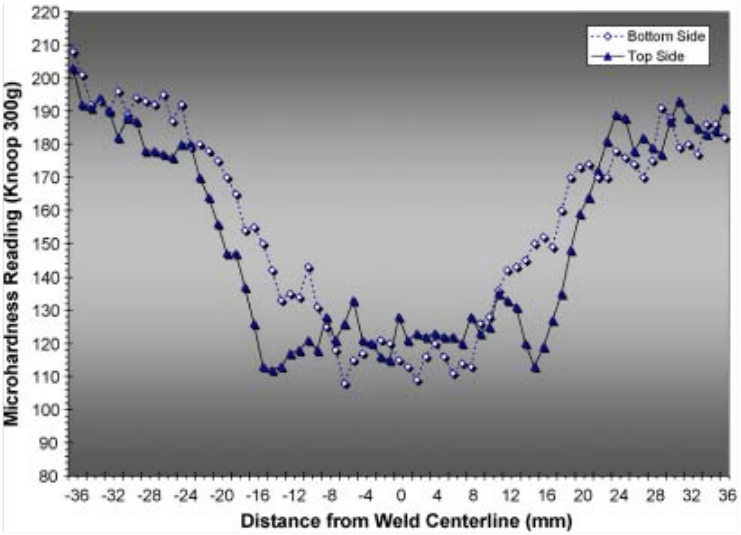

Fig. 2.15 Microhardness profile across the weld AA2195 T8 FSW [69]

Schneider et al. [64] has observed a high degree of scatter in the hardness values in the nugget; the lower values have been attributed to a T_B precipitate microstructure and the higher to the mixed microstructure of T1, θ' and T_B.

A study conducted by Pouget and Reynold [70] on residual stress and microstructure effects on fatigue crack growth in AA2050 T81 FSW reported that

post weld heat treatment (15 h @ 160°C) can give an increase in the hardness values in the weld. The hardness profiles are shown in Fig. 2.16.

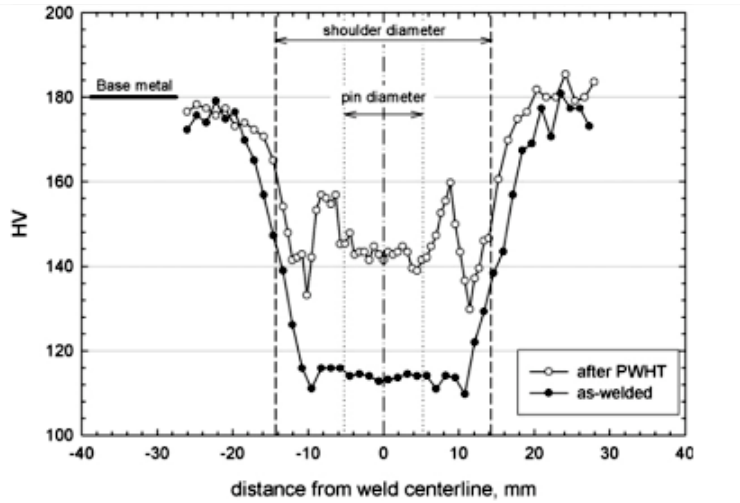

Fig. 2.16 Microhardness profile across the weld AA2050 T8 FSW, with and without post weld heat treatment (15 h @ 160°C) [70].

After post weld heat treatment, a "W" shape can be observed in the hardness profile, with maxima at either edge of the nugget, in the TMAZ region. It was suggest that the high deformation during the welding process increases the amount of precipitation during the post-weld ageing treatment. However studies on the effect of FSW on microstructure of 7075 [47-49], have reported a reduction in dislocation density in the TMAZ. Similar hardness profiles along the weld (in the as-welded condition) have been reported for AA2195 [45] and the reduction in hardness in the weld region was related with the dissolution of the main strengthening precipitates present in the base material.

Welding parameters (tool rotation speed and tool-piece travel speed) have been shown to have a strong influence on the hardness values in the weld region [51].

2.3. Corrosion of Al and Al-Li alloys

2.3.1. Corrosion of aluminium in aqueous environments

The oxidation reactions of metals can be classified according to their respective electrochemical potentials. The more electronegative is the potential the higher is the tendency to oxidise and, in particular condition, to corrode in aqueous media. Thermodynamically, aluminium is a very reactive metal; aluminium has a highly negative standard electrode potential of 1660 mV [71]. Therefore, aluminium is expected to be very unstable in the presence of moisture. However, because the formation of a natural, adherent, self-healing oxide film that is stable in the pH range of approximately 4 to 9, aluminium shows a high resistance to corrosion.

The natural oxide film is formed according to the reaction:

Eq. 2.1 $2Al_{(s)} + 3H_2O_{(l)} \rightarrow Al_2O_{3(s)} + 6H^+_{(aq)} + 6e^-$

Temperature and oxygen pressure influence the growth of this oxide layer.

The thickness of this protective surface layer is about 5-10 nm [1, 71]. In wet environments the anodic dissolution of aluminium take place according to the following reaction:

Eq. 2.2 Anodic dissolution: $Al \rightarrow Al^{3+} + 3e^-$

The electrons produced by this anodic reaction (described by the Equation 2.2) must be consumed by one of these two cathodic reactions:

Eq. 2.3 Cathodic oxygen reduction: $\mathbf{O_{2(g)} + 2H_2O_{(l)} + 4e^- \rightarrow 4OH^-_{(aq)}}$

Eq. 2.4 Cathodic water reduction: $\mathbf{2H_2O_{(l)} + 2e^- \rightarrow 2OH^-_{(aq)} + H_{2(g)}}$

The oxide passive film is resistant to dissolution in neutral pH and is a good insulator. For these reasons, the electrons produced by the anodic reaction cannot reach the oxide/solution interface, where the cathodic reactions take place.

The stability of the oxide film is expressed by the potential vs. pH diagram as shown in Fig. 2.17.

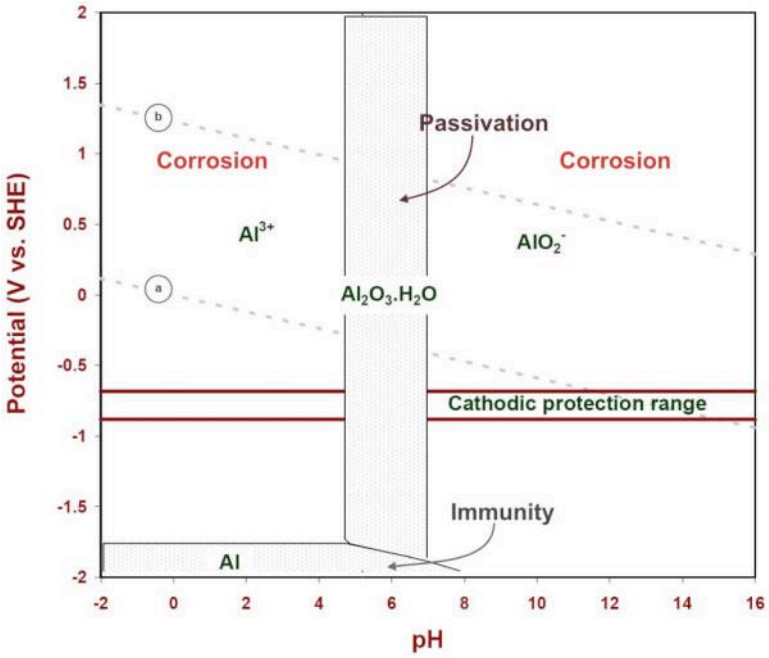

Fig. 2.17 Theoretical regions of corrosion, immunity and passivation for aluminium at 25ºC in the presence of water [72]

Aluminium's protective film is stable in the pH range of 4 - 8.5 but this range can be altered by the presence of substances that can react with the metal. The oxide film is soluble in acid and alkaline environments, according to the following reactions:

Eq. 2.5 $Al_2O_{3(s)} + 6H^+_{(aq)} \rightarrow 2Al^{3+}_{(aq)} + 3H_2O_{(l)}$ in acid conditions

Eq. 2.6 $Al_2O_{3(s)} + 3H_2O_{(l)} + 2OH^-_{(aq)} \rightarrow 2Al(OH)_4^-{}_{(aq)}$ in alkaline conditions

In such environments the integrity of the protective oxide layer is compromised and localized corrosion, like pitting, can take place through the following reaction:

Eq 2.2 Dissolution: $Al_{(s)} \rightarrow Al^{3+}_{(aq)} + 3e^-$

Eq 2.7 Hydrolysis: $Al^{3+}_{(aq)} + H_2O_{(l)} \rightarrow AlOH^{2+}_{(aq)} + H^+_{(aq)}$

Eq 2.8 Alkaline dissolution: $Al_{(s)} + 4OH^-_{(aq)} \rightarrow Al(OH)_4^-{}_{(aq)} + 3e^-$

The last reaction happens only in extremely alkaline conditions since usually the film will dissolve at the film/solution interface and grow at the metal/film interface.

2.3.2. Influence of alloying elements

High-purity aluminium (99.999%) is highly corrosion resistant but it possesses a very low yield strength in the annealed condition (7-11 MPa) [1], therefore it is generally alloyed with elements such Cu, Mg, Zn, Li, Mn, Si.

The effects of principal alloying elements on the electrolytic-solution potential of aluminium is shown in Fig. 2.18 [73]. Homogeneous additions of Mn, Cu and Si result in an increase in solution potential, while additions of Mg and Zn reduce aluminium's corrosion potential.

Aluminium alloys are generally more corrosion resistant when the alloying elements are in solid solution, but because the equilibrium solubility of most of metals in aluminium is low, alloying additions result in the formation of second phase particles. These particles also commonly contain impurities such iron. Elements like Fe, Mn, Cu, Si, form particles that have thinner, and more conductive passive films than that on pure aluminium, and allow cathodic reaction to take place and dissolution of aluminium to proceed. Moreover these particles can acts as pit initiation sites [74]. For these reasons, aluminium alloys are less corrosion resistant than high-purity aluminium. Series 1xxx (Al $\geq$ 99.0%) possess the highest corrosion resistance, followed by the non-heat treatable alloys (series 3xxxx, 4xxx and 5xxx). Heat

treatable alloys exhibit the lower corrosion resistance, in this order: series 6xxx, series 7xxx and series 2xxx [71].

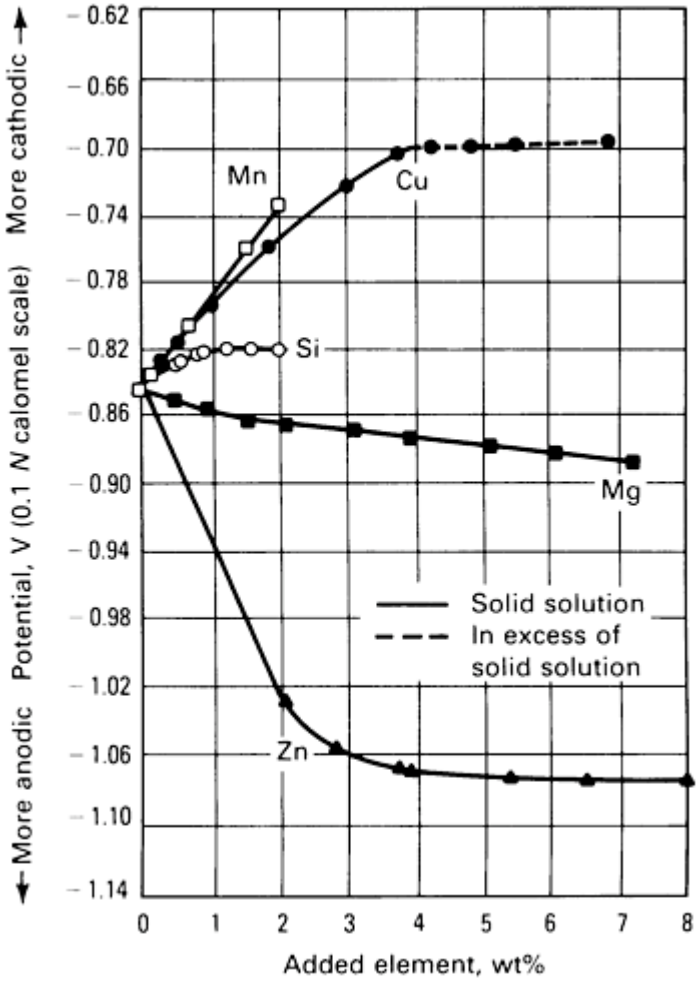

Fig. 2.18 Effects of principal alloying elements on the electrolytic-solution potential of aluminium. Potentials are for solution-treated and quenched high-purity binary alloys in a solution of 53 g/L NaCl plus 3 g/L H_2O_2 at 25 °C (75 °F) [73].

The corrosion behaviour of wrought aluminium alloys depends strongly on the nature and distribution of these second-phase particles. These particles can be grouped as:

- Particles formed by reaction between aluminium and alloying elements or between alloying elements in order to improve specific properties (strengthening particles or dispersoids)
- "Constituent" particles, often containing impurities, that precipitate during solidification

Intermetallic particles can act as preferential initiation sites for localised corrosion [75]. Intermetallic particles that are more electrochemically active than the matrix act as anodes and undergo dissolution, while particles that are nobler than the aluminium matrix act as cathodes. Corrosion potentials for intermetallic particles commonly found in aluminium alloys are shown in Table 2.2.

Table 2.2 Corrosion potentials (average values) for intermetallic particles commonly found in aluminium alloys, also including pure metals [76].

Stoichiometry	**Corrosion potential (mV, SCE) in NaCl solutions**		
	0.01M	**0.1M**	**0.6M**
Al_3Fe	-493	-539	-566
Al_2Cu	-592	-665	-695
Al_3Zr	-752	-776	-801
Al_6Mn	-839	-779	-913
Mg_2Al_3	-1124	-1013	-1162
$MgZn_2$	-1001	-1029	-1095
Mg_2Si	-1355	-1538	-1536
Al_2CuMg	-956	-883	-1061
Al	-679	-823	-849
Mg	-1601	-1586	-1688
Mn	-1315	-1323	-1318
Si	-450	-441	-452
Cu	-117	-232	-220

Different types of corrosion can occur on aluminium and aluminium alloys. The predominant type of corrosion depends on several factors, related to the metal and its properties and conditions, to the medium and to the conditions of use.

2.3.3. Pitting corrosion

Pitting corrosion is a localised form of attack resulting in the formation of cavities in the surface of the metal. The process can be divided into two steps: initiation and propagation.

In aluminium alloys, the initiation of localized pitting corrosion is possible in presence of a local breakdown of the passive film. Film breakdown occurs when the oxide layer is not completely uniform and in presence of aggressive species as chloride ions. The presence of second phases and intermetallic particles lead to a heterogeneous passive film.

Pit propagation in aluminium is schematically illustrated in Fig. 2.19.

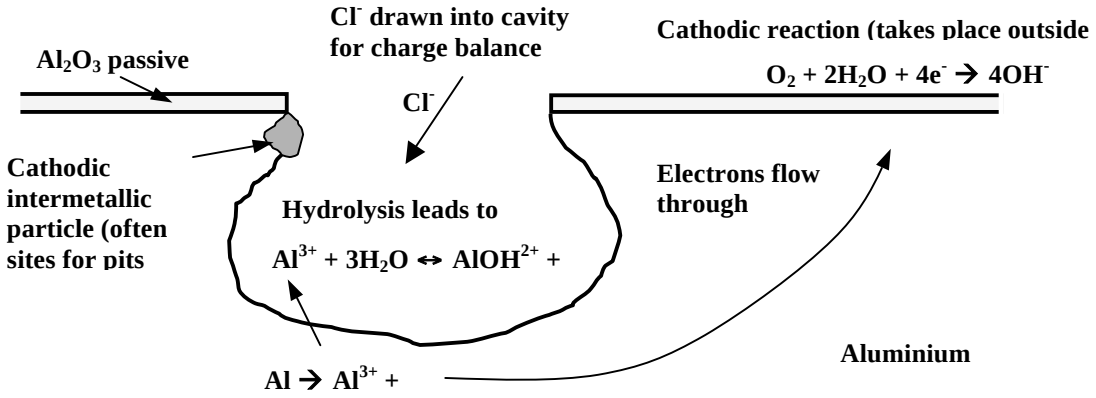

Fig. 2.19 Diagram illustrating the mechanism of pitting corrosion in aluminium

The presence of chloride ions promotes the dissolution of aluminium according to the Equation 2.2. The hydrolysis of aluminium chlorides (Eq. 2.7) will lead to an acidification of the pit at the bottom and to a further increase in dissolution (pit growth) of the metal and prevent repassivation. The dissolution of aluminium by formation of Al^{3+} ions at the bottom of the pit creates an electrical field that attracts Cl^- ions towards the pit bottom. Al^{3+} ions being concentrated at the bottom of the pit,

they diffuse towards the metal surface, where the cathodic reaction leads to alkalisation, and will precipitate as $Al(OH)_3$.

Pitting is associated with a 'breakdown potential', a potential at which a rapid increase in current occurs and stable pit growth. It is measured using potentiodynamic sweeps in which the potential applied to a sample is steadily increased until stable pitting takes place.

2.3.4. Intergranular corrosion

Intergranular corrosion (IGC) is a form of selective attack that takes place preferentially at grain boundaries. IGC penetrates faster than pitting corrosion but, because the limited oxygen available in the narrow corrosion path, reaches a self-limiting depth and, at this stage, it starts to spread laterally.

The propagation of IGC starts at pits and it is caused by a difference in chemical composition between the matrix (the bulk of the grains) and the grain boundaries. This gradient of composition lead to a difference in the electrochemical potential that is the driving force for the process. The potential of the matrix, as seen in Fig. 2.18, depends on the concentration of the alloying elements and differs from the potential of the intermetallic compounds (Table 2.2).

IGC can occur in two ways:

- Precipitation of an anodically-active phase (more electronegative than the matrix).

This is the case for β (Mg_2Al_3) phase for the 5xxx series alloys, or η ($MgZn_2$) phase for the copper-free 7xxx series, that precipitate at grain boundaries after prolonged heating. These reactive phases at the grain boundaries, in presence of a corrosive medium, undergo to anodic dissolution and can generate IGC.

- Precipitation of noble phase (less electronegative than the matrix).

This is the case for 2xxx series, and copper-bearing 7xxx series: the precipitation of copper-rich particles such as θ (Al_2Cu) at the grain boundaries leads

to the formation of a narrow band nearby that is depleted in copper and susceptible to anodic dissolution. IGC is essentially a galvanic corrosion process that takes place between the copper-depleted zone (anode) and the copper-rich phase Al_2Cu and it is driven by the difference in electrochemical potential of these two phases (Fig. 2.20). In aged Al-4%Cu, IGC has been demonstrated being a consequence of the pitting corrosion of a copper-depleted zone along the grain boundaries [78].

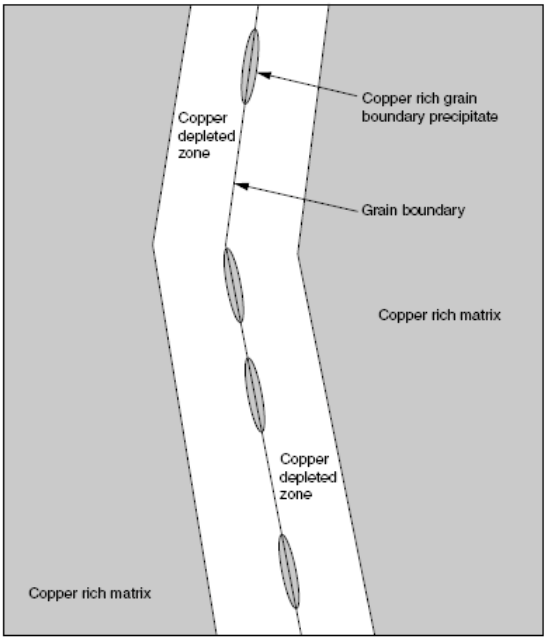

Fig. 2.20 Grain boundary region in a 2xxx alloy [77]

2.3.5. Exfoliation corrosion

Exfoliation corrosion is a type of selective corrosion that propagates along a large number of planes running parallel to the direction of rolling or extrusion [79]. This kind of corrosion is generally developed from intergranular attack [80]. The entrapped and voluminous corrosion products formed along the paths of attack produce an internal stress that splits off the overlying layers of metal, hence the name "exfoliation". Exfoliation occurs predominantly in products that have markedly directional structures in which highly elongated grains form platelets that are thin relative to their length and width [73].

In Al-Li alloys, exfoliation lowers strength, fatigue proprieties and service life. In a study of Li et al. [81], the extent of exfoliation corrosion has been evaluated for Al-2.8%Cu-1.5%Li-0.3%Mg-0.3%Zn-0.3%Mn-0.15%Zr using Electrochemical Impedance Spectroscopy in EXCO solution (4.0 M NaCl + 0.5 M KNO_3 + 0.1 M HNO_3). The alloy was found susceptible to this kind of attack and the susceptibility increased with ageing time (Fig. 2.21).

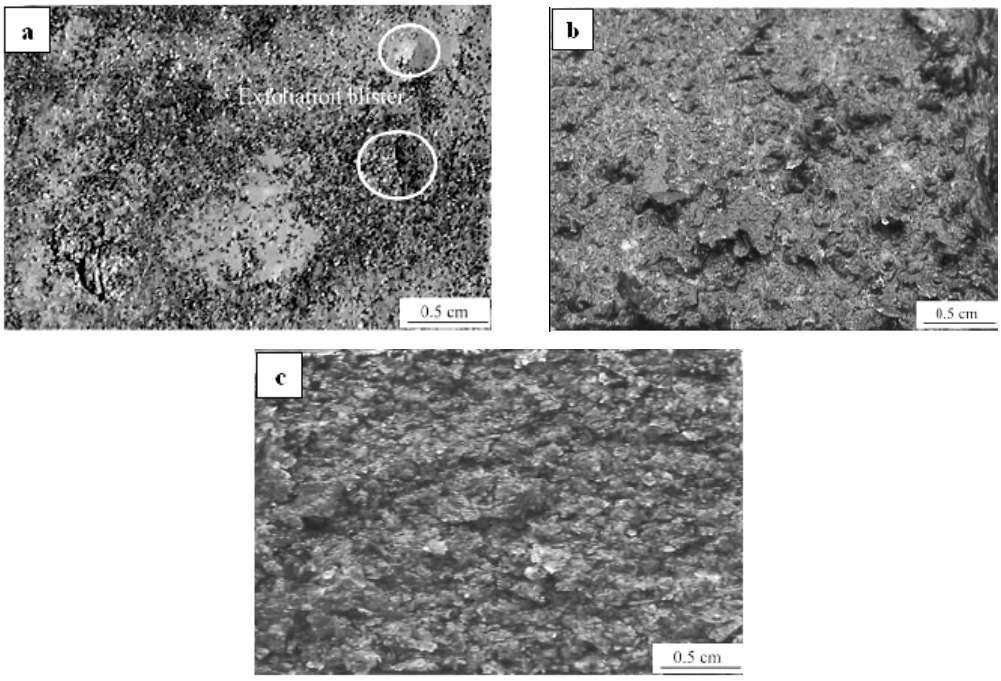

Fig. 2.21 Corrosion morphologies of (a) under-aged, (b) peak-aged and (c) over-aged Al-Li alloys immersed in EXCO solution for 96 h [81]

2.3.6. Corrosion of Al-Cu-Li alloys

AA2050 contains copper as major alloying element. As discussed in the previous section, copper has a strong effect upon the tendency of aluminium alloys to corrode. The presence of second phases rich in copper or heterogeneity in the copper solid solution distribution, produces microscopic galvanic potential differences that make these heat-treatable alloys less resistant to corrosion than alloys of other series. Furthermore, the rate of quenching and the temperature and time of artificial ageing can both affect the corrosion resistance [73, 82].

Lithium, unlike copper, is more active than aluminium and lithium-containing particles tend to be predominantly anodically active (particularly precipitates with a high Li content). The rate of dissolution of aluminium is only slightly increased by lithium in solid solution, while the rates of repassivation doesn't change significantly [83]. The repassivation behaviour is altered by precipitation of lithium rich phases; the nature of these alterations depended on the type of precipitate. For instance overageing Al-Li alloys resulted in the precipitation of δ (AlLi) at the grain boundaries and increasing lithium dissolution [83].

An extensive corrosion investigation of a number of binary and ternary aluminium-lithium alloys as been carried out by Niskanen et al. [84]. The formation of the δ (AlLi) anodic phase was found to have deleterious effect on the corrosion resistance in 3.5% NaCl solution. Increasing ageing time and sites for heterogeneous nucleation of this phase increase the presence of this phase and the corrosion susceptibility. In overageing conditions and at high Mg contents (> 3.5 wt%) the presence of the AI_2MgLi as dominant phase tying up lithium in the δ (AlLi) and reduce the pitting tendency.

In the study of localized corrosion of AlCuLi alloys two main mechanism are considered:

- Preferential anodic attack on very narrow, anodic copper-depleted regions along the grain boundaries [85, 86]. Kumai et al. [85] suggest that intergranular corrosion is caused by the anodic dissolution of PFZ.
- Anodic dissolution of active T1, when the ageing condition leads to the precipitation of these phases at the grain boundary [87].

Since the main precipitate in Al-Cu-Li, including T1, contain both Cu and Li, the two mechanisms are possible.

2.3.6.1. Role of copper depleted zone

Kumai et al. [85] have studied the pitting corrosion as a function of ageing at 200 ºC of an Al-Li alloy (Alloy A) and an Al-Cu-Li alloy (Alloy B - AA2090) in solutions with and without chloride ions. In **Alloy A** δ' phase precipitates throughout the microstructure, leading a PFZ adjacent to high-angle grain boundaries, but not at the sub-grain boundaries (Fig. 2.232 – Alloy A). For this alloy corrosion at grain or subgrain boundary was not observed and ageing alloy did not have significant effect on its pitting potential, in agreement with an earlier study [84]. In **Alloy B**, the ageing treatment resulted in the formation of a copper-depleted zone and a PFZ along the high-angle grain boundaries. In the same alloy precipitation of phases rich in copper (T1 and θ), preferentially at subgrain boundaries, took place leading to the formation of zones that are free of these precipitate and depleted in copper (Fig. 2.22 – Alloy B). In this case, corrosion attack was found both at grain and subgrain boundaries. In the same alloy, stretched before ageing, copper depleted region was not found and attack at boundaries was not observed. From these observation it was suggested that the corrosion attack was the result of attack of the copper depleted region along grain and subgrain boundaries.

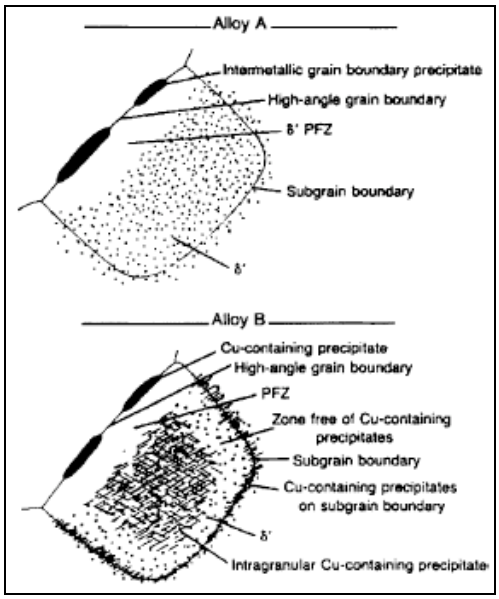

Fig. 2.22 Schematic illustration of phase changes and PFZs formation in aged Al-Li alloy (alloy A) and AA2090 (alloy B) [85]

Selective dissolution of a Cu-depleted zone has also been proposed to explain SCC susceptibility of Al-Cu-Li alloys [86].

3.3.6.2. Role of active precipitates

Selective dissolution of T1 was first proposed by Rinker et al. [88] as mechanism for intergranular attack in AA2020. Buchheit et al. [87] have investigated the role of T1 precipitates in localized corrosion of AA2090 in aerated and deaerated NaCl solutions. T1 phase was found concentrated in subgrain boundaries of artificially aged AA2090. Based on polarization measurements this strengthening precipitate was found to be an active phase and, despite the high Cu content, the corrosion potential was lower than the one measured for the matrix and the copper depleted zone. In order of decreasing nobility the following galvanic series was found: Solution Heat Treated 2090→ Cu depleted zone → T1. In aerated Cl^- containing solutions, the attack was found at subgrain boundaries because the reactivity of T1, concentrated there and the resulting acid environment at the subgrain boundaries fissures determined the dissolution of the 2090 matrix and lead to a continuous attack. Also in the large pits around Fe and Cu-rich impurity particles, a strong role of T1 was suggested.

The role of the strengthening phases present in the Al-Cu-Li-X system on the corrosion behaviour has been studied by Kertz et al. [82]. In this study the effect of slow or interrupted quenching on localized corrosion susceptibility of an Al-1.8Li-2.70Cu-0.6Mg-0.3Zn alloy (AF/C458) has been evaluated. The major precipitate phases of this alloy were identified as: δ' (Al_3Li), T1 (Al_2CuLi), θ' (Al_2Cu), T_B (Al_7Cu_4Li), T2 (Al_6CuLi_3) (Al_5CuLi_3 according to Chen and Bhat [42]). After immersion in 57 g/l NaCl plus 10 ml/l H_2O_2, it was found that intergranular (IGA) and inter-subgranular (ISGA) attack occurred when T1 precipitate was found at boundaries. No evidence of Cu depleted zone was found. Furthermore, the alloy was observed to be resistant to IGA and ISGA when only θ' and T_B were found at boundaries. The selective dissolution of the T1 active phase was therefore proposed as driving force for boundary attack and a “critical density” of this precipitate was also suggested as necessary condition to generate corrosion.

A change in the electrochemical behaviour, from anodic to cathodic, of T1 precipitates, due to the dealloying of lithium from this phase, has been observed and it was suggested that localized corrosion was a consequence of an alternating

dissolution of this active phase and the base alloy at its adjacent periphery [89-92]. Simulated bulk of T1 and T2 (fabricated through melting and casting) and simulated Al alloy containing these particles were prepared and the electrochemical behaviour in 3.5% NaCl solution was investigated [89, 92]. The potential of T1 and T2 precipitates was found to be negative with respect to that of α(Al) (Fig. 2.23).

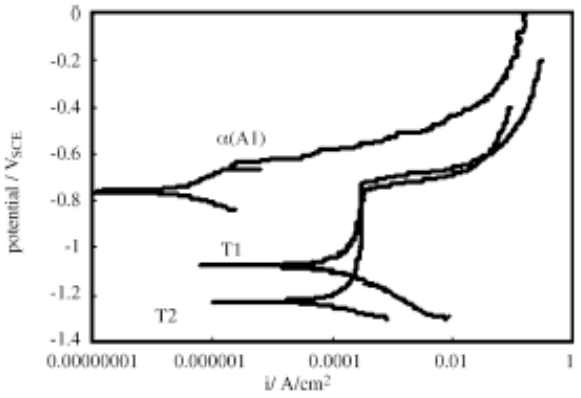

Fig. 2.23 Potentiodynamic scanning curves of α(Al), T1 and T2 in 3.5% NaCl solution [89].

The coupling behaviour of T1 and T2 with α(Al), was also investigated, measuring the coupling current in 3.5% NaCl. The OCP of the individual phases was also measured at regular intervals. During coupling in 3.5% NaCl solution, a change in the OCP of T1 (Fig. 2.24a) and, consequently, in the coupling current of this precipitate in the T1- α(Al) system was observed (Fig. 2.24b). The OCP of T1 become less negative than α(Al) and the coupling current change from anodic to cathodic. It was suggested that at the beginning of the corrosion process T1 was attacked, while Li was preferentially dissolved this phase become rich in Cu and nobler than the matrix, leading to the dissolution of the surrounding base alloy. After 12 h of immersion in 3.5% NaCl solution, corrosion is observed in the simulated T1 particles and at the boundary with α(Al) (Fig 2.25).

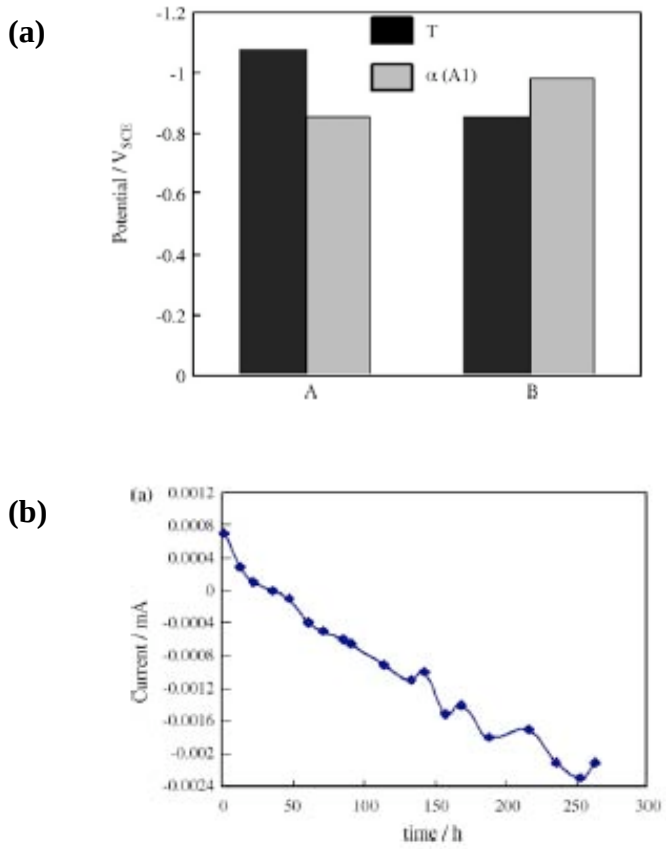

Fig. 2.24 (a) Open circuit potential variation of T1 and α(A1) in 3.5% NaCl solution (**A** At beginning of the test, **B** after coupling for 10 days)
(**b)** Coupling current of T1 in the T1- α(Al) system [89].

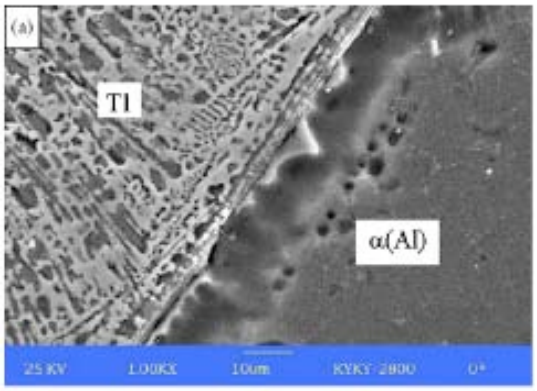

Fig. 2.25 Corrosion morphology of simulated Al-Cu-Li alloy containing T1 particles, immersed in 3.5% NaCl for 12h [89].

More complex coupling behaviour was observed for T2. This phase contains more Cu and less Li than T1. T2 is acts as anodic phase at the beginning of the test, then becomes cathodic and finally again anodic. The OCP variation and coupling current

are shown in Fig 2.26 while the corrosion morphology after 12 h immersion in 3.5% NaCl solution is shown in Fig. 2.27.

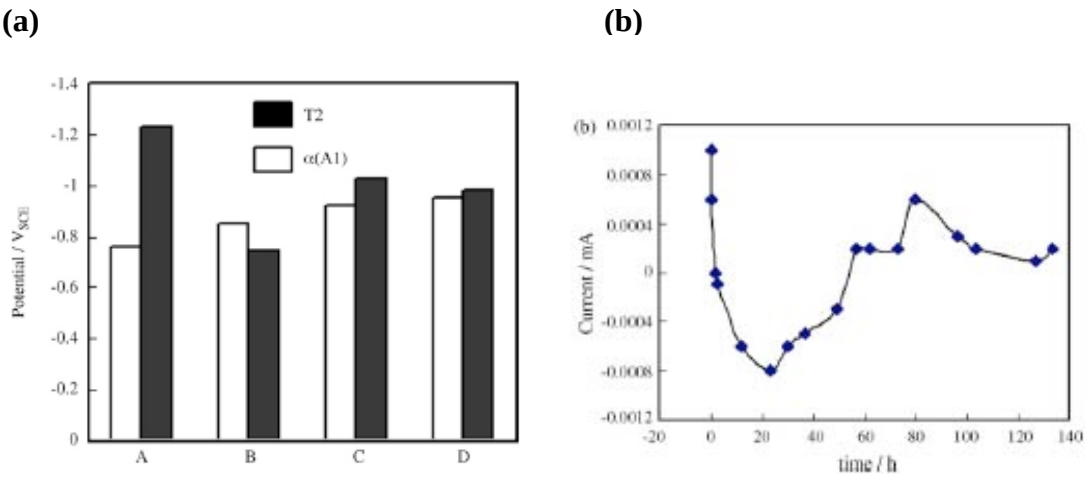

Fig. 2.26 (a) Open circuit potential variation of T2 and α(A1)
(A At beginning of the test, B after coupling for 12.2 h, C after 80.3 h, D after 133 h)
(**b)** Coupling current of T2 in the T2- α(Al) system [89].

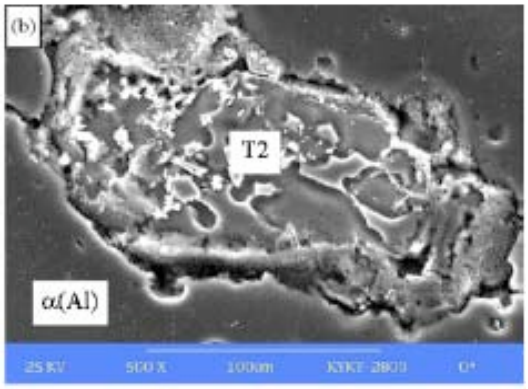

Fig. 2.27 Corrosion morphology of simulated Al-Cu-Li alloy containing T2 particles, immersed in 3.5% NaCl for 12h [89].

In the same studies TEM samples were made from an AA2195 over-aged at 300 °C for 24 h. T1 was observed within the grains and T2 at grain boundaries. After immersion of the TEM sample, for 1 h in 3.5% NaCl, a change in colour of the precipitates (from dark to white was related to preferential attack of these phases (Fig. 2.28).

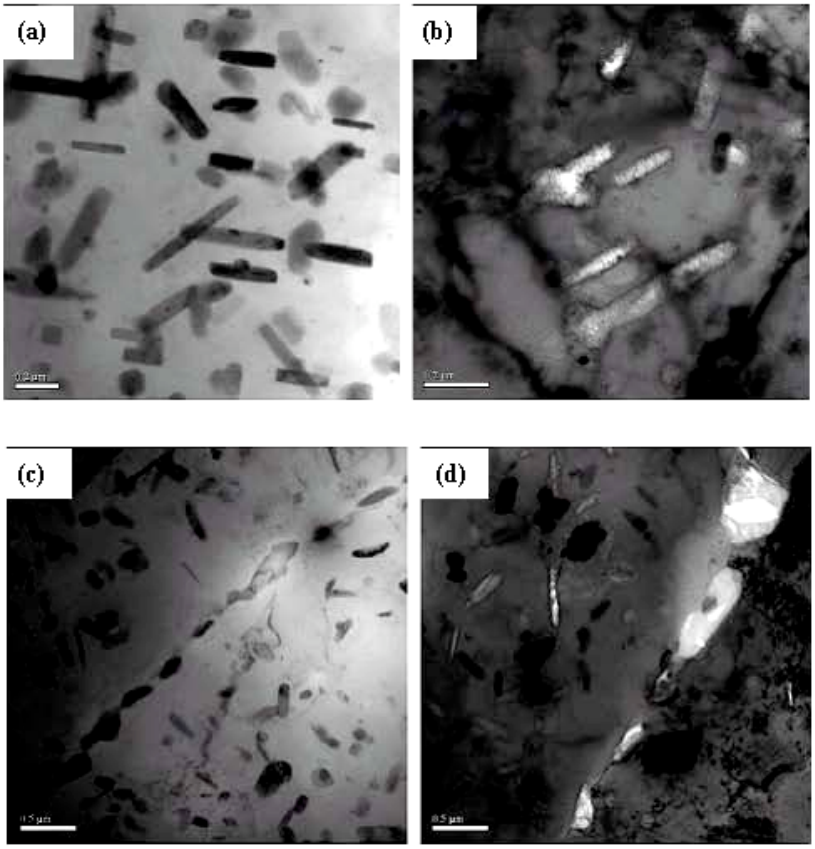

Fig. 2.28 Bright field TEM image of 2195 A1-Li alloy aged at 300°C for 24h. T1 precipitates inside the grain before (a) and after (b) immersion in 3.5% NaCl solution for 1h. T2 precipitates at grain boundaries before (c) and after (d) 1h immersion in 3.5% NaCl solution.

A summary of corrosion potential of T1, T2, θ' precipitates and simulated copper depleted zones, measured by different authors, in different solutions is presented in Table 2.3. The corrosion potential of AA2090-T8 and of copper rich intermetallic particles are also listed.

In the selection of high strength aluminium alloys for aerospace and aircraft applications the resistance to Stress Corrosion Cracking (SCC) is an important criterion. Anodic dissolution of strengthening precipitate, dissolution of copper depleted zone, hydrogen embrittlement and lithium segregations are proposed mechanisms to explain environmental-induced cracking.

Table 2.3 Summary of corrosion potential of different phase present in Al-Cu-Li alloys according to different authors.

PHASE/ALLOY	Ecorr (mV_{SCE})	Solution*	Reference
α (Al)	- 758	3.5 % NaCl	[90] Li et al.
T1	- 1076	3.5 % NaCl	
T2	- 1228	3.5 % NaCl	
α (Al)	- 855	4 % NaCl	[89] Li et al.
T1	-1076	4 % NaCl	
θ'	-699	4 % NaCl	
α (Al) (AA1100)	-840±56	0.6 M NaCl	[93] Buchheit et al.
T1	-1096±3	0.6 M NaCl	
AA2090-T8	-730±11	0.6 M NaCl	
Al-14Cu	-620	0.6 M NaCl	[94] Buchheit et al.
Al-18Cu-5Fe	-670	0.6 M NaCl	
Al-24Cu-5Fe	-675	0.6 M NaCl	
* Aerated solution			

2.3.7. Effect of temper on corrosion of Al-Cu-Li alloys

Several authors have reported the effect of temper on the size, morphology and distribution of precipitates in Al-Cu-Li alloys [39-42, 44, 95-97]. Considering the role played by active precipitates (see previous Section), different tempers are expected to have different influences on the corrosion behaviour.

The effect of ageing treatment on a stress corrosion behaviour of a Al-2.9Cu-2.2Li-0.12Zr alloy has been investigated by Meletis [97]. The peak aged and two over-aged conditions were investigated. In the peak aged condition, δ', θ' and T1 were the strengthening phases that observed. The subgrain boundaries were found decorated with large T1 precipitates. Even if none of the three tempers showed a well-defined plateau crack velocity, a comparison in terms of crack velocity and stress intensity factor shows that overageing has a detrimental effect on stress corrosion resistance (Fig. 2.29).

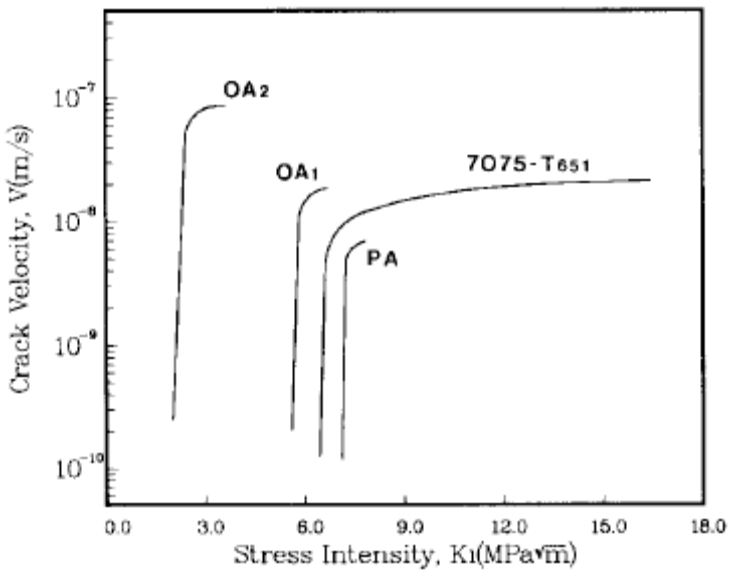

Fig. 2.29 Stress-corrosion crack growth rate *vs.* stress intensity for the three A1-2.9Cu-2.2Li-0.12Zr tempers and 7075-T651 alloy [97].

A reduction of the ratio between tensile strength and stress-corrosion strength, observed increasing the ageing time, confirm the adverse effect of the overageing. TEM studies showed that an increase of the ageing time produces microstructural changes that result in phases with higher chemical reactivity: the transformation of θ' in T1 and, besides the coarsening of the δ' precipitates, the increase of nucleation and growth of δ (which contains more lithium than δ ') at subgrain boundaries. The presence of coarse T1 precipitates at grain boundaries and the development of grain boundaries strain were considered to induce stress corrosion susceptibility in the over-aged temper.

In an Al-Cu-Li-Zr alloy containing Sc in the T6 condition, it was observed that the artificial ageing significantly influenced intergranular and exfoliation corrosion. At 160 °C, the size and the distribution of the main strengthening precipitate (T1), changed with the ageing time from the under to over-aged condition. In the under-aged condition there are few T1 precipitates in the matrix and at grain boundaries; in the over-aged condition, the T1 precipitates are coarse at grain boundaries leading to a wide PFZ; in the peak-aged condition T1 are observed in the matrix with a fine and uniform distribution. The depth of intergranular attack, the exfoliation susceptibility and the major electrochemical parameters (such corrosion

potential and corrosion current density), determined from polarization curves in EXCO solution, were found to increase with ageing time.

In Al-Cu-Li alloy, containing small amounts of Mg, Zn, Mn and Zr, it was observed that different tempers, T6 and T8 (stretched before ageing), show different corrosion susceptibility [98]. The higher exfoliation susceptibility of T6 alloy was related to T1 precipitates at grain boundaries since these were observed to be larger in size and number compared with the T8 (Fig. 2.30) .

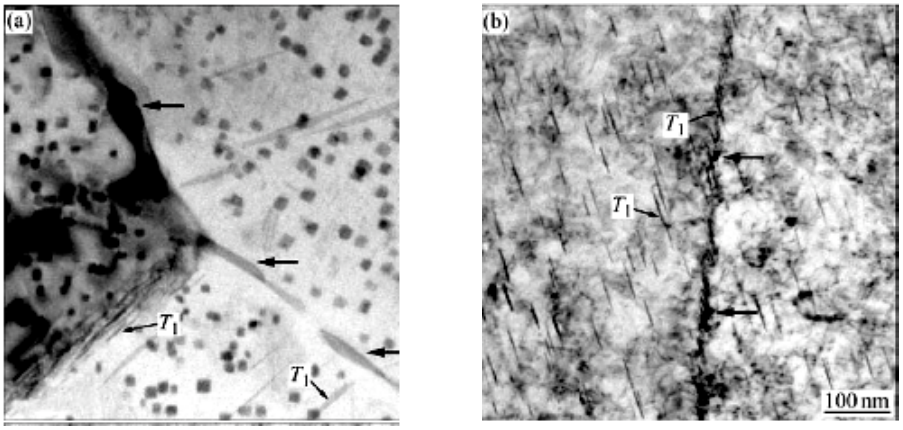

Fig. 2.30 TEM images of grain boundary of Al-Cu-Li-Mg-Mn-Zn-Zr alloy (a) T6 and (b) T8 [98].

2.3.8. Corrosion of Al alloys Friction Stir Welds

As discussed in the previous sections, even if FSW is a solid state process, significant modifications in microstructure, size and distribution of the precipitates occur and, therefore, a change in the corrosion behaviour must be expected.

Despite the increasing interest in developing the third generation of Al-Li alloys to obtain high strength and high toughness alloys and the successful applications of FSW process to aluminium alloys containing lithium, to date, relatively little research has been conducted on the corrosion behaviour of Al-Cu-Li friction stir welds. Research has tended to focus on other aluminium alloys, particularly 7XXX and 2XXX aerospace alloys.

Lumsden et al. have investigated the susceptibility to intergranular corrosion of a AA7075-T651 FSW [99]. The greatest susceptibility was found in the hottest regions within the HAZ. The corrosion attack was correlated with sensitisation occurring during the weld process leading to the formation of copper-depleted regions along the grain boundaries. Polarization curves showed that the HAZ had the lowest pitting potential, followed by the nugget and by the base material.

Sensitisation of the weld has been reported in a AA7108 T9 FSW [100]. Non-uniform distribution of η/η' ($MgZn_2$) within the TMAZ has been reported to be the cause of intergranular attack in this region.

Nugget and TMAZ has been observed as the most corrosion susceptible weld region in AA7050 but post welding heat treatment, operated for 25 minutes at temperatures ranging from 115 °C to 215 °C, decreases the corrosion susceptibility [101].

AA2024-T351 FSW has been found to be susceptible to intergranular corrosion in the nugget and HAZ and a correlation with the welding parameters was observed [51]. Low rotation speeds increase the anodic reactivity of the nugget, and subsequent corrosion attack was found in this region, while for high rotation speeds prevalent attack was found in the HAZ due to the sensitisation of grain boundaries. High cathodic reactivity was observed in the nugget and related to the precipitation of coarse S-phase particles.

In Al-2.05Li-2.70Cu-0.6Mg-0.3Zn FSW, after G110 immersion test pitting, intergranular and inter-subgranular attack was found in base material, HAZ and TMAZ and intergranular and pitting attack in the nugget. Nugget and both HAZ showed the greatest decrease in SCC resistance and the HAZ in the retreating side was found having the higher susceptibility to environmentally assisted failure [102].

The corrosion of AA2195 and AA2024 friction stir welds has been evaluated by Corral et al. [103] using immersion test in 0.6 M NaCl solution and potentiodynamic polarization curves in the same solution. For the AA2125 FSW, after immersion test, an even amount of built-up product on the base metal and in the FSW

zones was observed (Fig. 2.31a and b). Similar behaviour for the weld region and the base metal was found after potentiodynamic measures (Fig. 2.31c).

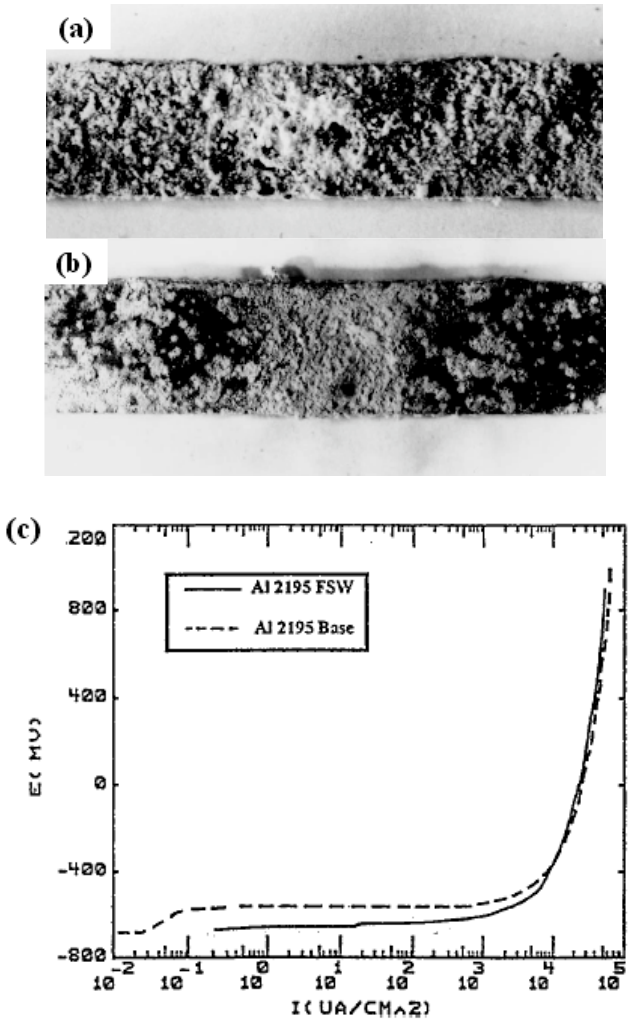

Fig. 2.31 AA2195 FSW after immersion test in 0.6 M NaCl solution after (a) 20 h and (b) 25 days.
(c) Potentiodynamic curves measured in the weld zone and in the base metal [103].

CHAPTER 3 Experimental Method

3.8. Material Composition

A commercial AA2050-T34 FSW was supplied by Alcan-Centre de Recherches de Voreppe (CRV) with a plate thickness of 20 mm. The FSW was performed by Alcan-CRV on a solution heat treated and stretched 3.5% plate (T34), with the welding parameters shown in Table 3.1. One sample was supplied in the T34 condition (with no post weld heat treatment) and one sample in the T34-T8 condition (with 18h at 155°C post weld heat treatment).

Table 3.1 Welding process parameters

Alloy	Thickness [mm]	Tool	Pin length [mm]	Shoulder [mm]	Rotation speed (rpm)	Traverse speed [mm/min]	Rotation direction	Force [N]
AA2050 T34	20	CRV conical triflat	16	30	250	200	Clockwise	52

The nominal chemical composition of the alloy is shown in Table 3.2.

Table 3.2 Major alloy elements and limits according to The Aluminum Association for AA2050 [31]

Element	Composition (wt%)	Composition limits (wt%)
Cu	3.49	3.2 – 3.9
Li	0.83	0.7 – 1.3
others	1.38	-
Al	Balance	Balance

3.9. Sample Preparation

Specimens were sectioned from the friction stir welded plate. Cross sections were taken perpendicular to the welding direction (and perpendicular to the hot rolling direction of the plates) with dimension of about 100 x 10 mm (see Fig. 3.1).

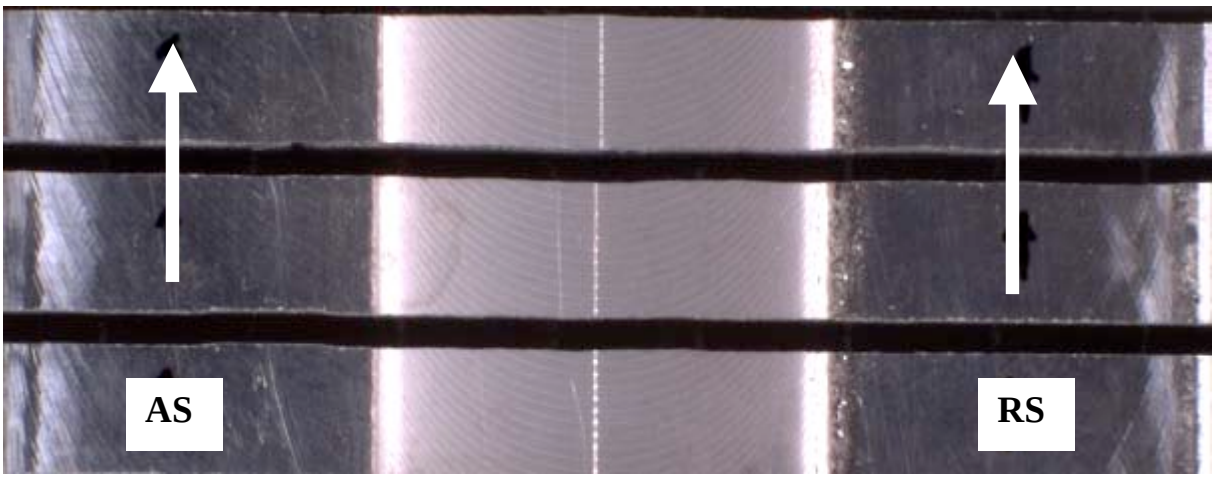

Fig. 3.1 AA2050 FSW specimen. AS Advancing Side. RS Retreating Side

The 20 mm thick samples were machined 2 mm from the top surface and 7 mm from the bottom (see Fig. 3.2).

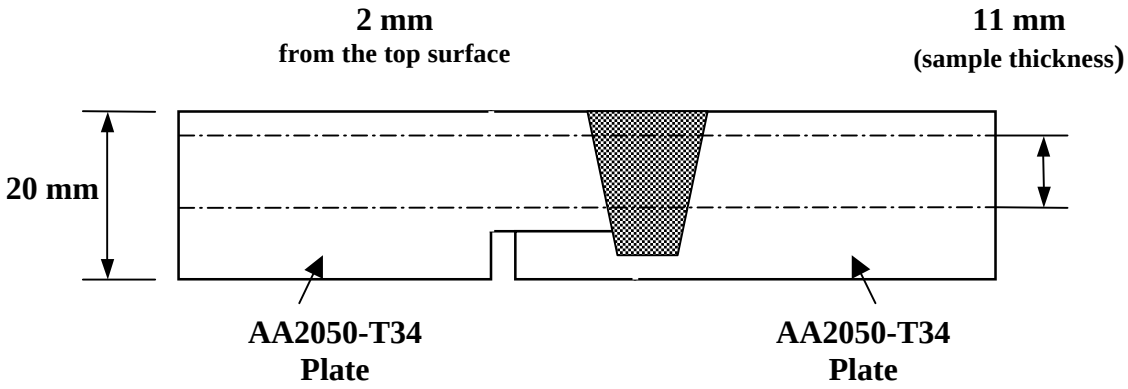

Fig. 3.2 Welding configuration and position of the samples

All samples were ground down to 4000 grade with successive grades of SiC paper (120/800/1200/4000) and polished with 3 micron and 1 micron Struers-DP diamond suspension. All grinding and polishing were performed with Struers alcohol based lubricant in place of water. Before electrochemical measurements, immersion tests, optical and scanning electron microscopy (SEM) characterization, samples were ultrasonically cleaned with ethanol. In all cases, during sample preparation, contact with water or water-containing solutions was avoided.

3.10. Heat treatment

Artificial ageing treatments were performed in an ELITE TEHERMAL SYSTEM furnace for different ageing time. Table 3.3 summarized the five different post welding heat treatment.

Table 3.3 Post Welding Heat Treatment (PWHT) conditions

Natural Ageing	T34
3h at 155 ºC	T34-T8 (3 h)
18h at 155 ºC	T34-T8 (18 h)
36h at 155 ºC	T34-T8 (36 h)
72h at 155 ºC	T34-T8 (72 h)

The AA2050 plate was solution heat treated (SHT) and then stretched by 3.5%. FSW 2-3 weeks, after SHT and stretching. The post welding treatment was performed after 1 year. The processing route is shown schematically showed in Fig. 3.3.

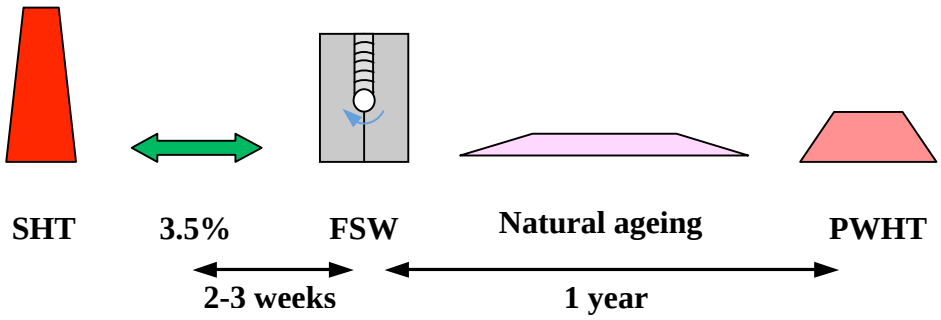

Fig. 3.3 Processing route

3.11. Micro Hardness Testing

Microhardness profiling was performed using a Mitutoyo MVK-H1 hardness-testing machine, with a load of 50 g, along the mid line of the transverse cross section of the weld. A Vickers indenter was used. Prior etching of the surface tested was performed in order to define the different regions of the weld.

3.12. Microstructural Characterization

Microstructure evolution across the weld was observed using a Leica optical microscopy. Prior etching with Keller's reagent on the polished surface was carried out. After etching specimens were rinsed with ethanol.

3.13. Immersion Tests

3.13.1. 0.1 M NaCl immersion test

Samples of the transverse cross section of the 5 different ageing conditions were prepared as described in Section 3.2. Surfaces not under examination and edges of the sample were masked with MacDermid 45 STOPPING-OFF Lacquer. The samples were immersed in naturally aerated 0.1 M NaCl solution at room temperature for 10 days. The volume ratio of solution / specimens was $\geq$ 50 and the temperature was measured between 17 °C and 18.5 °C.

After testing, macro pictures of the transverse cross section surface, exposed to the solution, were taken using a digital camera. In order to define the depth of attack, the corroded surfaces were sectioned (as shown Fig. 3.4), mounted in MetPrep Tri-Hard cold mounting powder, ground and polished, then observed with optical microscope and Field Emission Gun Scanning Electron Microscope (FEG-SEM) JEOL 7000.

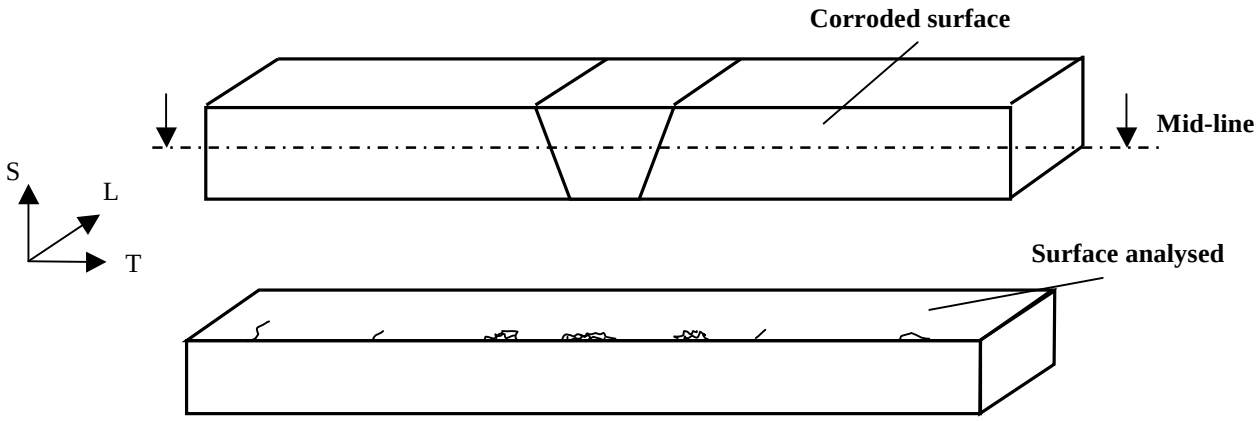

Fig. 3.4 Surface analysed after immersion test

3.13.2. G110 immersion test

An intergranular corrosion test was performed according to ASTM G110 [104]. The test was performed on the T34-T8 (18 h) sample. The sample was prepared as described in Section 3.6.1. for the 0.1 M NaCl immersion test. A solution of 57 g/l (0.98 M) NaCl and 10 ml/l 30% (0.09 M) H_2O_2 was used, in aerated condition, at room temperature. The sample was immersed in the solution for 24 h.

After testing, macro pictures of the transverse cross section surface, exposed to the solution, were taken using a digital camera. After polishing the surface with 1 micron diamond suspension, in order to remove corrosion products, optical and FEG/SEM images were taken in different regions of the weld. The depth of attack was observed as described in the Section 3.6.1.

3.14. Electrochemical Tests

3.14.1. 'Droplet Cell' Potentiodynamic Measurements

The local electrochemical cell, attached in place of an objective lenses of an optical microscope, consisted of a 1 mm diameter plastic pipette tip, a platinum wire counter electrode (CE) and a silver/silver chloride reference electrode (RE) (Fig. 3.5). Counter and reference electrodes were contained in a small plastic device attached to the pipette. A syringe was used to fill the cell with the electrolyte and to control the amount of solution at the pipette tip. Counter, reference and working electrode (WE), the AA2050 FSW samples, were connected to an ACM field machine potentiostat.

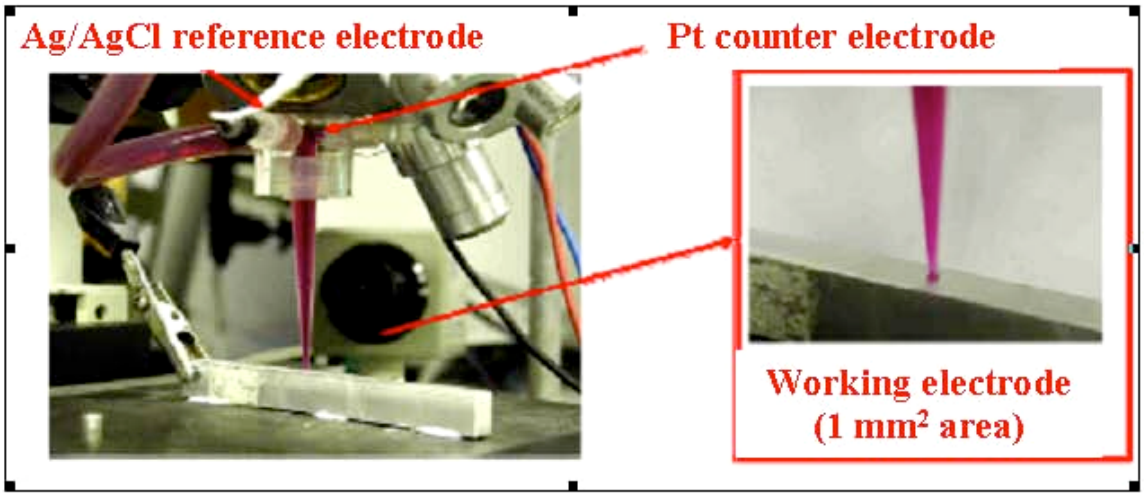

Fig. 3.5 Droplet cell apparatus for localized electrochemical measurements [105]

For each test, the open circuit potential (OCP) was monitored for 300 seconds and then a potentiodynamic sweep was carried out from the OCP at a rate of 1 mV/s. Anodic and cathodic polarization tests were performed separately, starting respectively at -10 mV and +10 mV relative to the OCP. All measurements were carried out in naturally aerated 0.01 M NaCl.

3.14.2. Potentiostatic Measurements

IGC susceptibility for AA2050-T34 FSW in the naturally aged and in the over-aged T34-T8 (72 h) condition was evaluated, for the different regions of the weld, by measuring the current vs. time behaviour at a fixed potential. Measurements were taken with the local electrochemical apparatus described in 3.7.2. The potential was determined from the potentiodynamic polarization curves just below the anodic breakdown potential. In order to promote attack of grain boundaries, naturally-aerated 0.1 M NaCl solution, acidified to pH 2.75 with HCl, was used [90]. After the electrochemical measurements, the sample surface was investigated with SEM.

3.14.3. Long term OCP

The OCP was measured for 24 h for the 5 different post-welding ageing conditions. The samples were ground down to 4000 grade SiC paper. All surfaces, except the transverse cross section surface, were laquered as described in Section 3.6.1. The whole weld was immersed in a beaker containing 500 ml of naturally aerated 0.1 M NaCl. The beaker was immersed in a thermal bath at 25 °C in order to avoid thermal fluctuations during the test. The OCP was measured using an Ag/AgCl as reference electrode. For the T34-T8 (18 h) post-welding ageing treated sample the same test was carried out also in the G110 solution.

CHAPTER 4 Results and discussion

4.5. Microstructure of the AA2050 (base metal)

The AA2050-T34 plate has a highly directional, anisotropic grain structure. Fig. 4.1 shows the elongated pancake-shaped grain structure, typical of a rolled product. The size of the elongated grains is 100-300 μm in the T direction and 20-50 μm in the S direction (Fig. 4.2).

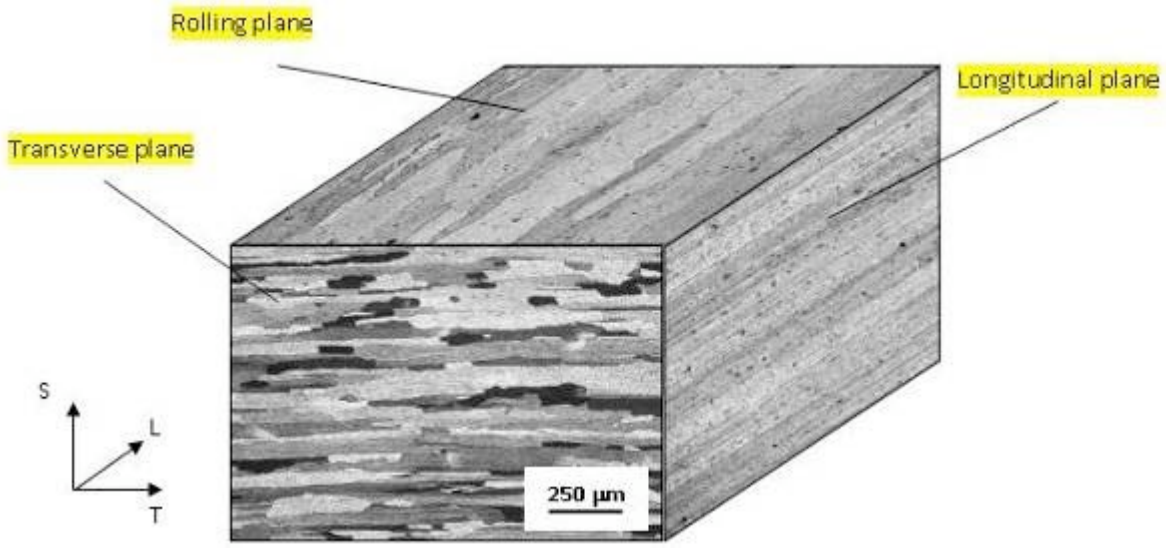

Fig. 4.1 Picture showing the 3D microstructure of the AA2050-T34 rolled plate, after etching with Keller's reagent for 30s

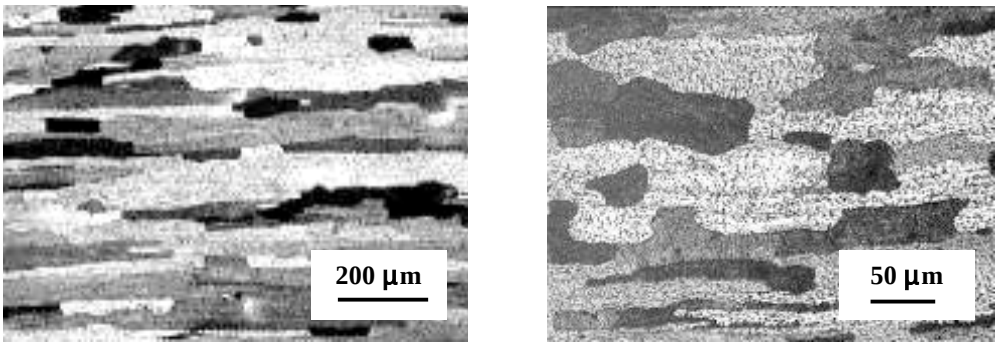

Fig. 4.2 Pictures showing the elongated grains of the AA2050-T34 base metal at different magnifications, after etching with Keller's reagent

FEG/SEM observations reveal the presence of a large number of coarse intermetallic particles that tend to be arranged in sheets parallel to the rolling direction of the alloy (Fig. 4.3). These particles tend to be irregular in shape (Fig. 4.4a) and mainly contain Cu, Mn and Fe (Fig. 4.4b).

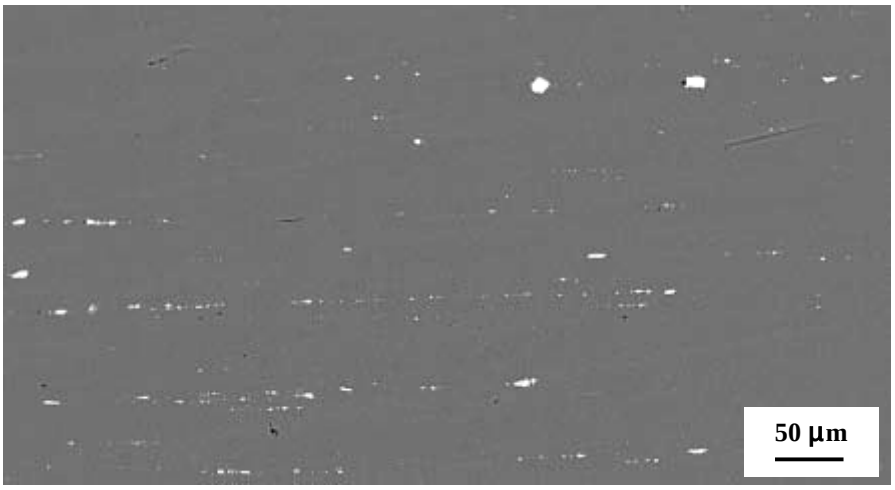

Fig. 4.3 FEG/SEM backscattered electrons image of the AA2050-T34 showing intermetallic particles

(a)

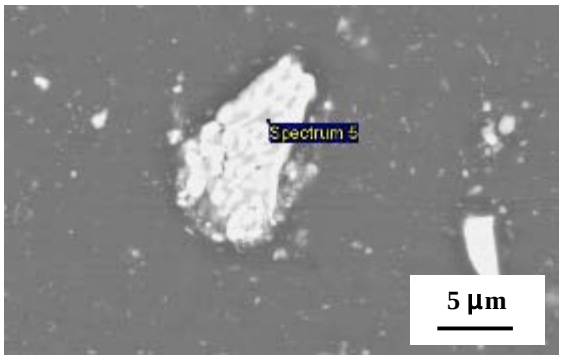

(b)

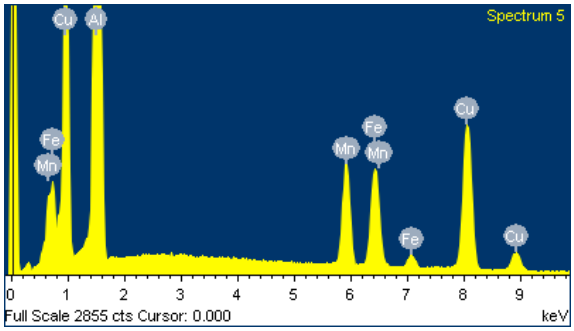

Fig. 4.4 (a) FEG/SEM backscattered electrons image showing intermetallic particles in AA2050-T34. (b) EDX spectrum

4.6. Microstructure of AA2050-T34 FSW

Fig. 4.1 shows a picture of the transverse cross section of the AA2050-T34 FSW. The microstructure in the different regions of the weld is shown in Fig. 4.2.

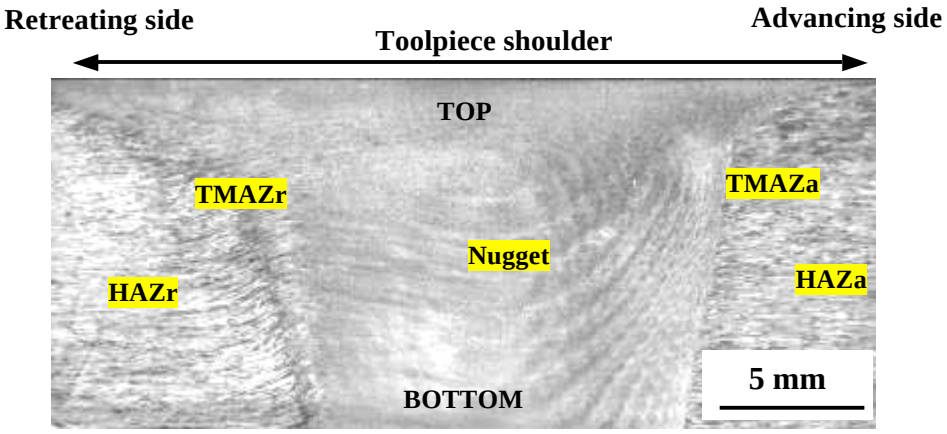

Fig. 4.1 Macrographic picture of the cross section of the AA2050-T34 FSW

The nugget has a fine recrystallised structure [45, 46, 54-59, 107, 108]. The grains are larger close to the bottom surface than at the centre line or close to the top surface as shown on Fig. 4.2 a, b and c. This difference in grain size is mainly due to variations in heat transfer during the welding process [108].

The Thermo-Mechanically Affected Zone (TMAZ), is located at the interface between the recrystallised nugget and the heat-affected zone (HAZ), where the grains are highly deformed during FSW [46, 49, 60]. This region is found on both sides of the weld between 7 mm to 8.5 mm from the nugget centre. The transition appears sharp on the advancing side of the weld (Fig. 4.2 d, e, f), particularly at the bottom of the weld, while it is more gradual and wide on the retreating side (Fig. 4.2 g, h, i). At the retreating side, the transition from nugget to TMAZ is not clearly defined and a partially recrystallised zone is visible as shown in Fig. 4.2 g. The Heat Affected Zone (HAZ) shows elongated grains characteristic of the base metal (Fig. 4.2 j, k).

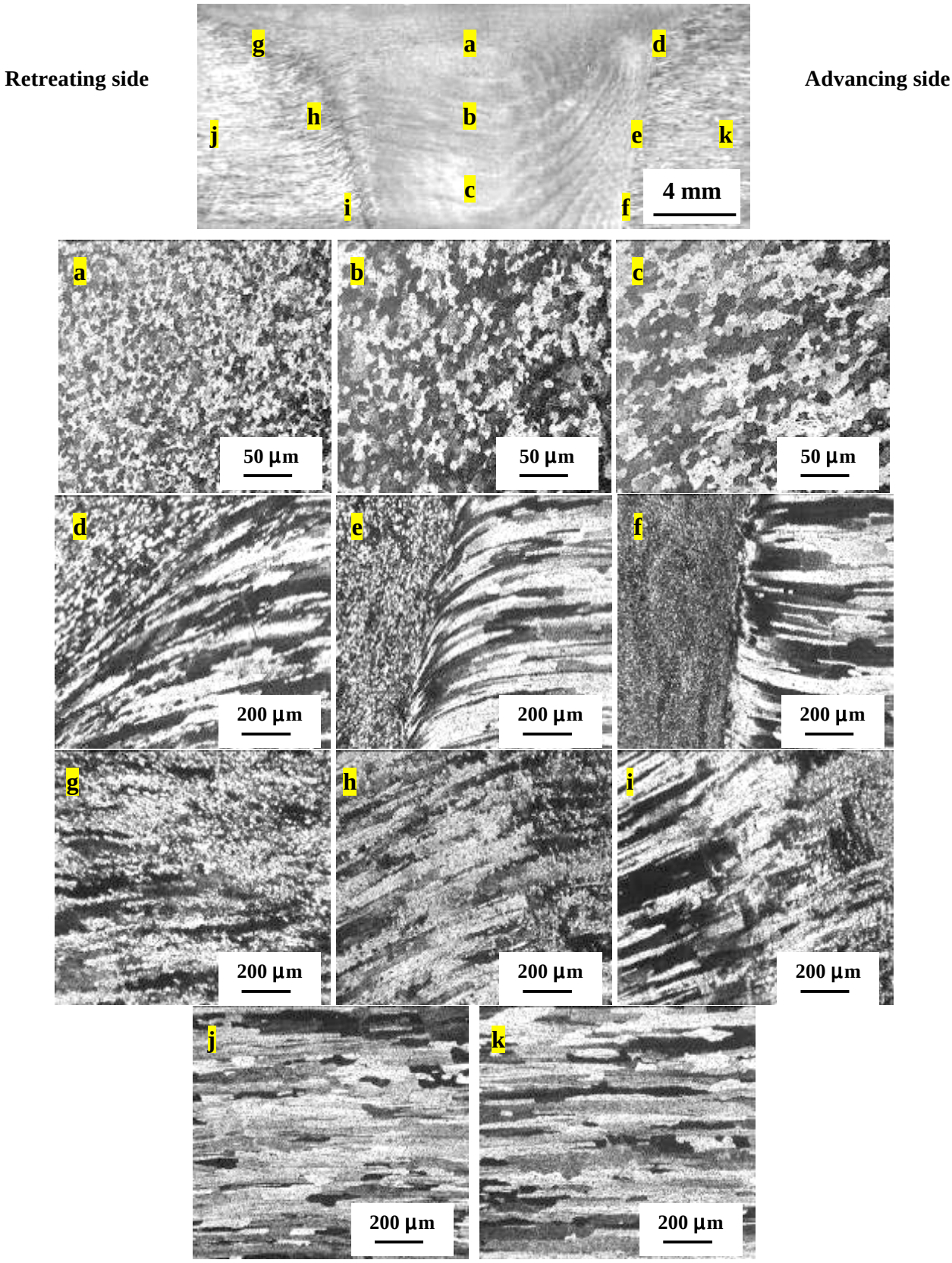

Fig. 4.2 Macrographic picture of the cross section of the AA2050-T34 FSW, after etching with Keller's reagent for 30s, together with detailed micrographs of the different weld regions.

4.7. Microhardness of AA2050-T34 FSW

The change in the hardness resulting from the welding process was determined by Vickers microhardness along the mid line of the transverse cross section of the weld (Fig. 4.3).

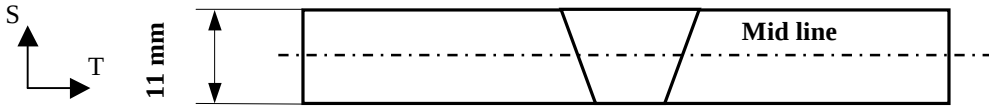

Fig. 4.3 Position of the Vickers microhardness profiles

Microhardness measurements performed on the etched samples were also used to identify the different regions of the weld. In the advanced side, the border between nugget and TMAZ is located at 7 mm from the centre of the weld (Fig. 4.4 a); TMAZ extents till 8.5 mm where a slight deformation of grains is still observed (Fig. 4.4 b); the HAZ starts at 9 mm grains, where grains appear not deformed along the rolling direction (Fig. 4.4 c).

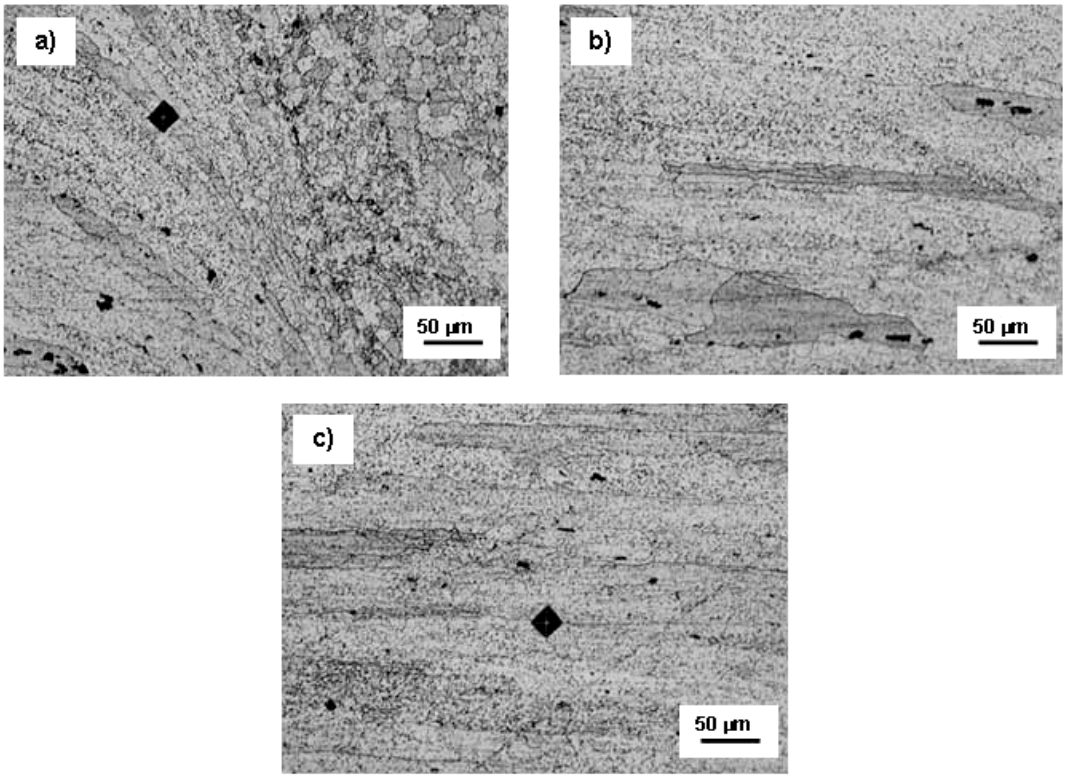

Fig. 4.4 AA2050-T34 FSW after etching: a) Nugget – TMAZ border; b) TMAZ; c) HAZ in the advanced side

On the retreating side, the border between nugget and TMAZ is located at 6.5 mm; compared to the advanced side, a less sharp separation between the two region is observed (Fig. 4.5 a). From 7 mm (Fig. 4.5 b) to 8 mm, the deformation of grains appears more evident; at 9mm (Fig. 4.5 d) grains still appear deformed. The HAZ is located at 9.5 - 10 mm where the grains appear not deformed along the rolling direction (HAZ) (Fig. 4.4 c).

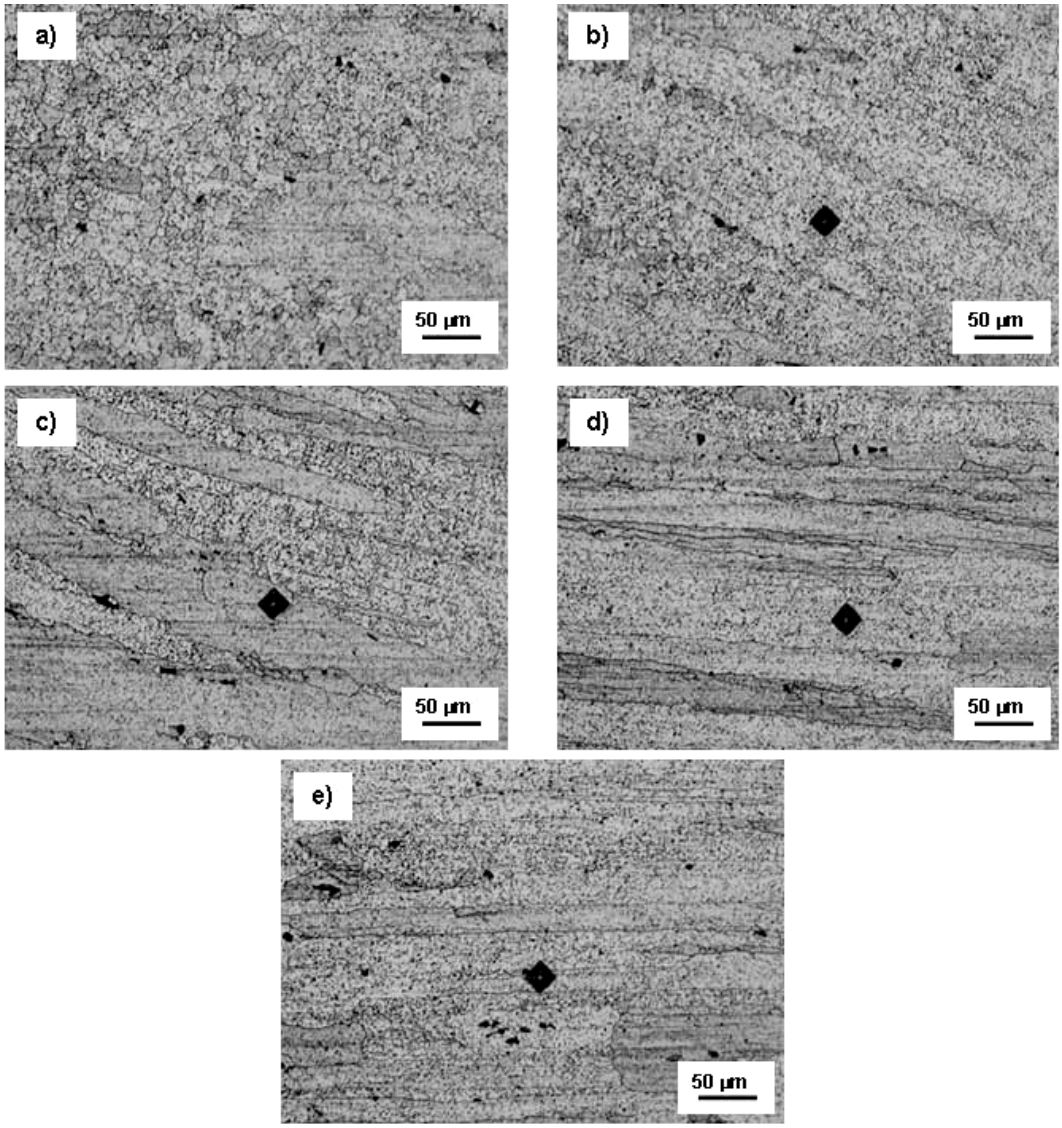

Fig. 4.5 AA2050-T34 FSW after etching: a) Nugget – TMAZ border; b), c), d) TMAZ; e) HAZ in the retreating side

The microhardness profiles for the five different post weld heat treatments conditions are presented in Fig. 4.6.

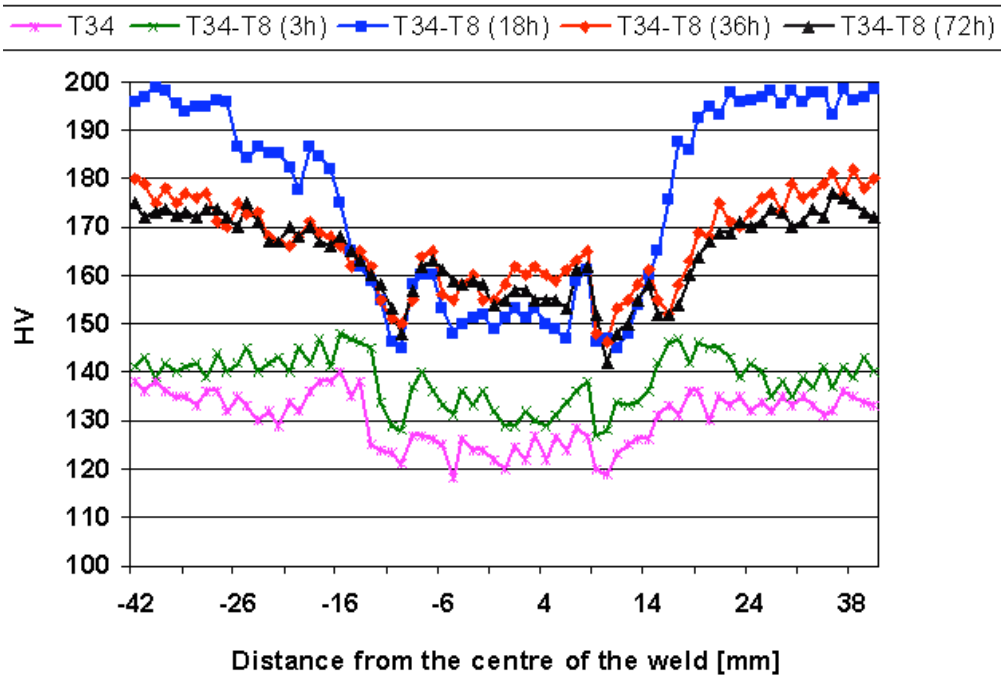

Fig. 4.6 Vickers microhardness profiles at mid-line of the cross section of the weld for the five different post weld heat treatment conditions.

For all conditions, a drop in hardness in the weld region was observed. This softening is related with the coarsening and/or dissolution of strengthening precipitates during the thermal cycle of the FSW [45, 64]. Post weld heat treatment lead to an increase in hardness values.

The base material beyond the HAZ is not subjected to any thermal heating during the FSW process, therefore the effect of ageing on this region is the precipitation of the main strengthening phase and the resulting increase in the hardness. At the ageing temperature (155°C) the main strengthening precipitate is reported to be T1 [42]. In the over-aged conditions, T34-T8 (36 h) and T34-T8 (72 h), the decrease in hardness, compared with the T34-T8 (18 h), is related to the coarsening of precipitates [39, 42].

The maximum hardness was found in the base metal after 18h at 155 °C, while further ageing at this temperature leads to a decrease of hardness. Heat treatment leads to an increase in this region from about 140 HV, in the naturally-aged condition, to 200 HV after 18h at 155 °C.

In the HAZ, the decrease in hardness is a consequence of the overageing caused by the thermal transient during welding: this is generally observed when alloys in the T6 or T8 conditions are processed with slow welding parameters [111]. or all post welding conditions the minimum hardness in HAZ was found at 10-11 mm from the centre of the weld. From Fig 4.4 (c) and 4.5 (e) it was possible to locate HAZ starting at 9 - 9.5 mm from the centre of the weld up to 20 mm, where significantly difference in hardness is observed compared with the base alloy (Fig. 4.6).

The hardness in HAZ, at the interface with TMAZ, was found to be lower, for all five PWHT (post weld heat treatment) conditions, than in the TMAZ. The drop in hardness in HAZ is particularly evident in the T34-T8 (18 h), (32 h) and (72 h) conditions. The thermal transient in this region lead to a coarsening of precipitate distributions and consequent overageing of the alloy [62, 111].

In the TMAZ hardness was found higher than the HAZ, particularly in the T34-T8 (18 h), (32 h) and (72 h) and less evident in the T34-T8 (3 h) and T34 condition.

Compared with the nugget, the TMAZ hardness was found higher in the T34-T8 (3 h), (18 h), (32 h) and (72 h); in the T34 weld similar hardness were in these two regions.

After welding, depending on the alloy composition and welding parameters, one of the following should be expected:

- if the weld nugget is over-aged, then ageing treatment will have either no effect or cause a slight decrease in the nugget hardness;

- if the nugget has been left in the solid solution condition, then post weld ageing should enable recovery of properties similar to that of the base metal;
- if the nugget is partially solution treated, post weld heat treatment should result in some hardening [61, 62, 109].

After post weld heat treatment, a gradual increase hardness is observed in the weld region (Fig. 4.6). This increase is up to 40 HV from the T34 to the T34 (36 h) condition. G. Pouget, A.P. Reynolds observed similar behaviour in AA2050 T8 FSW, with and without post weld heat treatment (15 h at 160°C) [70].

4.8. Immersion tests in 0.1 M NaCl for 10 days

A series of weld cross sections in the different post weld heat treatment conditions were immersed in 0.1 M NaCl for 10 days, as described in Section 3.6.1. Macroscopic images of the transverse cross section of the weld after immersion are shown in Fig. 4.7.

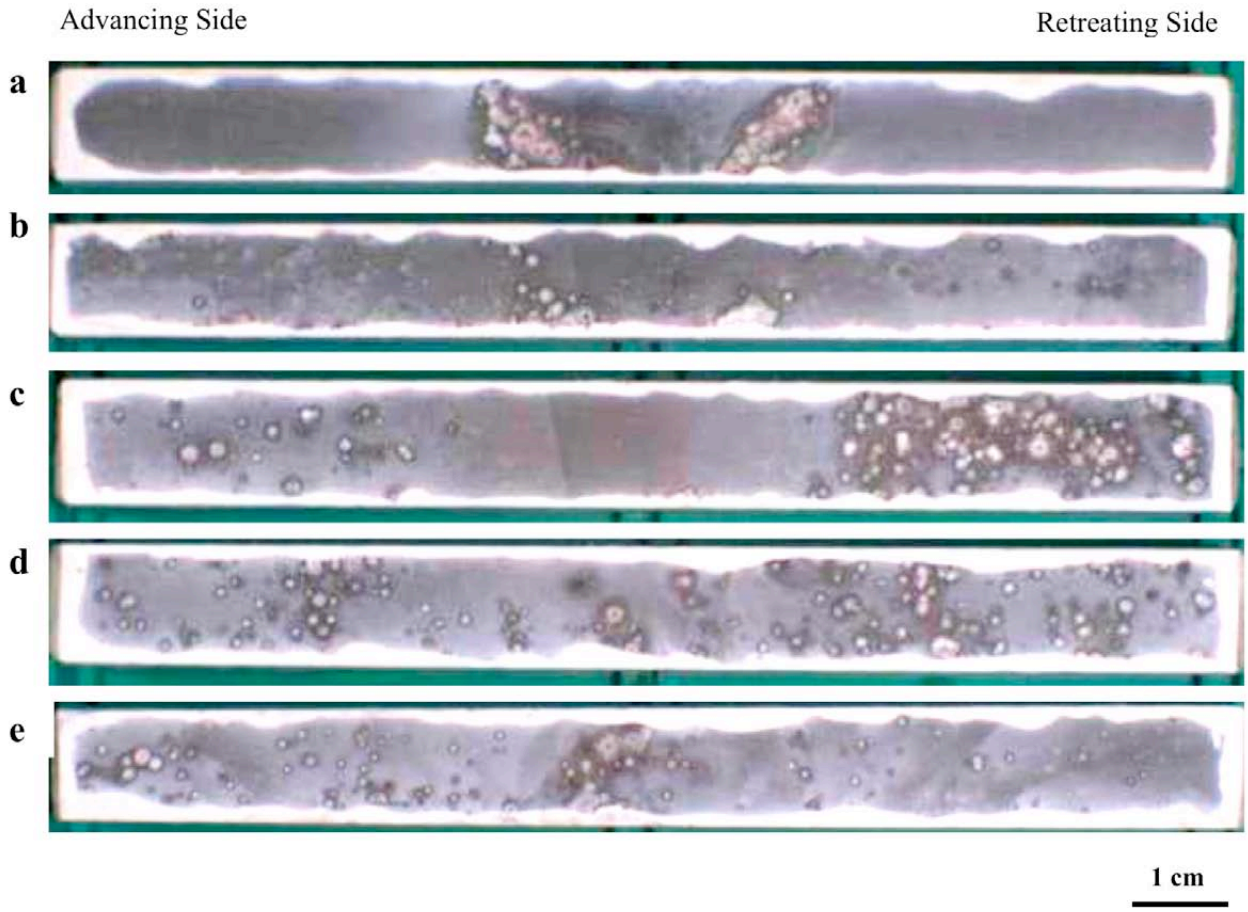

Fig. 4.7 Macrograph of AA2050-T34 FSW after immersion in 0.1 M NaCl for 10 days, for the five different post weld heat treatment conditions:
(a) T34, (b) T34-T8 (3h), (c) T34-T8 (18h), (d) T34-T8 (36h), (e) T34-T8 (72h)

In the post weld naturally-aged sample (Fig. 4.7 a) the attack is localized in the HAZ. In the TMAZ, near the weld root (the bottom part of the weld), a large pit is visible. The nugget is mildly attacked. The base metal appears corrosion resistant.

In the T6-T8 (3h) sample (Fig. 4.7 b), the attack is localized in the HAZ, predominately near the weld root. In the TMAZ near the weld root a large pit is visible. The base metal and the nugget are mildly attacked.

In the T6-T8 (18h) sample (Fig. 4.7 c) the attack is localized in the base metal while no evident signs of attack are visible in the other regions of the weld.

In the T6-T8 (36h) sample (Fig. 4.7 d) the corrosion products are uniformly distributed along the weld.

In the T6-T8 (72h) sample (Fig. 4.7 e) the attack is localized in the nugget. Less attack is visible in the other regions, where the corrosion is uniformly distributed.

The depth of attack and the corrosion morphology were evaluated by sectioning the samples, as described in Section 3.6.1., and the result are exposed in the following five sections.

4.4.1. AA2050-T34 FSW – Naturally aged

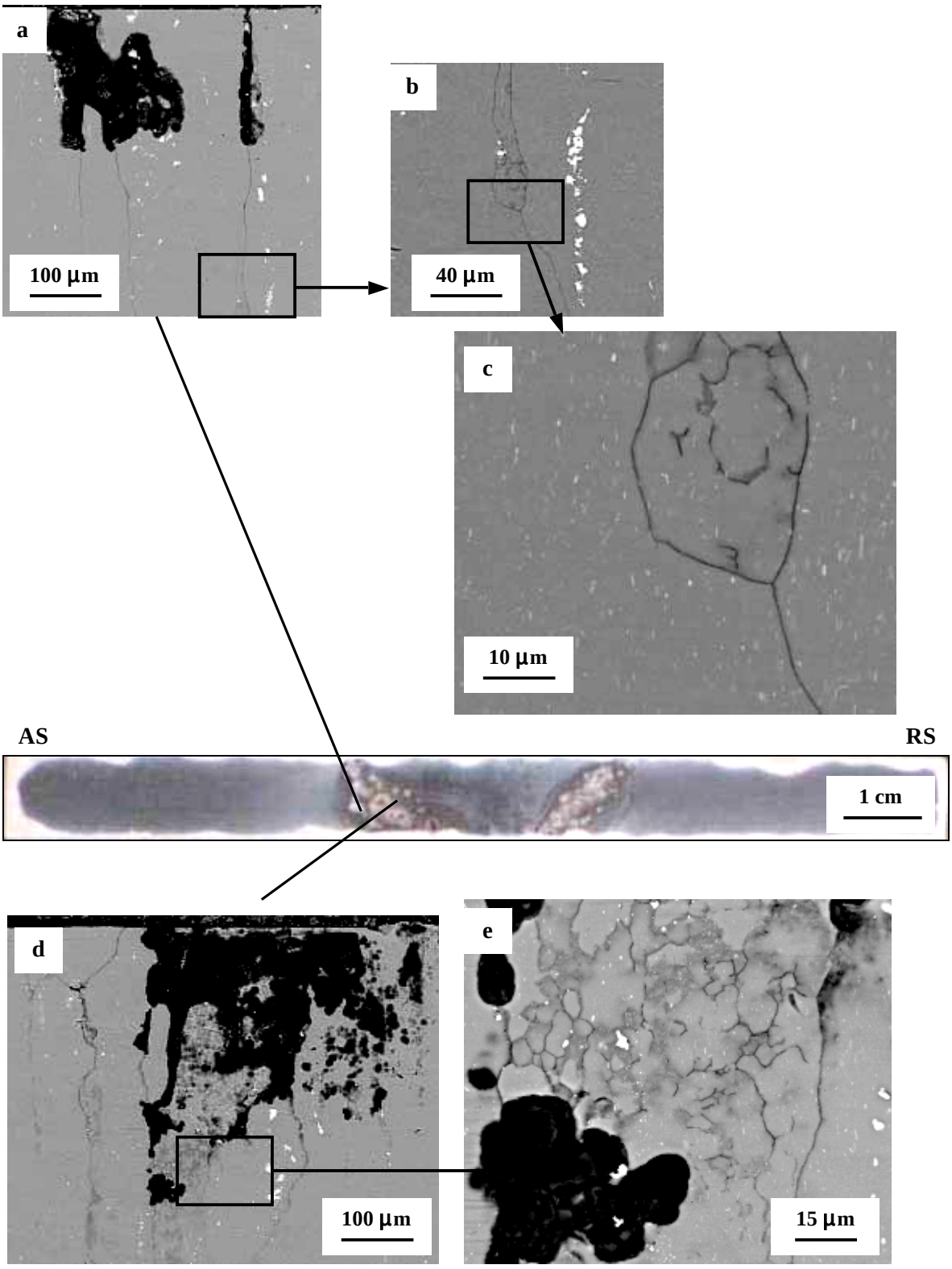

Fig. 4.8 FEG/SEM backscattered electrons images showing the corrosion attack in the TL section of the AA2050-T34 FSW: (a),(b),(c) HAZ advancing side; (d),(e) TMAZ advancing side

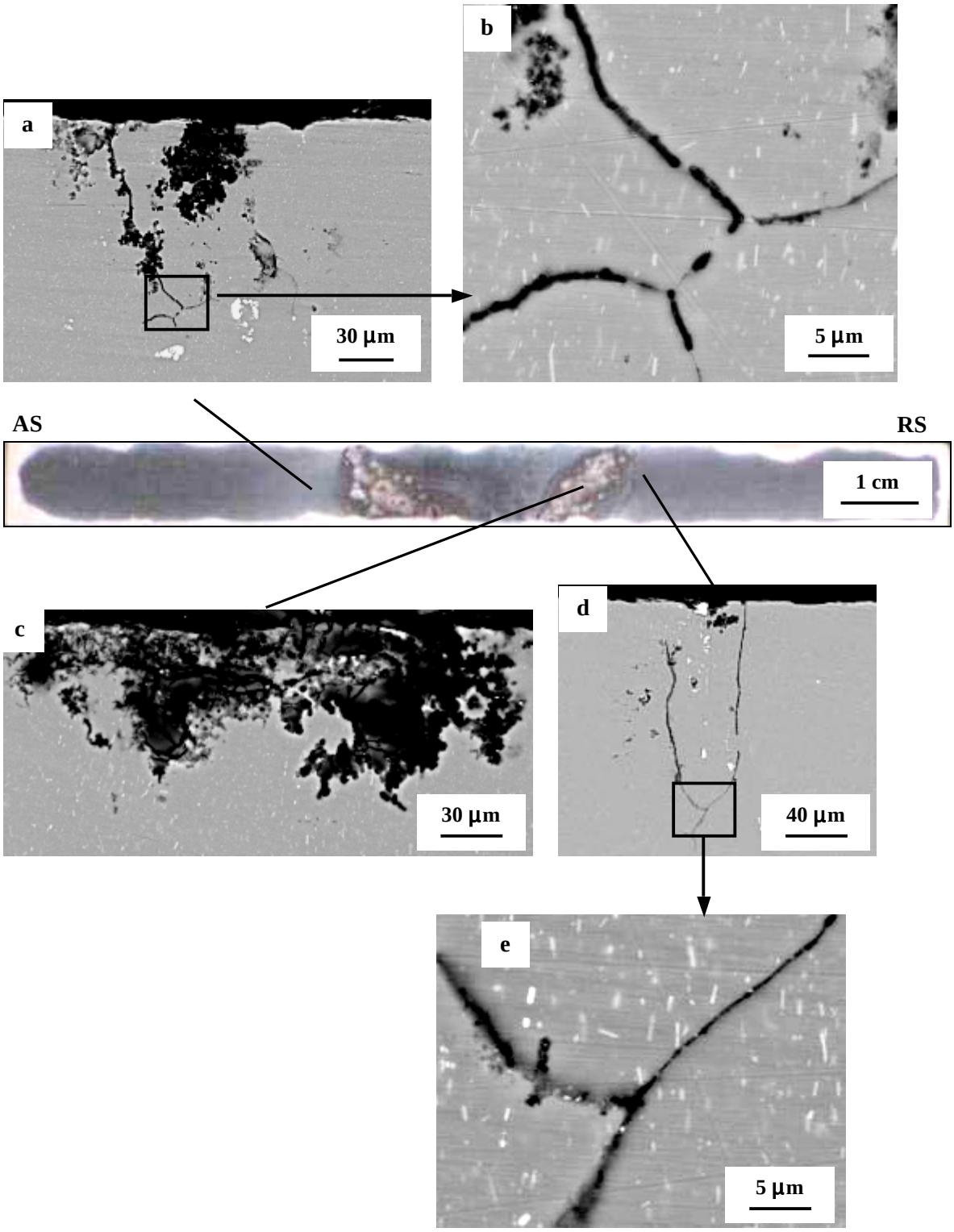

Fig. 4.9 FEG/SEM backscattered electrons images showing the corrosion attack in the TL section of the AA2050-T34 FSW: (a),(b) HAZ advancing side (c), (d), (e) HAZ retreating side

For the naturally-aged sample, on both sides of the weld the HAZ showed the more severe attack. Intragranular corrosion was found in several observations (Fig 4.9 c). Large cavities and pits were also found (Fig 4.8 a). Attack at a grain boundary was found deep in the bulk, up to 350-400 μm (Fig. 4.8 b-c). In the TMAZ, the attack was found to be severe, with both intra- and intergranular attack (Fig. 4.8 d-e). At the interface between HAZ and base metal (at around 20-25 mm from the weld centre), were the alloy had still been subjectected to thermal heating, several regions of intergranular attack were found (Fig 4.8 a-b and Fig. 4.9 d-e). The TL sections of the sample, in the nugget and in the base metal, didn't show any evident signs of attack even though the corroded surface (the surface exposed to the solution) showed shallow grooves around the copper-containing intermetallic particles (Fig. 4.10 a-b). This kind of attack was also present for the other weld regions (Fig. 4.10 c refers to the TMAZ retreating side) and observed in every post weld heat treatment condition.

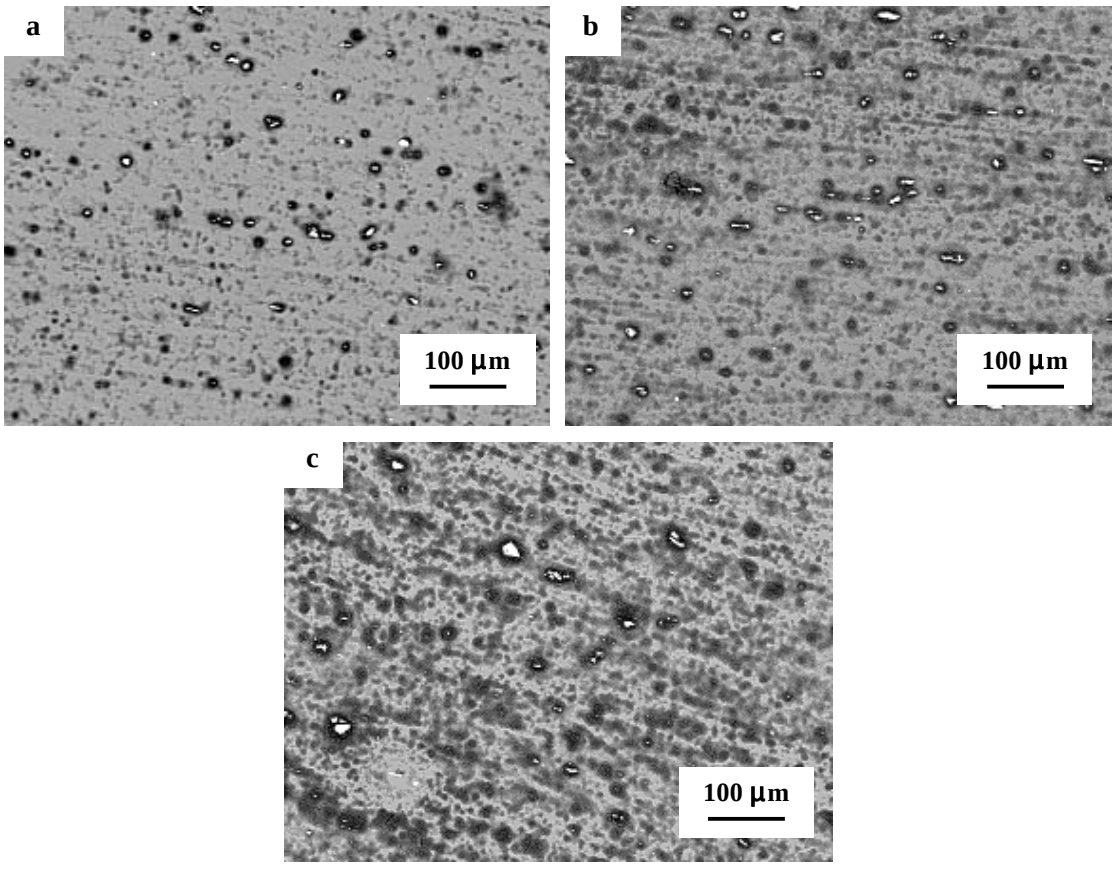

Fig. 4.10 FEG/SEM backscattered electrons images showing the corrosion attack for the surface exposed to the solution AA2050-T34 FSW: (a) base metal; (b) nugget; (d) TMAZ retreating side

5.4.2. AA2050-T34 FSW – T8 (3h)

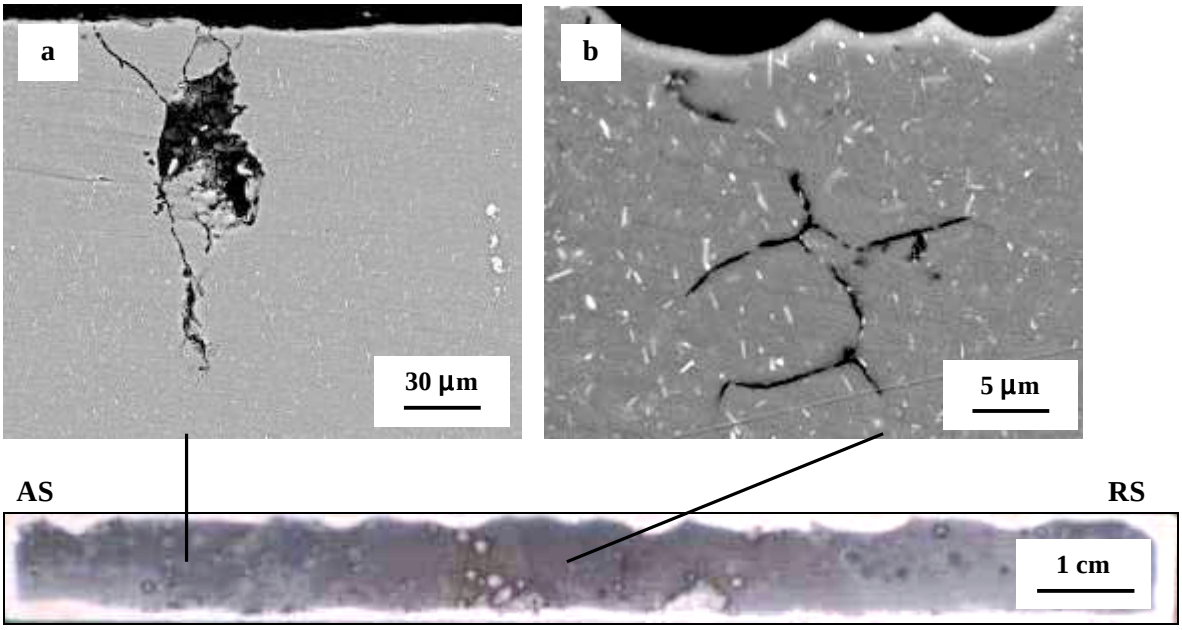

Fig. 4.11 FEG/SEM backscattered electrons images showing the corrosion attack in the TL section of the AA2050-T34 FSW – T8 (3h): (a) base metal; (b) nugget

On the sample aged for 3 hours, the base metal was found to be mildly corroded, with the most prevalent attack at grain boundaries and, in a few cases, intragranular corrosion was also found (Fig. 4.11 a). The nugget was generally found to be corrosion resistant, with just a single observation of attack at grain boundaries (Fig. 4.11 b). On the corroded surface, as observed for the T34 FSW – natural aged sample, several grooves associated with copper-containing intermetallic particles, were found (not shown).

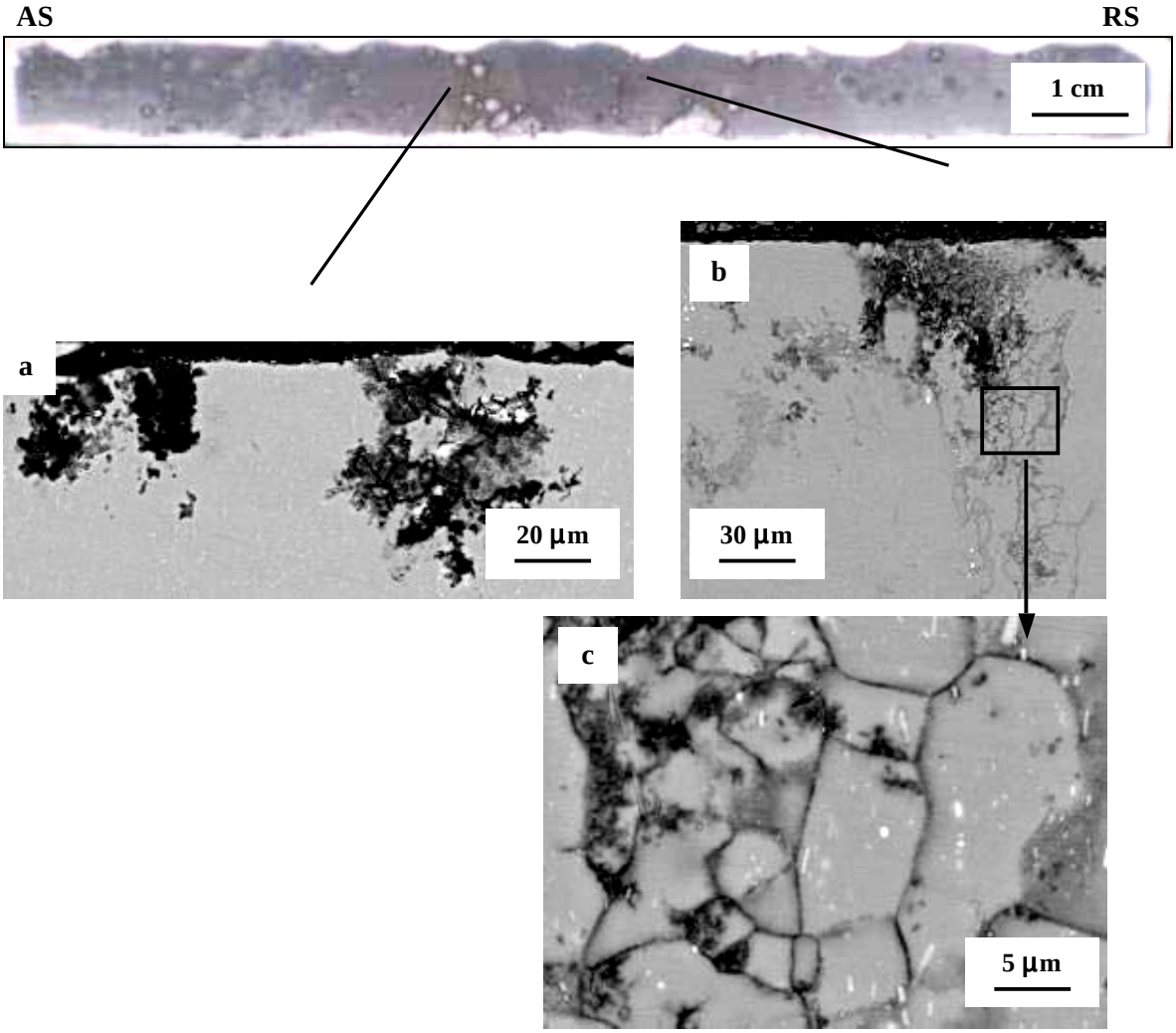

Fig. 4.12 FEG/SEM backscattered electrons images showing the corrosion attack in the TL section of the AA2050-T34 FSW – T8 (3h): (a) HAZ advancing side; (b),(c) interface between TMAZ retreating side and Nugget

On both sides of the weld, in the HAZ intragranular attack was found (Fig. 4.12 a refers to the advancing side). In the TMAZ, on both sides of the weld, the attack is visible both at grain boundaries and inside the grains (in Fig. 4.12 b refer to the retreating side). At the interface between TMAZ and nugget the attack is prevalent at grain boundaries (Fig. 4.12 c). Compared with the natural aged condition, for both regions (HAZ and TMAZ) and both sides, the attack was found to be less severe.

4.4.5. AA2050-T34 FSW – T8 (18h)

Immersion test in 0.1 M NaCl for 10 days was performed on two samples, one was heat treated, after welding, in Birmingham and one was heat treated in Alcan. Fig. 4.7 c referred to the sample heat treated in Birmingham while Fig. 4.13 refers to the one heat treated in Alcan, than exposed to 0.1 M NaCl in Birmingham. Results are consistent: the attack is localized in the base metal, while no signs of evident attack are visible in the other regions, except for a big pit in the TMAZ near the weld root.

Fig. 4.13 Macrograph of AA2050-T34 FSW - T8(18h) after immersion in 0.1 M NaCl for 10 days

Before sectioning the sample, images of the corroded surface were taken in the different regions. In the base metal (Fig. 4.14 A) several, large and elongated pits were found. The same kind of pits are visible in the HAZ region, but they appear smaller in dimension (Fig. 4.14 B and C). Less attack was found in the nugget (Fig. 4.14 F) and in TMAZ (Fig. 4.14 E). In the TMAZ, on the advancing side, near the weld root, a large pit was observed (Fig. 4.14 D).

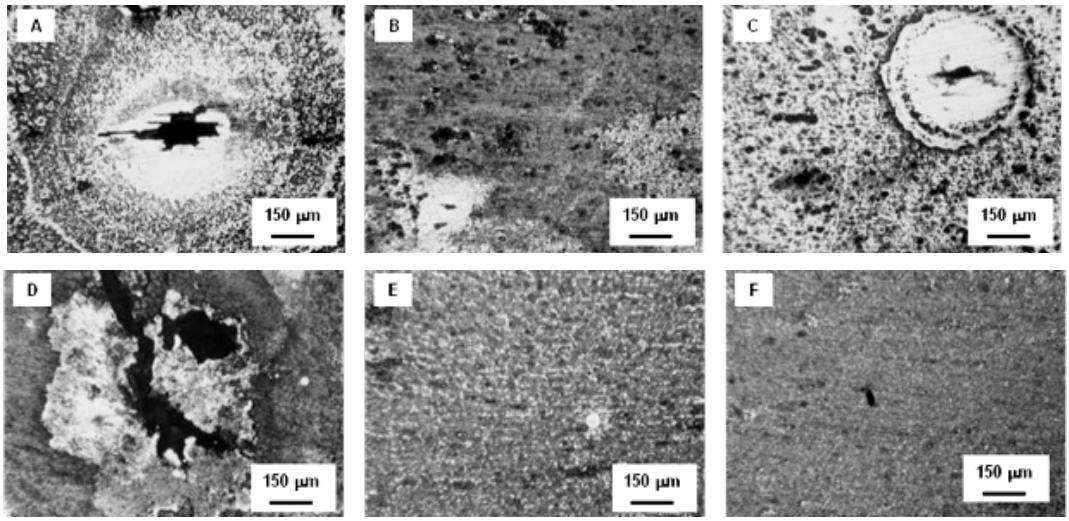

Fig. 4.14 Optical images of the corroded surface of AA2050-T34 FSW-T8(18h) after immersion test in 0.1 M NaCl for 10 days: (A) base metal; (B) HAZ advancing side; (C) HAZ retreating side; (D) TMAZ advancing side; (E) TMAZ retreating side; (F) nugget

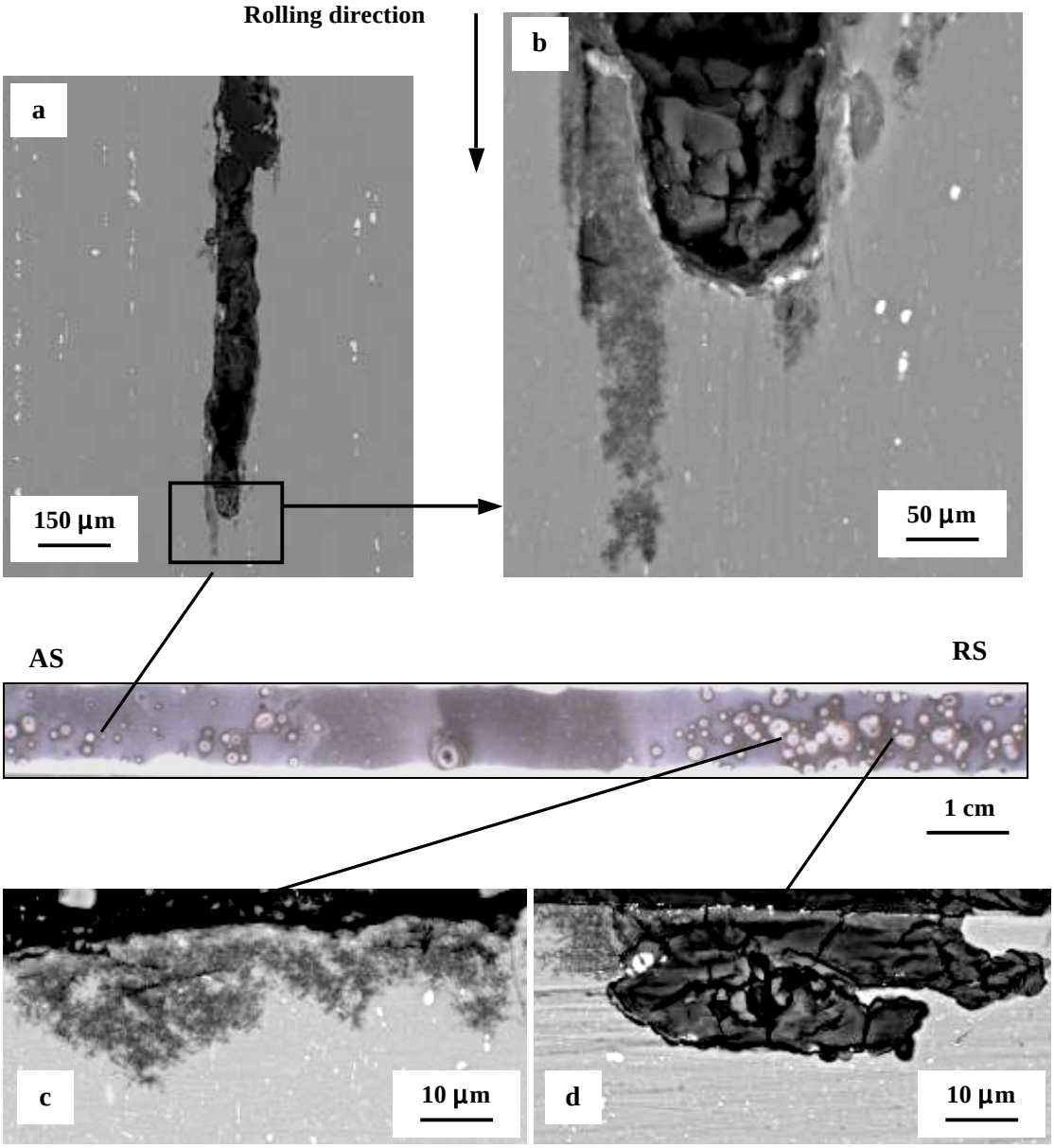

Fig. 4.15 FEG/SEM backscattered electrons images showing the corrosion attack in the TL section of the AA2050-T34 FSW – T8 (18h): (a)-(d) base metal

Following cross sectioning parallel to the plate, in the base metal long pits along the rolling direction were found (Fig. 4.15 a). Large cavities were also visible (Fig. 4.15 d). Several observations of intragranular attack were found (4.15 c), often localized at the border of pits or cavities (Fig. 4.15 a and b).

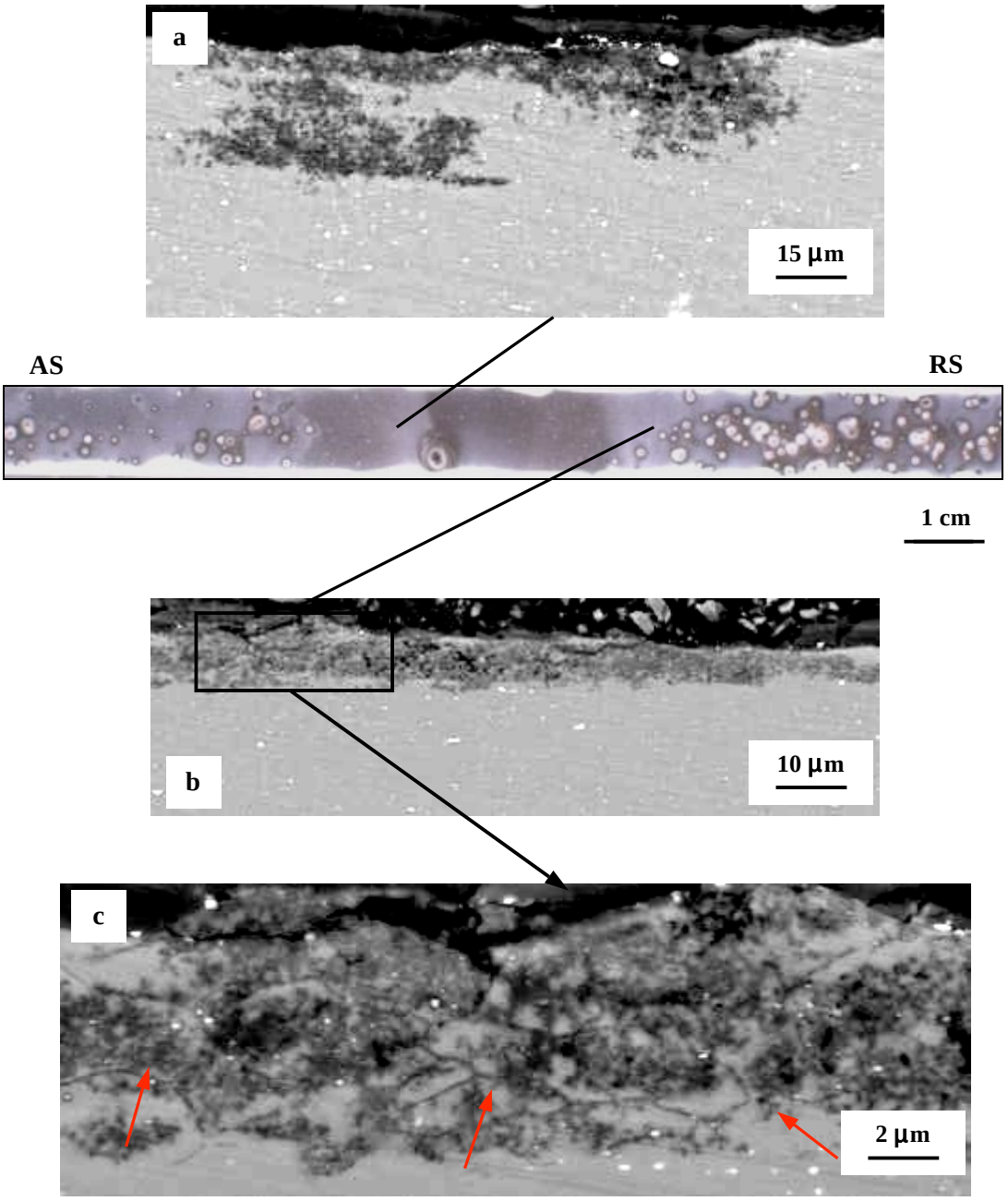

Fig. 4.16 FEG/SEM backscattered electrons images showing the corrosion attack in the TL section of the AA2050-T34 FSW – T8 (18h): (a) HAZ advancing side; (b),(c) HAZ retreating side

Intragranular corrosion was the main form of attack in the HAZ at both sides (Fig. 4.16 a-b). At higher magnification attack at subgrain boundaries was also observed but with less frequency than intragranular attack (Fig. 4.16 c).

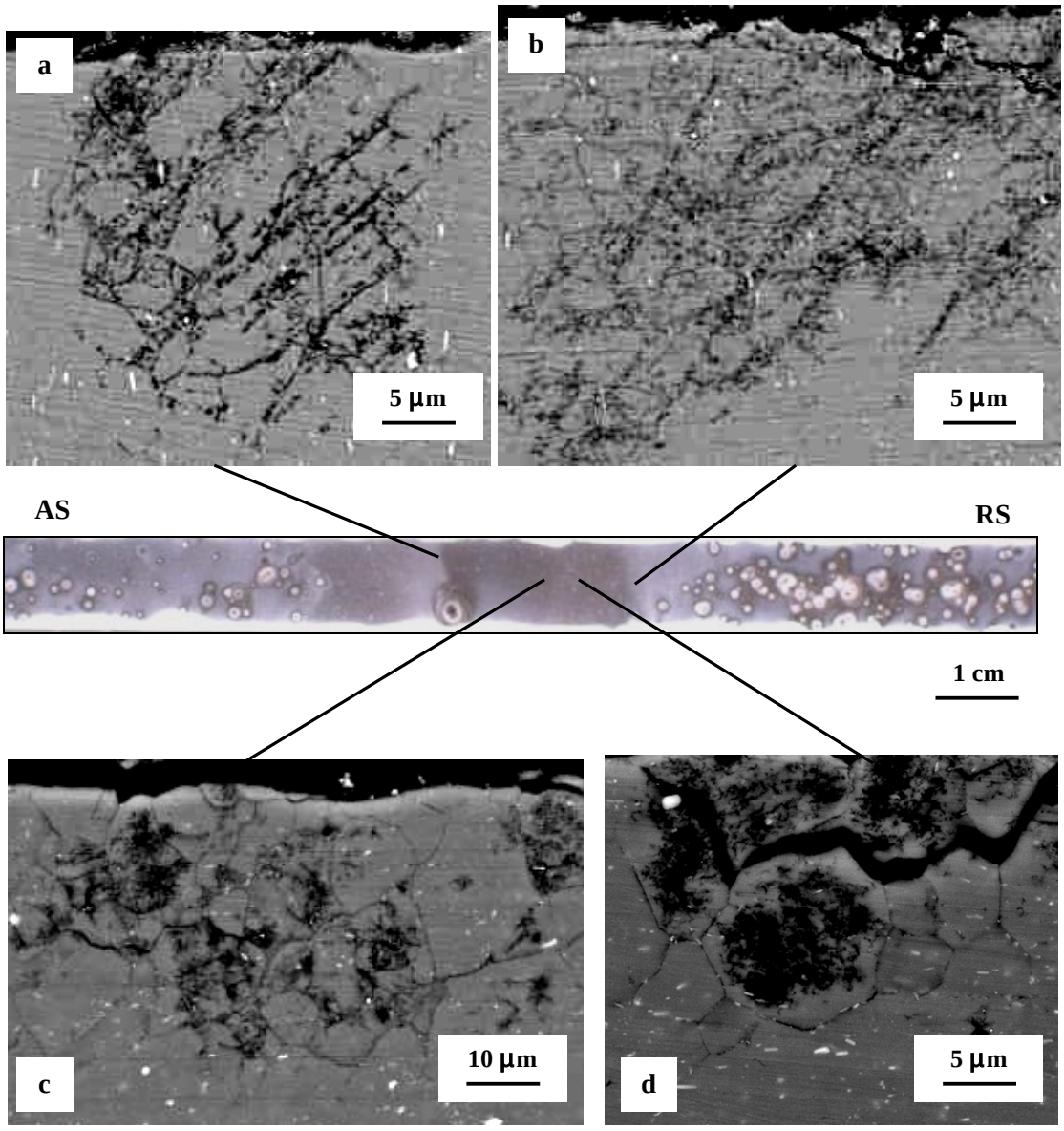

Fig. 4.17 FEG/SEM backscattered electrons images showing the corrosion attack in the TL section of the AA2050-T34 FSW – T8 (18h): (a) TMAZ advancing side; (b) TMAZ retreating side; (c), (d) nugget

In the TMAZ, at both sides (Fig. 4.17 a-b) corrosion attack appears fairly uniform with signs of intragranular attack. Corrosion at subgrain boundaries is also visible. In the nugget some grains show attack only at the boundary, while others grains appear corroded both at boundary and, partially, inside the grain (Fig. 4.17 c-d).

4.4.6. AA2050-T34 FSW – T8 (36h)

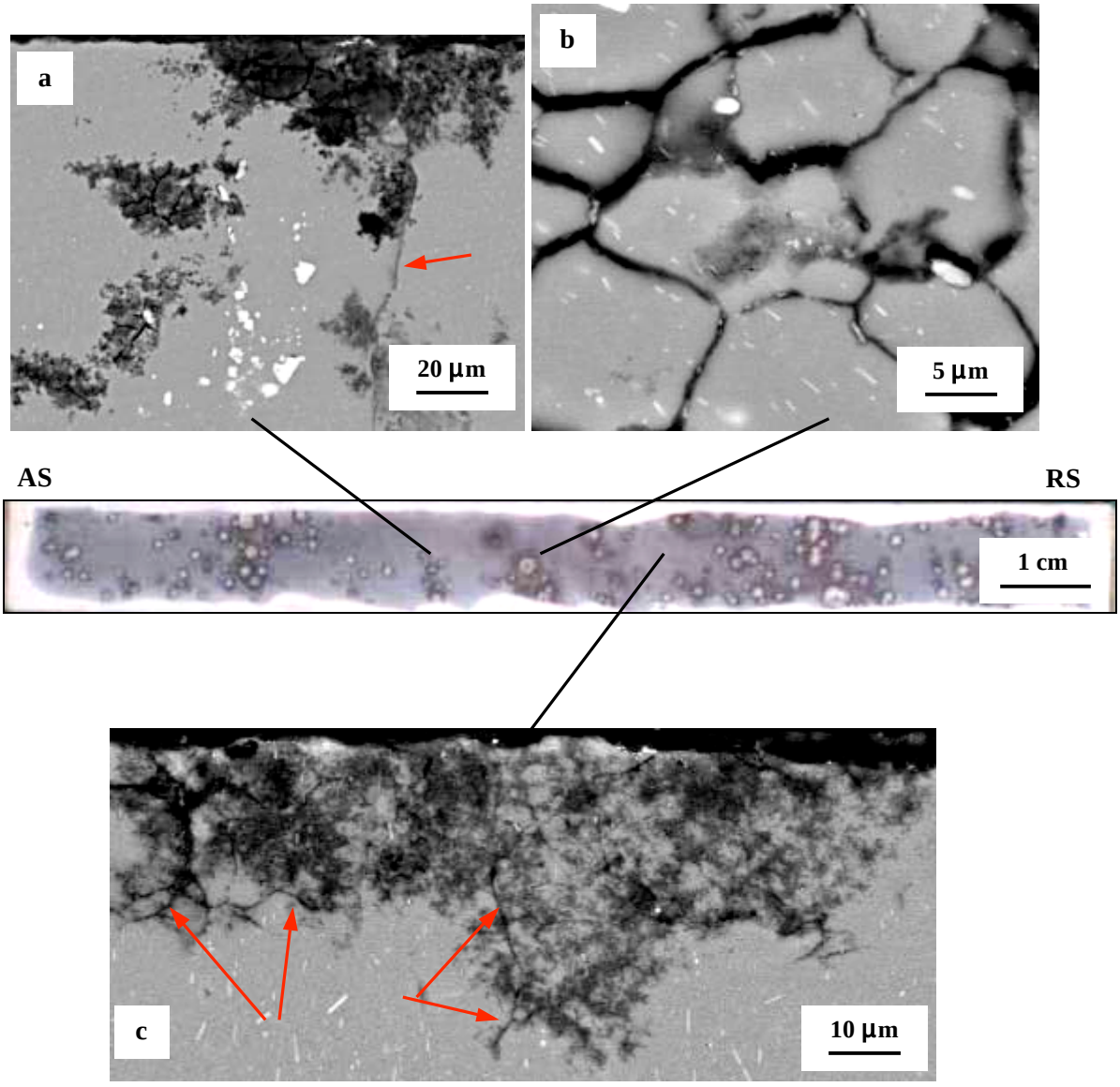

Fig. 4.18 FEG/SEM backscattered electrons images showing the corrosion attack in the TL section of the AA2050-T34 FSW – T8 (36h): (a) HAZ advancing side, (b) nugget; (c) HAZ retreating side. Attack at grain and subgrains highlights with narrows

After ageing for 36 hours, intergranular corrosion is the main form of attack in the nugget. Along some boundaries, the attack becomes severe and in some grains, signs of intragranular corrosion is also visible (Fig. 4.18 b), but less evident than for the 18 h treatment. In the HAZ, at both sides of the weld, the prevalent form of attack is intragranular corrosion (Fig. 4.18 a-c). Attack at grain and subgrains boundaries is also observed (highlights with narrows).

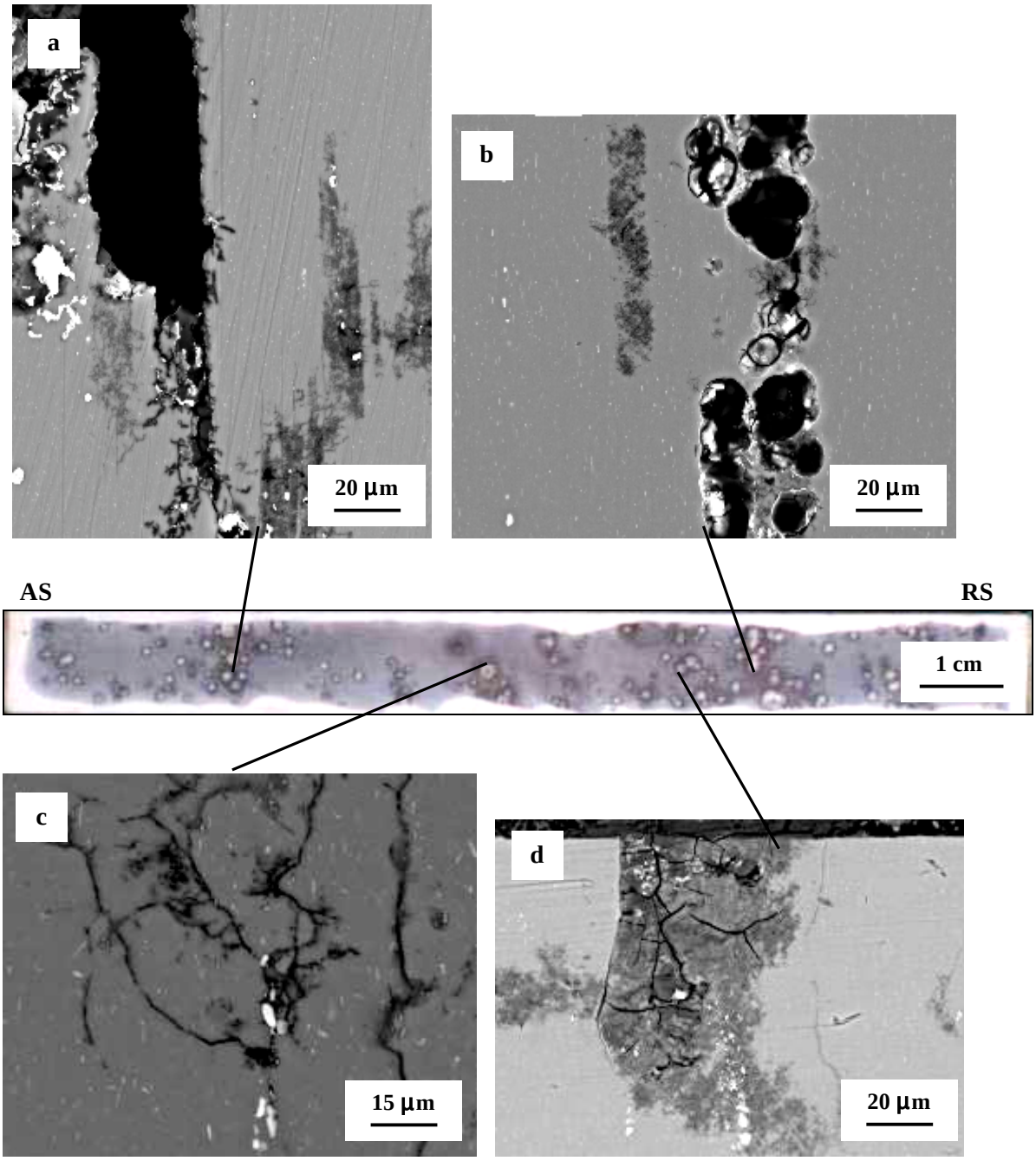

Fig. 4.19 FEG/SEM backscattered electrons images showing the corrosion attack in the TL section of the AA2050-T34 FSW – T8 (36h): (a), (b), (d) base metal; (c) TMAZ advancing side.

The TMAZ was mildly corroded. Attack was found mainly at subgrain boundaries (Fig. 4.19 c). Compared with the two under-aged conditions, the attack in this region was less severe. In the base metal, the attack was mainly intragranular. Some pits grow along the rolling directions (Fig. 4.19 (a) and (b)), as observed in the T8 (18 h) condition. Attack at grain boundaries was also visible in some locations.

4.4.6 AA2050-T34 FSW – T8 (72h)

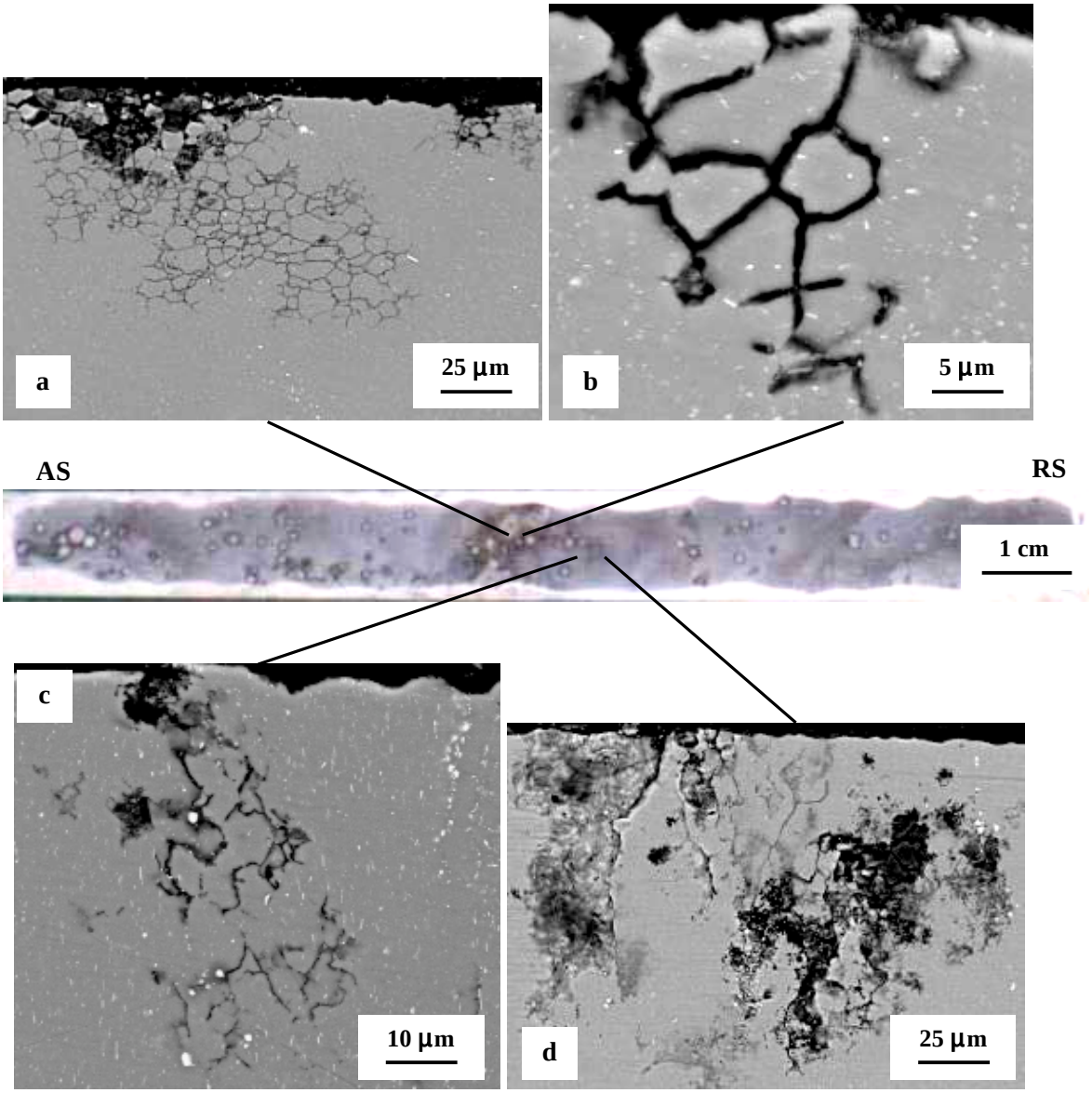

Fig. 4.20 FEG/SEM backscattered electrons images showing the corrosion attack in the TL section of the AA2050-T34 FSW – T8 (72h): (a),(b) nugget; (c) TMAZ retreating side; (d) HAZ retreating side

For the sample aged for 72 hours, several observations of intergranular corrosion were observed in the nugget and, in some case, the attack at grain boundaries appears severe (Fig.4.20 b). Intragranular corrosion was also observed (Fig. 4.20 a). In the TMAZ prevalent attack at subgrain boundaries was found (Fig. 4.20 c). In the HAZ intragranular corrosion is the main form of attack and in some observations intergranular attack is also visible (Fig.4.20 d refers to the retreating side).

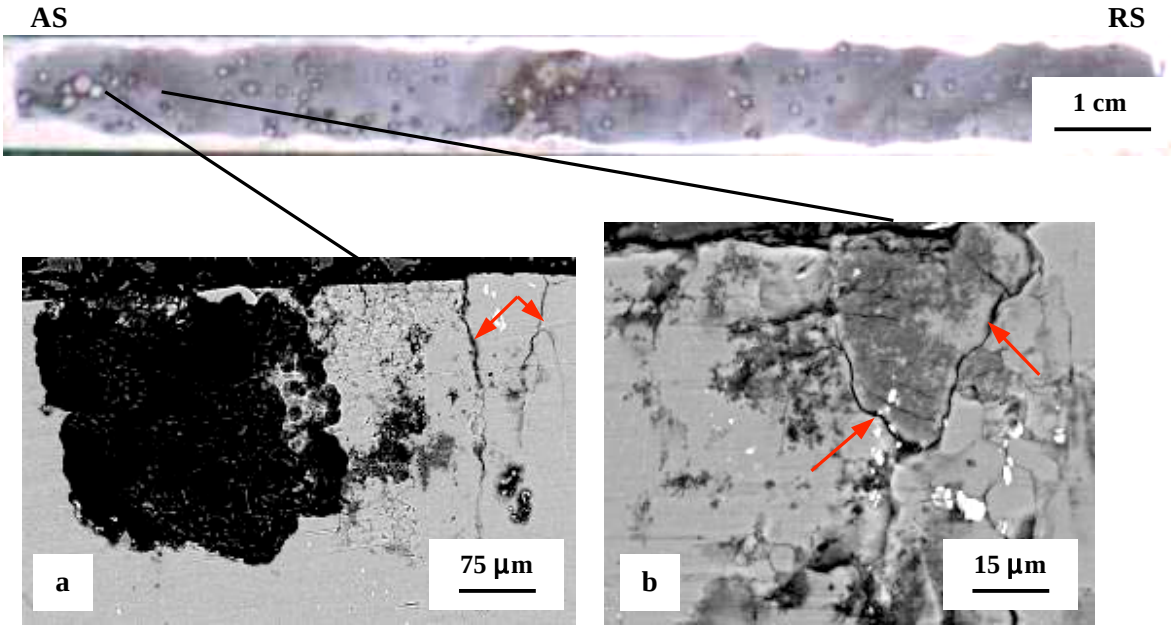

Fig. 4.21 FEG/SEM backscattered electrons images showing the corrosion attack in the TL section of the AA2050-T34 FSW – T8 (72h): (a),(b) base metal. Red arrows highlight attack at grain boundaries in form of cracks

In the base metal several observations of intergranular and intragranular corrosion were found. Intergranular corrosion leads to large cavities (Fig. 4.21 a) and to pits that along the rolling direction Attack at grain boundaries it is severe and in some observation appears in a form of cracks (highlighted in Fig. 4.21 b).

4.7. Intergranular corrosion test (ASTM G110)

An intergranular corrosion test (G110 ASTM [104]) was performed on AA2050-T34 FSW – T8 (18h). A macroscopic image of the transverse cross section of the weld after the test is shown in Fig. 4.22. The result is consistent with the 0.1 M NaCl immersion test (see Fig. 4.7 c and Fig. 4.13): prevalent attack was found in the base material, were the build-up corrosion products are concentrated.

Fig. 4.22 Macrograph of AA2050-T34 FSW - T8 (18h) after immersion test in 0.98 M NaCl – 0.09 M H_2O_2 for 24 h

After the immersion test and following polishing (in order to remove the corrosion products), optical and FEG/SEM images were taken in the different regions of the weld.

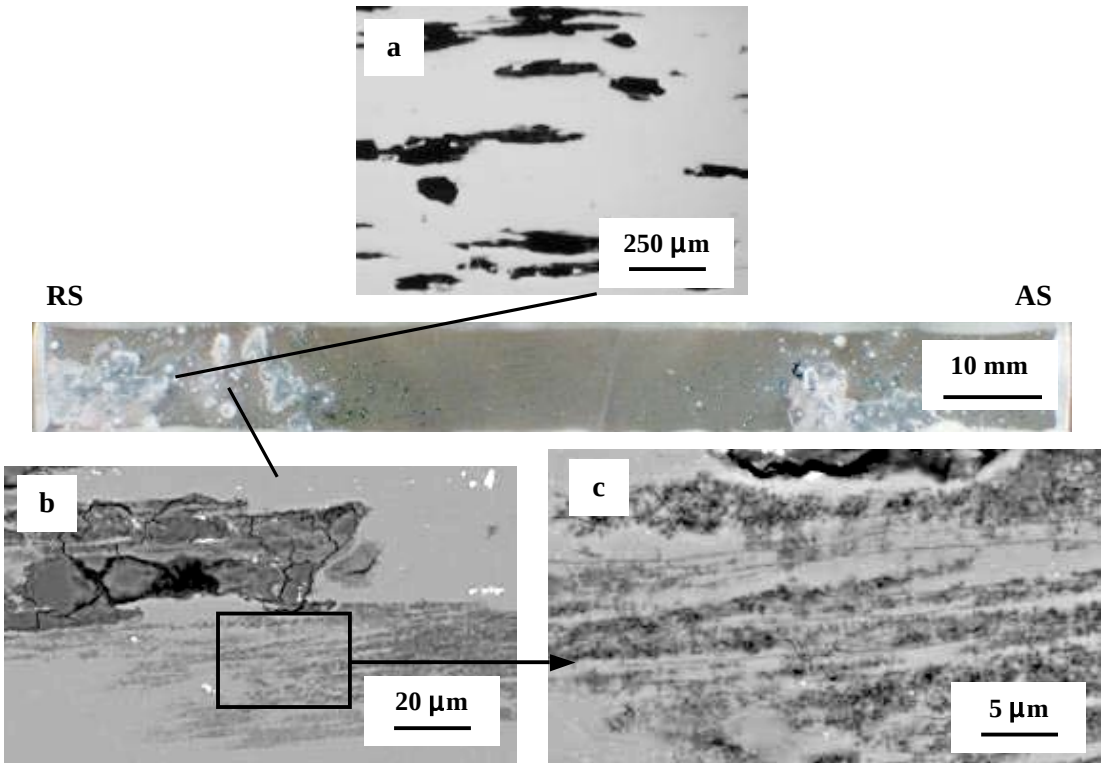

Fig. 4.23 Optical (a) and FEG/SEM backscattered electrons images (b) and (c) images showing the corrosion attack in the base metal. AA2050-T34 FSW – T8 (18h) after G110 test.

In the base metal several, large pits along the grain orientation (Fig. 4.23 a) and intragranular corrosion (Fig. 4.23 b), were found. In some observations attack at grain boundaries is also visible (Fig. 4.23 c).

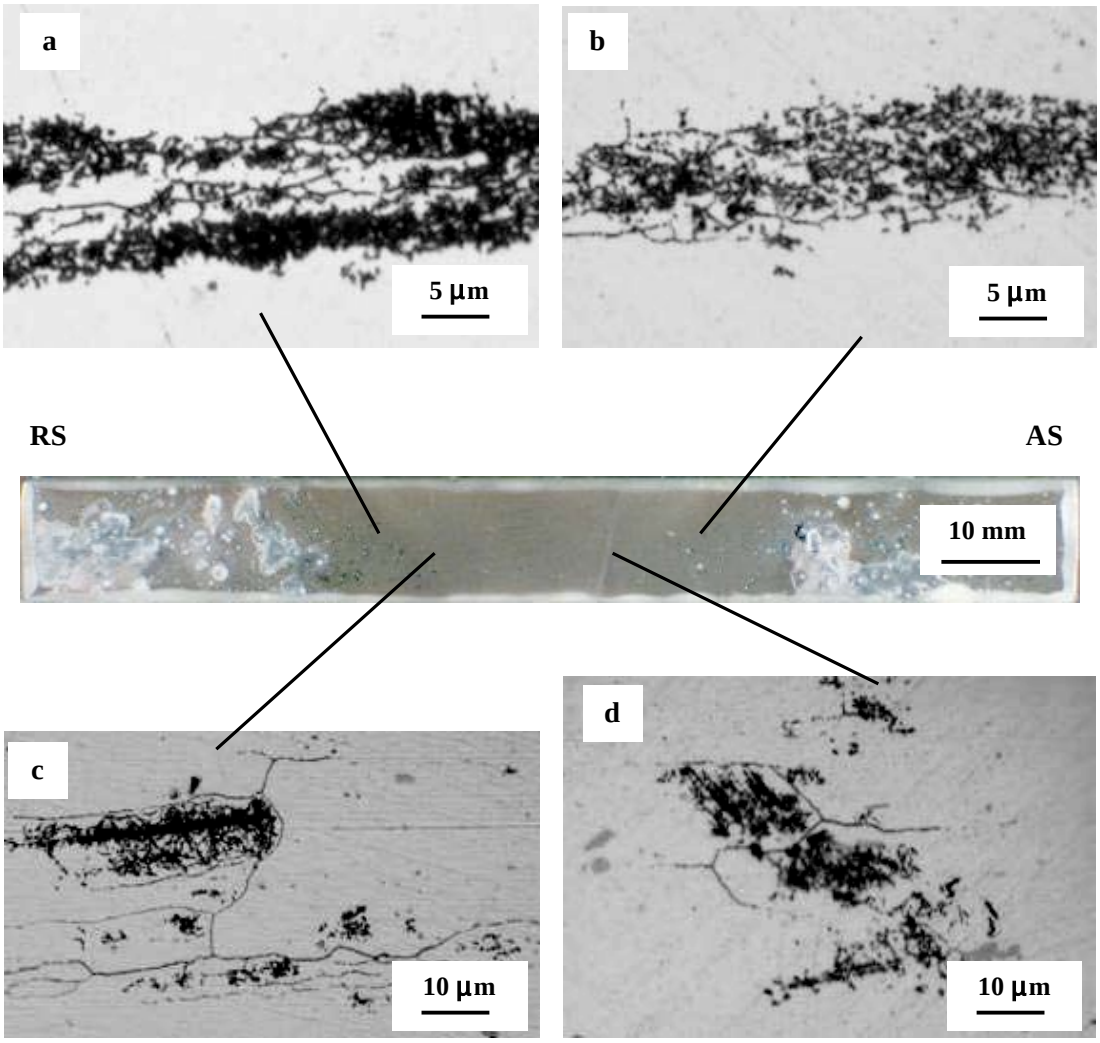

Fig. 4.24 Optical images showing the corrosion attack in retreating side AA2050-T34 FSW – T8 (18h) after G110 test:
(a) HAZ retreating side; (b) HAZ advancing side; (c) TMAZ retreating side; (d) TMAZ.

In the HAZ (Fig. 4.24 a-b) and in TMAZ (Fig. 4.24 c-d) at both sides, intergranular and intergranular corrosion were found. In the HAZ intragranular corrosion is the main form of attack. In the same region, some signs of attack at grain boundaries were found close to the interface with TMAZ while, towards the interface with the base metal, pits, similar to those found in base metal, were also observed (not shown).

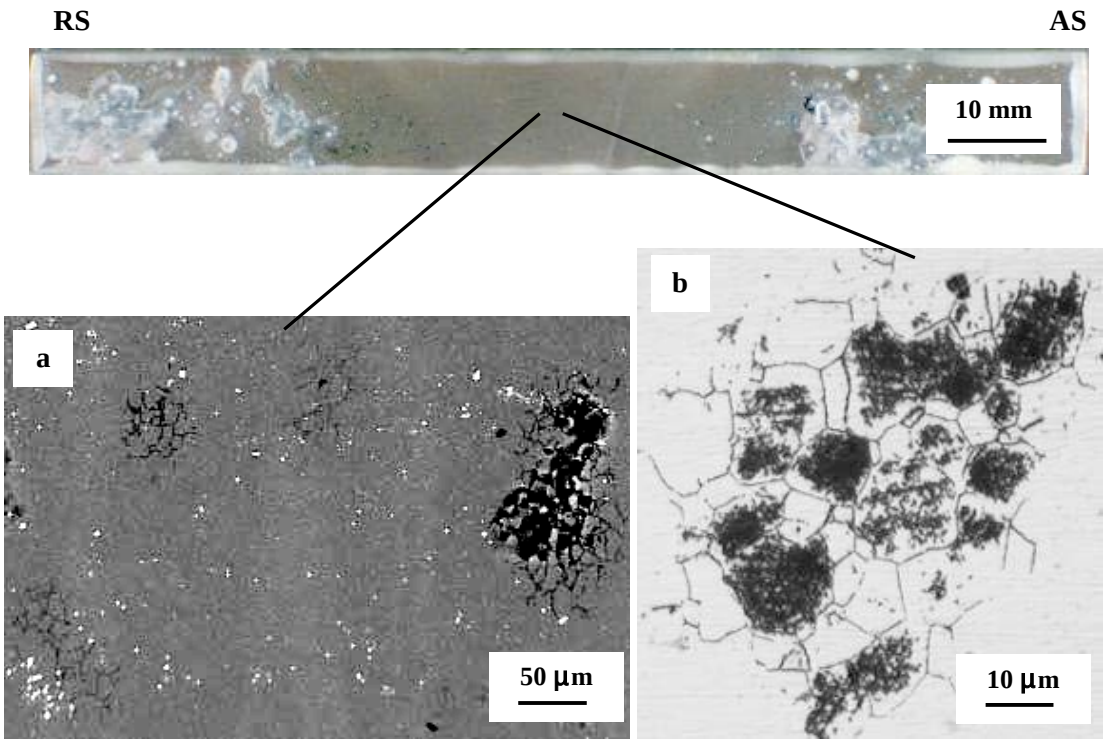

Fig. 4.25 FEG/SEM backscattered electrons image (a) and optical image (b) showing the corrosion attack in the nugget. AA2050-T34 FSW – T8(18h) after G110 test

In the nugget intergranular and intragranular attack were found (Fig. 4.25a). In this region, as already observed for the 0.1 M NaCl immersion test, for some grains the corrosion is essentially intergranular while for others the attack is also inside the grain (Fig 4.25b).

The overall results show that all weld regions are susceptible to intergranular corrosion. Intergranular corrosion was found also in the base metal, while the test in 0.1 M NaCl didn't reveal this kind of attack in this region. Consistently with the 0.1 M NaCl test, the nugget, followed by TMAZ, was the region more susceptible to intergranular corrosion, while in the base metal the attack predominantly took place as intragranular corrosion and in a form of large pits that propagate along the grains orientation. Compared to the 0.1 M NaCl test the attack was found more severe and the number of observation was higher. This should be a consequence of the more aggressive solution of the G110 test compared to the 0.1 M NaCl test.

4.8. Electrochemical behaviour

5.6.1. Long term OCP

Long-term OCP measurements were taken for 24 h in 0.1 M NaCl solution, for the full weld in the five different heat treatment conditions. From the naturally-aged condition T34, to the over-aged condition T8 (72h), a shift of the curves through more negative values (Fig. 4.26) was observed. In the last 2 hours of the test, the two under-aged conditions and the two over-aged conditions reached about the same value, -600 mV and -660 mV respectively, while the T8 (18h) shows an intermediate value (-640 mV) between the two extreme post weld heat treatment conditions. Consistently with the immersions test, after long term OCP measurements, the exposed surface showed corrosion product mainly in the HAZ in the under-aged conditions, predominantly in the base metal in the T8 (18h) and all over the weld in the over-aged conditions.

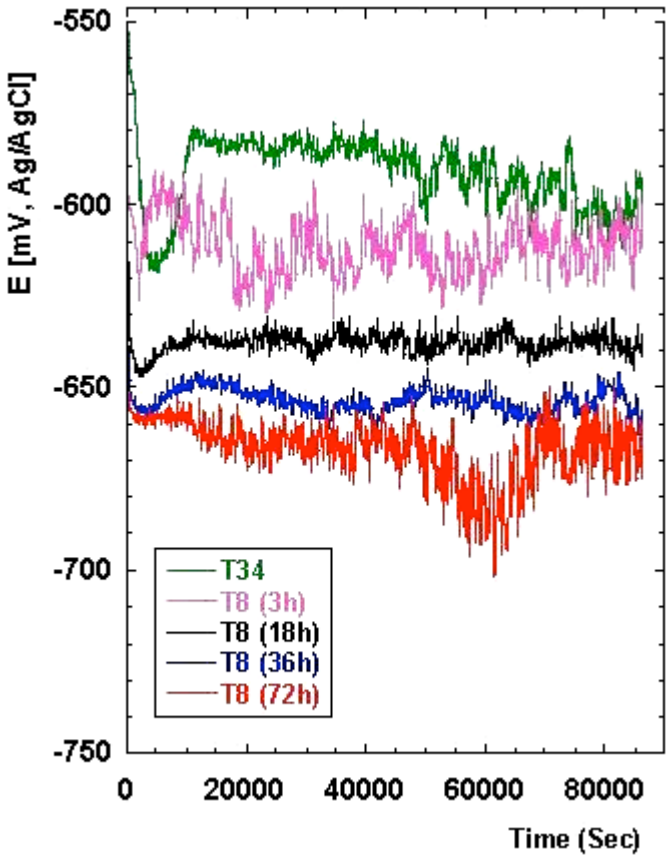

Fig. 4.26 OCP measurements in 0.1 M NaCl for the five different post weld heat treatment conditions

Fig. 4.27 shows for the T8 (18h) condition, long term OCP measurements in the two solutions used for the immersion test: 0.1 M NaCl and G110 solution (0.98 M NaCl + 0.09 M H_2O_2). The more aggressive solution used in the intergranular test leads to a lower value of the OCP.

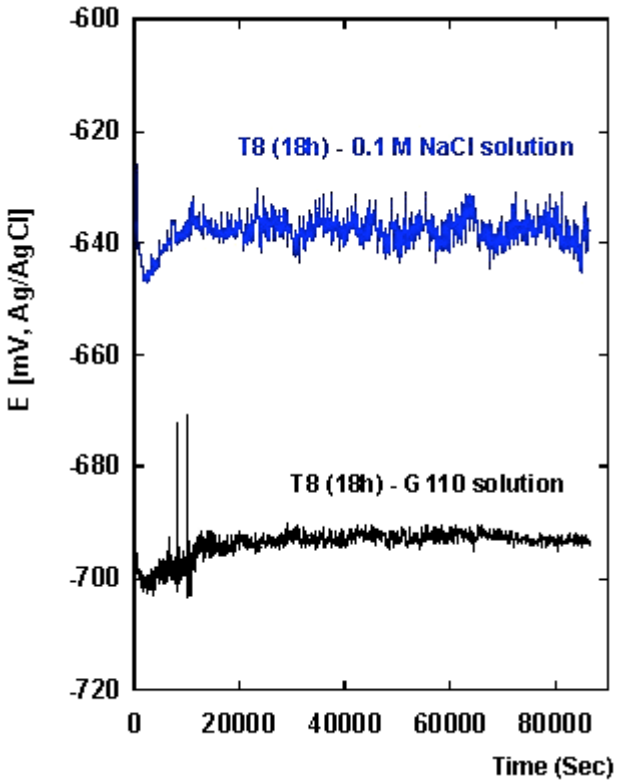

Fig. 4.27 OCP measurements in 0.1 M NaCl an in 0.98 M NaCl + 0.09 M H_2O_2, after 24 h for the five different post weld heat treatment conditions

5.6.2. Potentiodynamic measurements

4.6.2.1. Anodic polarization measurements

Anodic polarization tests were performed, starting from -10 mV from the OCP, in 0.01 M NaCl naturally aerated solution, at a sweep rate of 1 mV/s. For the five different post weld heat treatment conditions measurements were taken in the nugget (Fig. 4.28 a) and in the base metal (Fig. 4.28b).

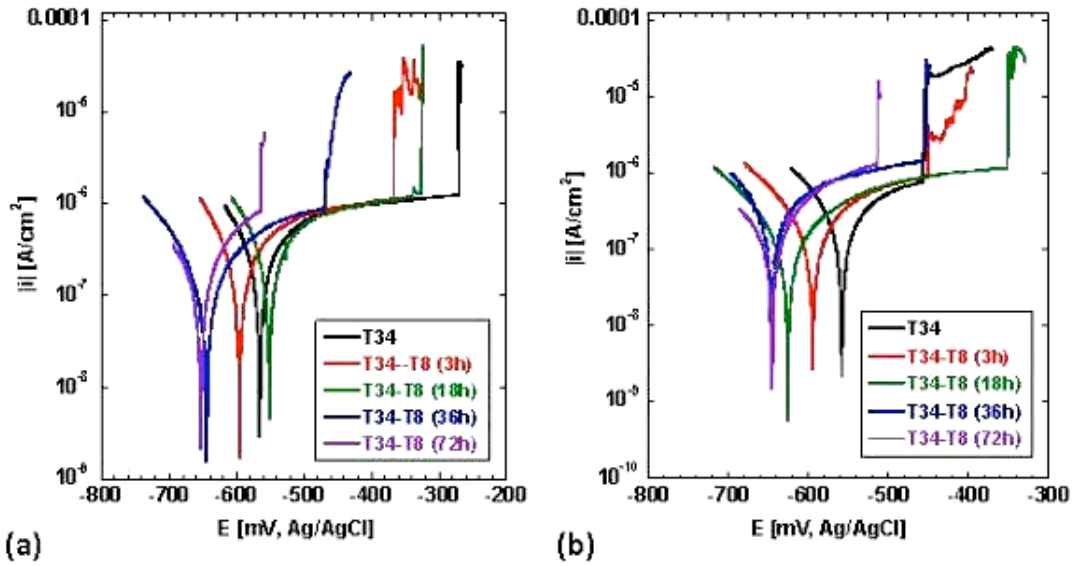

Figure 4.28 Anodic polarization curves for AA2050-T34 FSW in the five different post weld heat treatment conditions (0.01 M NaCl - sweep rate = 1 mV/s). (a) Nugget ; (b) Base Metal

In order to compare the anodic reactivity of the AA2050-T34 FSW, in the different post weld heat treatment conditions, the breakdown potential (Eb) and the open circuit potential (OCP) are presented in Figure 4.29 and Figure 4.30 respectively. In the nugget, over-ageing leads to a decrease of the Eb and the OCP, while the two under-aged and the T8 (18h) conditions show similar values. In the base metal the OCP shows a tendency to move through more negative values increasing the ageing time, while a less evident tendency can be seen for the Eb, even if the T8 (72h) clearly shows the lowest values. In the two over-aged conditions Eb was found lower in the nugget compared to the base metal, while in the two under-aged conditions base metal show the lowest breakdown potential.

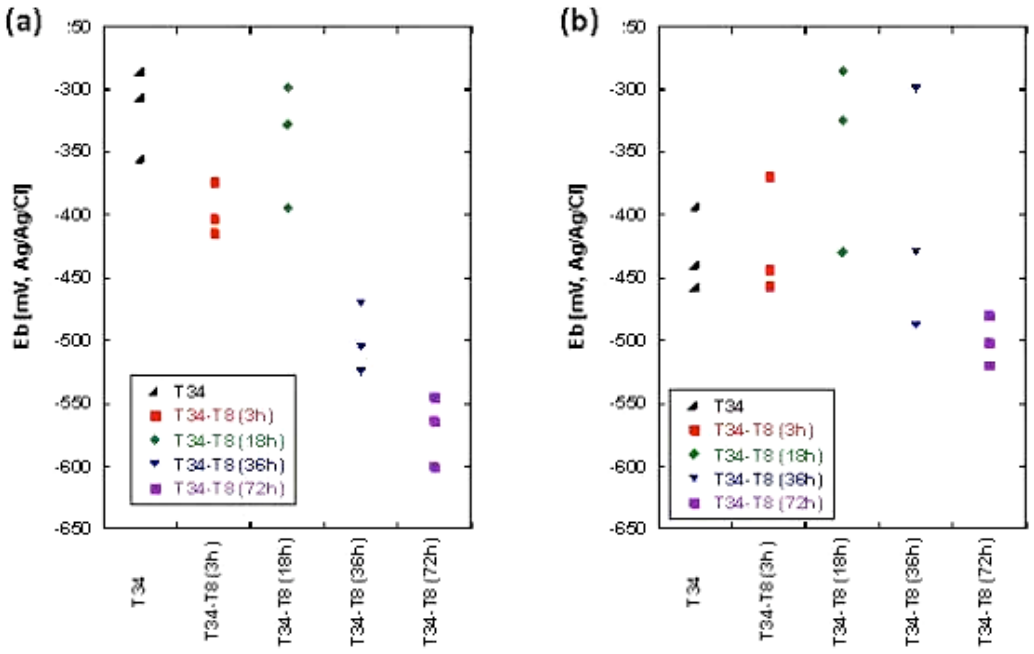

Figure 4.29 Breakdown potential for AA2050-T34 FSW in the five different post weld heat treatment conditions (0.01 M NaCl - sweep rate = 1 mV/s). (a) Nugget, (b) Base Metal (data taken from polarisation curves of the type shown in Figure 4.28)

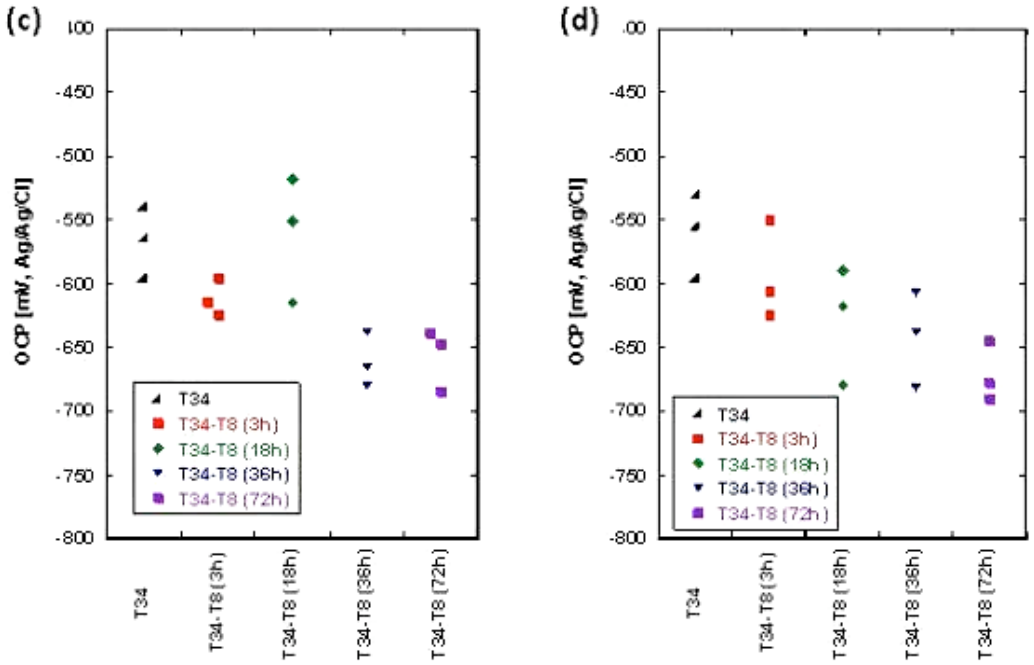

Figure 4.30 Open Circuit Potential for AA2050-T34 FSW in the five different post weld heat treatment conditions (0.01 M NaCl - sweep rate = 1 mV/s). (c) Nugget, (d) Base Metal (data taken from polarisation curves of the type shown in Figure 4.28)

5.6.2.2. Cathodic polarization measurements

Cathodic polarization tests were performed, starting from +10 mV from the OCP, in 0.01 M NaCl naturally aerated solution, at a sweep rate of 1 mV/s. For the five different post weld heat treatment conditions, measurements were taken in the nugget (Fig. 4.31a) and in the base metal (Fig. 4.31b).

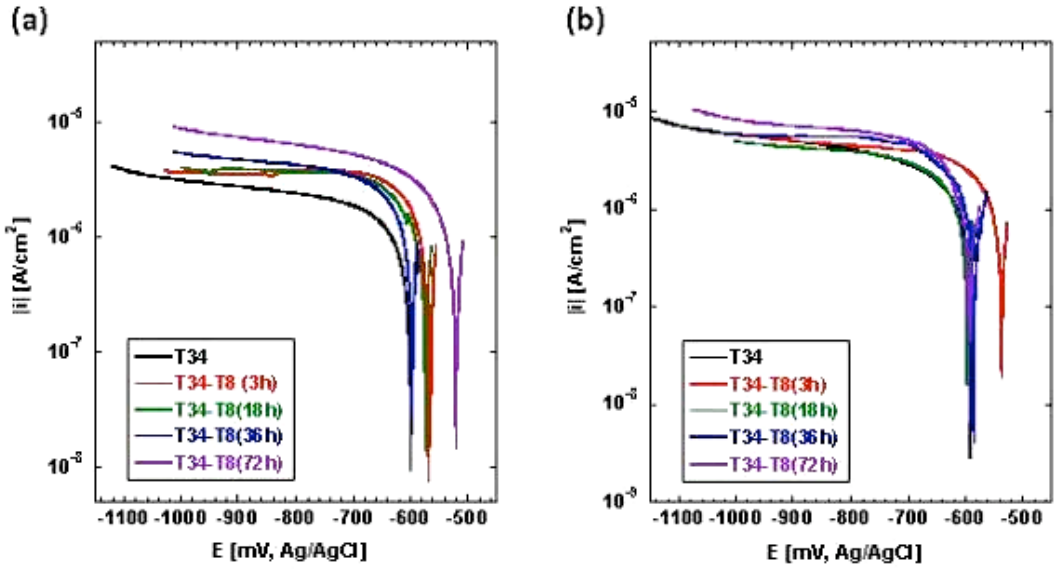

Figure 4.31 Cathodic polarization curves for AA2050-T34 FSW in the five different post weld heat treatment conditions (0.01 M NaCl - sweep rate = 1 mV/s). (a) Nugget ; (b) Base Metal

The cathodic currents were compared at a potential value of -900 mV vs. Ag/AgCl. In the nugget, a tendency to an increase of the cathodic current density with increasing ageing time was observed (Fig. 4.32a). In the base metal, the highest value of the cathodic current was found in the T8 (72h) condition, while no significant difference was observed for the other four conditions (Fig. 4.32b)..

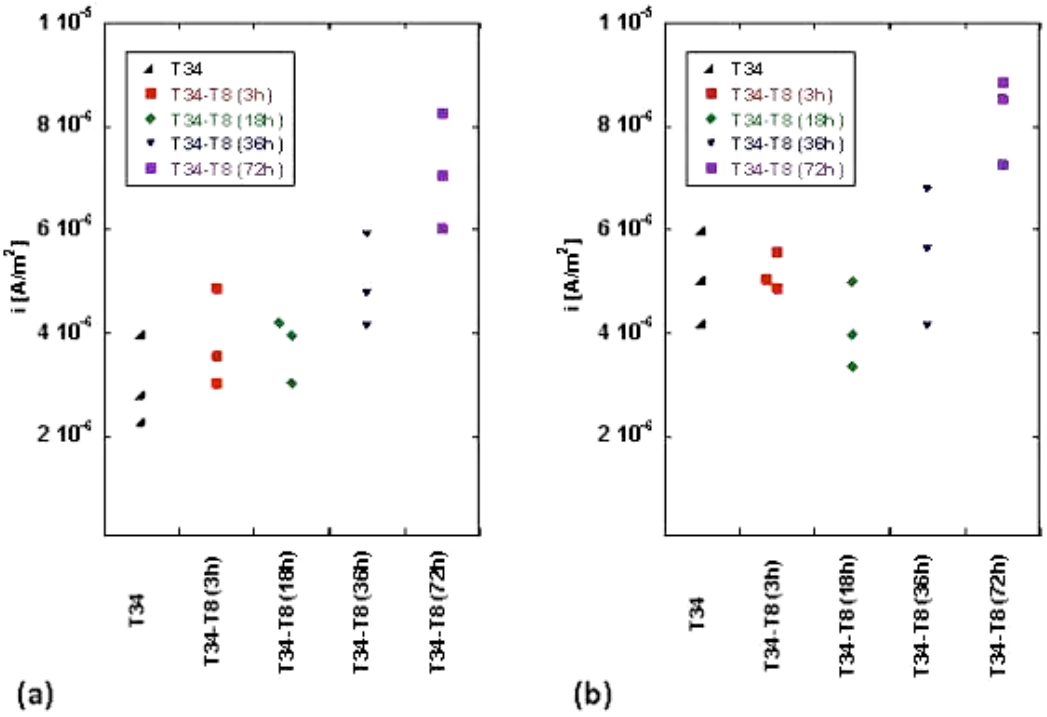

Figure 4.32 Cathodic current densities for AA2050-T34 FSW in the five different post weld heat treatment conditions, at potential equal to -900 mV (0.01 M NaCl - sweep rate = 1 mV/s) (a) Nugget ; (b) Base Metal

5.6.2.3. Anodic polarization measurements along the AA2050-T34 FSW T8 (18h)

For the T8 (18h) conditions anodic measurements were taken along the weld in order to measure local change in electrochemical behaviour in the different regions. From these measurements, the OCP and Eb were determined and plotted in Fig. 4.33. From the nugget to the base metal, at both sides of the weld, a decrease of the OCP is observed (Fig. 4.33a). Eb shows high scattering and no clear trend can be seen (Fig. 4.33b). Pitting was often found associated with copper-containing intermetallic particles (see Section 4.4.1.), that were found with similar size and distribution along the whole weld. If the Eb measured from the polarization curves is associated with these particles, no big difference should be expected in its value in the different regions of the weld.

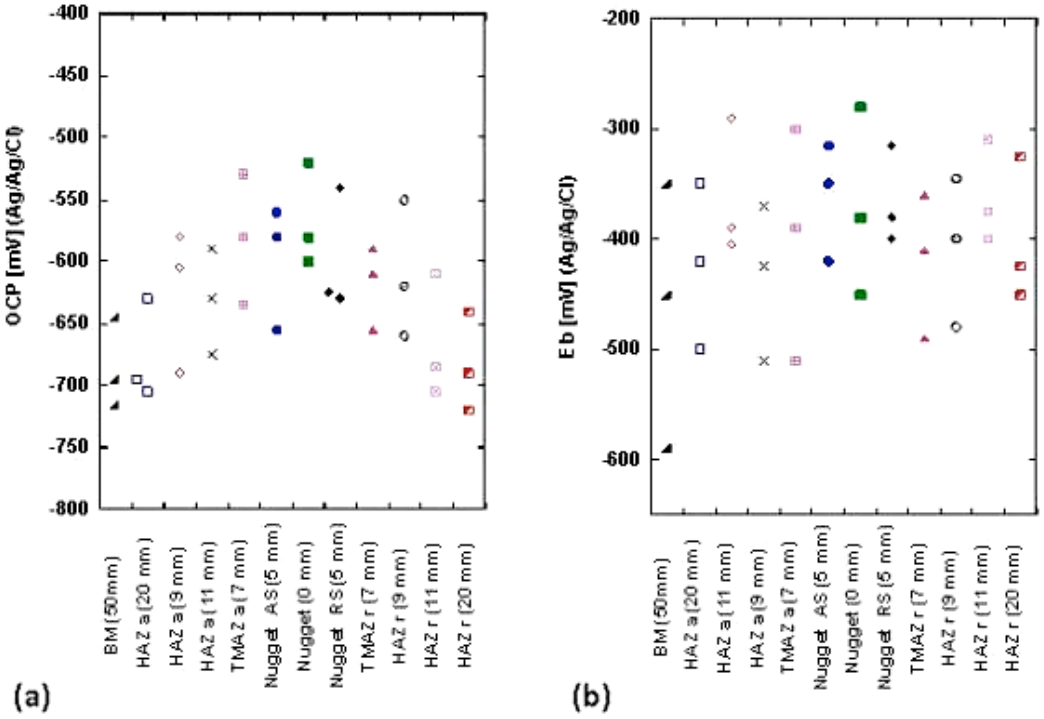

Figure 4.33 AA2050-T34 FSW T8 (18h) polarization measurements along the weld (0.01 M NaCl - sweep rate = 1 mV/s)

(a) OCP ; (b) Eb

CHAPTER 5 Discussion

5.1. Base alloy

The base alloy is the region that is not subjected to the thermal effect of the welding. In the T34 condition, the presence of dislocations, due to stretching, gives possible initiation sites for precipitation during natural ageing. However, very little precipitation took place in the matrix, as confirmed by the low hardness measured and it should be associated with the main phases reported for this temper condition (δ' and GP Zone [42]). The matrix is therefore corrosion resistant because a relatively high level of copper remains in solid solution. There is also evidently very little precipitation at grain boundaries as attack is not visible.

As the base alloy is heat-treated, there is an increase in precipitation. This is initially slow (3h shows little increase in hardness) but then reaches a peak at 18 h, and the precipitates coarsen from 18 h onward, leading to lower hardness at 36 h and 72 h. The lower hardness found in the 36 h and 72 h treatments suggests that over-ageing has taken place in base alloy for these treatment conditions.

Immersion tests in 0.1 M NaCl solution show a progressive change in the corrosion attack in the base alloy. In the T34 condition no signs of attack were found both at grain boundaries and in the matrix. After 3 hours of post weld heat treatment, T1 particles are expected to precipitate both at grain boundaries, where they have strong tendency to nucleate and grow, and to a lesser extent in the matrix, (see TTP diagrams, Fig. 2.5 [42]). This tendency explains the fairly small increase in hardness compared to the T34 weld and the prevalent attack at grain boundaries (and, in a few observations inside the grains) found for this heat treatment condition. The copper level in solid solution in the matrix is expected to remain fairly high, whereas, along the grain boundaries, the copper in solid solution will be lowered, owing to more extensive precipitation at grain boundaries, leading to a difference in solute content that promotes intergranular corrosion.

In the T34-18 h treatment, intragranular corrosion and pits along the rolling direction are the main form of attack. Intergranular corrosion was found after the G110 test but not after the 0.1 M NaCl immersion test. Among the 5 post weld heat treatment conditions, the T34-18 h was found to have the highest in hardness, which indicates the presence of a high density of T1 particles both in the matrix and at grain boundaries, with a corresponding relatively uniform and lower solute copper content, which will give a fairly low driving force for intergranular attack. .

In the two overaged conditions (36 h and 72 h), precipitates coarsen in the matrix, and the hardness decrease compared with the 18 h treatment. Coarsening is expected also for the precipitates that, in the early stage of heat treatment, nucleate and precipitate at grain boundaries. An even lower and more uniform solute level of copper is expected, which would be expected to favour pitting over intergranular attack. Pits along the rolling direction were found but with less frequency then in the 18 h treatment.

A change in the morphology of attack for base alloy from underageing conditions, where attack (when found) was essentially confined to grain boundaries, to overageing conditions where attack is prevalent inside the grain and in form of pitting, can be related with the role of T1 active precipitates and the variation of copper content. The strong role of T1 precipitates in corrosion behaviour of Al-Li alloys has been extensively studied [82,89-92]. In the Al-Cu-Li-X system, T1 was observed being an active phase, more anodic than the base alloy. In chloride-containing solutions attack starts as preferential dissolution of this active phase [82-87]. The effect of this dissolution is the dealloying of lithium from this phase and the consequent change in the electrochemical behaviour from anodic to cathodic of T1 with respect to the surrounding base alloy. The effect of T1 precipitation is also the decrease in copper content in the surrounding base alloy as mentioned above.

In the underaged condition, attack is essentially confined at grain boundaries, where T1 has strong tendency to precipitate [42] to give copper-depletion in the matrix along the grain boundaries, while in the matrix, lack of precipitation determines the absence of T1 active phase, from where corrosion can begin, and, at the same time, leaves all copper in solid solution. As heat treatment proceeds,

precipitation brings the amount of copper in the matrix down and the precipitate density (or size in overaged conditions) increases.

The cathodic reactivity increases with ageing time. Previous work on AA2024 [51] has shown that copper-rich precipitates (Al_2CuMg in the case of AA2024) are good sites for the cathodic reaction. It is likely that T1 will show similar behaviour, so this suggests that more precipitation takes place with increasing ageing time.

Anodic polarisation curves suggest that there is a higher passive current density for overageing for 36 and 72 h. This may be a result of copper depletion. This may also explain the small decrease in OCP (Fig. 4.28) since an increase in anodic reactivity will tend to decrease the OCP even in the presence of a small increase in cathodic reactivity.

The OCP of the base alloy decreases with increasing ageing time. This tendency was found for both polarisation curves in 0.01M NaCl (Fig.4.30 d) and long term OCP (Fig. 4.26) measurements in 0.1 M NaCl. This is the opposite effect that might be expected given the increase in cathodic reactivity. It suggests that the anodic effect dominates the OCP.

The long term OCP is noisy, suggesting that localised attack is occurring, which is consistent with visual observations of cross sections (although these are at a rather longer exposure time).

5.2. HAZ

Microstructural transformations that occur in the HAZ region are related to the temperature transient due to the welding process. These temperatures are reported in the range of 250-350°C [49, 56]. The microstructure of the alloy, before welding processes, must also be considered. In this case, FSW was carried out a few weeks after, following the SHT and the stretching, therefore, during this time, some precipitation should be expected.

In the T34 post weld heat treatment condition it was observed that corrosion attack is localized in the heat affected zone. At the interface with the TMAZ, in the region closer to the weld, the effect of the temperature transient is more important therefore corrosion was found with the observation of severe and intragranular, intergranular and pitting attack

.

Depending on the temperature history in this region, different microstructural changes can be expected: exposure in the range of 250–300 °C can lead to some T1 precipitation. In this temperature range, T1 phase is reported to be the predominant phase [42]. Precipitation starts first at subgrain boundaries and then in the matrix. In the same temperature range, precipitates that are present in the stretched alloy before welding undergo coarsening. If T1 precipitates are present in the base alloy before welding, as in the case of a 2150-T8 FSW [45], the heat generated during welding process leads to coarsening of this strengthening phase at subgrain boundaries and to the formation of PFZs.

At higher temperatures (up to 350 °C), rapid precipitation of θ' (Al_2Cu), is reported to take place first at subgrain boundaries and then in the matrix for the AA2195-T8 [42]. This situation is less probable than the previous case because these higher temperatures are generally reported for faster welding process [48]. It was also observed for a Al-1.8Li-2.70Cu-0.6Mg-0.3Zn (after interrupted quenching from solutionizing temperatures), that in chloride contain solution intergranular and inter-subgranular attack took place when T1 precipitate is present at boundaries. For the same alloy, on the contrary, no corrosion was found in the case of presence of θ' precipitates [82].

In the outer edge of the HAZ, at the interface with the base alloy, the effects of the temperature transient during welding are less evident, and attack is essentially confined to grain boundaries. At this location in the HAZ, temperatures around 250°C can be expected [49, 56]. Exposure to this temperature, even for a short time (6 minutes [42]) lead to abundant nucleation and significant coarsening of T1, particularly at subgrain boundaries, were they should be expected longer and thicker than in the matrix [42].

On increasing the ageing time, the corrosion attack in the HAZ is less severe. After 3 h of heat treatment, the attack is still predominantly in the heat-affected region but less severe than in the T34 condition and mainly concentrated inside the grains. In the 18 h, 36 h and 72 h conditions intragranular attack is the main form of corrosion. Subgrain boundary attack is also visible (Fig. 4.16 c and Fig 4.18 c).

5.3. TMAZ

During the welding process, the TMAZ is subjected to high temperatures and high plastic deformation. Higher temperatures in TMAZ compared with the HAZ leads to a lower hardness owing to the dissolution of strengthening precipitates, but mechanical damage can be expected to improve the dislocation density and the precipitation process. This second effect is likely to be dominant since in all of the post-weld heat treatment conditions the hardness in TMAZ was found to be higher than in the HAZ. In the 18 h heat treatment, this phenomenon is evident since the two maxima in hardness at the edge of the weld are significantly higher then the values measured in the HAZ and in the nugget. For the other post weld heat treatment conditions, the hardness in TMAZ is close or just slightly higher than in the nugget.

In the T34 condition, corrosion in TMAZ is observed as intragranular attack (Fig. 4.8 d) and subgrain boundary attack (Fig. 4.8 e). The high temperatures that this region is subjected to during welding, are reported to be in the range of 350-450 °C [49, 56]. At this range of temperatures θ' (Al_2Cu) is reported to precipitate both at grain boundaries and in the matrix [42].

After a 3 h heat treatment, the corrosion attack in the TMAZ is less severe than in the T34 condition. Fig. 4.12 b-c, refers to the interface Nugget/TMAZ. At this location (corresponding at the microstructure indicated in Fig. 4.5 a-b) both recrystallised grains, typical of the nugget region, are visible and the effect of plastic deformation is already visible. Around the equiaxed recrystallised structure, intergranular corrosion takes place. Because the nugget is still characterized by low hardness in the matrix, it is likely that no important precipitation has taken place there. In contrast, the effect of the high plastic deformation characterising the TMAZ

interface should promote some precipitation in the matrix and this, as previously observed, lead to a more favourable situation for attack inside the grains.

Improving the ageing time the attack in TMAZ become less and less important. In the 18 h heat treatment the attack is fairly uniform. Attack at subgrain boundaries is also visible (Fig. 4.17 a-b). Attack at grain and subgrain boundaries is visible also after G110 immersion test (Fig. 4.24 c-d) but in some case attack is visible also inside the grain. In the two overageing condition, 36 h and 72 h heat treatment, TMAZ appear mildly corroded and attack is essentially at subgrain boundaries (Fig. 4.19 c and Fig. 4.20 c respectively).

5.4. Nugget

The nugget is the region that has been subjected to a high temperature, in the range of 450 - 540 °C [56] and high plastic deformation. The resulting dynamic recrystallisation produces the fine equiaxed grains observed in Fig. 4.2 a-b-c. An increase in hardness after post welding heat treatment is observed, suggesting that in this region the temperature reaches a value that corresponds to partial or complete solution heat treatment. In this situation a high level of copper is expected in solid solution, improving the corrosion resistance of the matrix. A low dislocation density makes precipitation more difficult, except at grain boundaries.

In the T34 condition, the nugget appears to be corrosion resistant. Signs of corrosion were only found around the constituent particles which act as cathodically-active sites (Fig. 4.10 b). A very few precipitates, mainly at grain boundaries, and high copper content in solid solution are expected. The high breakdown potential (Fig. 4.29 a) and the low passive current density (Fig. 4.32 a), indicate that this region is probably a net cathode when coupled to the rest of material.

After 3 h heat treatment no significant change in hardness is observed compared with the T34 condition and the nugget was generally found to be corrosion resistant. A few signs of intergranular attack suggest that some precipitation has started taking place at grain boundaries.

After 18 h, the significant increase in hardness observed indicates the onset of matrix precipitation. Since grain boundaries act as preferential sites for nucleation, precipitates should be expected to grow there. After immersion in 0.1 M NaCl and, consistently, after the G110 test, corrosion attack is found both in the interior and at the boundaries of grains. Around grain boundaries, a region with no attack was often observed (Fig. 4.17 c – d and Fig. 4.25 b). It is possible that grain boundary precipitation has led to vacancy depletion around grain boundaries making precipitation more difficult there. Therefore this region around grain remains precipitate free and retains higher copper content than the centre of the grains, where precipitation leads to intragranular attack.

After 36 h no significant change in hardness is observed compared with the 18 h treatment, therefore no further precipitation in the matrix should be expected. The corrosion attack is predominantly at grain boundaries (Fig. 4.18 b) where it appears to more deep than the 18 h heat treatment. The breakdown potential is significant lower and an increase in cathodic current is also observed.

A similar situation, compared with the 36 h, was found for the 72 h, but the attack at grain boundaries tends to spread in larger areas (Fig. 4.20 a). In addition, a further reduction in the breakdown potential was observed.

5.5. Synopsis

Hardness varies along the weld, according to the different microstructure determined by the thermo-mechanical process. Results are consistent with the literature that reports a correlation with hardness, microstructure and precipitation sequence. A correlation with precipitation and corrosion morphology is also reported.

Results show that over ageing mainly lead to:

- A decrease in hardness in the base alloy.
- An increase in cathodic reactivity in the base alloy, related with the higher precipitates density and size and a simultaneous decrease in OCP values in the base alloy (which suggest that anodic effect dominates OCP).
- An increase in corrosion attack at grain boundaries in the nugget.
- Susceptibility to pitting, intragranular and intergranular corrosion in the base alloy. Attack at grain boundaries is particularly severe, in form of deep fissures, caused by the dissolution process, which could have a deleterious effect on SCC resistance.

For these reasons prolonged ageing treatment should be avoided.

In the T34 natural aged condition a good corrosion resistance is shown in the region were low precipitations is expected but in the heat affected region, due to FSW, the corrosion is severe. In the same time the overall hardness remains the lowest among the five post welding temper conditions analysed. Low corrosion resistance in the HAZ associated with an overall low hardness make this temper conditions not appropriate for the AA2050-FSW.

Main differences between 3 h and 18 h are:

- 18 h temper has higher hardness, up to 50 HV in the base alloy compared to the 3 h temper
- A difference in hardness, up to 50 HV, showed along the weld in the 18 h temper, while in the 3 h temper hardness profile results more “flat”

(therefore more homogeneous mechanical proprieties along the weld should be expected)

- In the nugget intergranular corrosion susceptibility is higher in the 18 h temper than in the 3 h temper (where just a beginning of attack was found)
- In 3 h temper the base metal is mildly attacked while the 18 h an increase in corrosion susceptibility is observed. For the 18 h temper pitting, intragranular and intergranular (after G110 test) were found in base alloy. In the 18 h temper pits, found deep in the bulk along the rolling directions, could act as stress risers and have an adverse effect on the fatigue and SCC, if stresses are applied along this direction

CHAPTER 6 Conclusions

The corrosion resistance of a AA2050-T34 FSW was investigated in the naturally-aged condition and following four different post weld heat treatment conditions: aged for 3 h, 18 h, 36 h and 72 h at 155 °C. In all cases, some corrosion was observed following exposure to chloride-containing solutions. However, the location, mode and extent of corrosion showed significant variation for the different heat treatments.

The heat resulting from welding itself and post-weld heat treatments leads to the precipitation of copper-rich T1 precipitates first at subgrain boundaries and then in the matrix. Subgrain boundary precipitation leads to copper-depletion at the boundary, with consequent intergranular attack, while precipitation in the matrix can lead to intragranular corrosion (attack of the grains themselves) and pitting as this lowers the copper content in the matrix.

In general, overageing tends to lead to a decrease in breakdown potential, an increase in passive current density prior to breakdown, and an increase in the cathodic reactivity (which is probably associated with an increase in the number of copper-rich precipitates). However, the open circuit potential tends to decrease with overageing, suggesting that the increase in anodic reactivity dominates over the increase in cathodic reactivity.

Overall results show that the higher corrosion resistance characterizes 3 h temper but, in the same time, the low hardness observed could not meet the minimum required for some applications.

Higher hardness in the base alloy is reached for the 18 h temper. For this condition, in the weld region, the HAZ and TMAZ show relatively superficial attack that is mainly in the form of intragranular corrosion with some attack on subgrain boundaries, and relatively little intergranular attack. In the nugget attack was prevalently at grain boundaries. These observations were made for both immersion in 0.1 M NaCl and the more aggressive ASTM-G110 test. Furthermore, the breakdown

potential for both the nugget and base material was one of the highest, whereas the cathodic reactivity was relatively low in both the nugget and base alloy. The OCP of the nugget was found to be slightly higher than that of the base alloy, suggesting that if the two are coupled, the nugget might be a net cathode, further protecting the weld region from corrosion. The main disadvantage of this temper is susceptibility to pitting in the base alloy, although these pits run parallel to the rolling direction and are therefore not a major risk for the development of initiation sites for mechanical failure

Evidence found in literature suggests that corrosion in Al-Cu-Li-X system starts at subgrain boundaries were T1 precipitates have strong tendency to nucleate and growth. In order to reduce corrosion susceptibility avoiding precipitation at subgrain boundaries, without sacrificing hardness a two-step temper is suggested. This ageing treatment, proposed for the AA2195 alloy by Chen and Stanton [43]. consist in a permanence of 20 h at 132 °C, followed by 40 h at 138 °C. Following this treatment an high precipitate density can be achieved in the matrix with no signs of precipitates at subgrain boundaries.

CHAPTER 7 - Appendix

7.4 Appendix A – Temper designation system [110]

T3, Solution Heat Treated, Cold Worked, and Naturally Aged to a Substantially Stable Condition.

T3 applies to products that are cold worked specifically to improve strength after solution heat treatment and for which mechanical properties have been stabilized by room-temperature ageing. It also applies to products in which the effects of cold work, imparted by flattening or straightening, are accounted for in specified property limits.

T4, Solution Heat Treated and Naturally Aged to a Substantially Stable Condition.

This signifies products that are not cold worked after solution heat treatment and for which mechanical properties have been stabilized by room-temperature ageing. If the products are flattened or straightened, the effects of the cold work imparted by flattening or straightening are not accounted for in specified property limits.

T6, Solution Heat Treated and Artificially Aged.

This group encompasses products that are not cold worked after solution heat treatment and for which mechanical properties or dimensional stability, or both, have been substantially improved by precipitation heat treatment. If the products are flattened or straightened, the effects of the cold work imparted by flattening or straightening are not accounted for in specified property limits.

T8, Solution Heat Treated, Cold Worked, and Artificially Aged.

This designation applies to products that are cold worked specifically to improve strength after solution heat treatment and for which mechanical properties or dimensional stability, or both, have been substantially improved by precipitation heat treatment. The effects of cold work, including any cold work imparted by flattening or straightening, are accounted for in specified property limits.

7.5 Appendix B – List of precipitates in Al-Cu-Li alloys

Symbol	Stoichiometry	Remarks
δ	AlLi	Equilibrium phase, nucleates heterogeneously, mainly at grain boundaries
δ'	Al_3Li	Metastable and coherent phase with low misfit. Main strengthening phase in binary Al-Li alloys and in Al-Cu-Li alloys naturally aged.
θ	Al_2Cu	Incoherent equilibrium phase
θ'	Al_2Cu	Semi-coherent plate shapes nucleated at dislocation
θ"	Al_2Cu	Coherent phase. May nucleate at GP zones
T_1	Al_2LiCu	Forms as thin plates on the {111} planes
T_2	Al_5Li_2Cu Al_6Li_3Cu	Equilibrium phase, precipitated preferentially at grain boundaries after prolonged ageing time and high temperatures.
T_B	$Al_{7.5}LiCu_4$	Equilibrium phase, precipitated in the matrix and grain boundaries after prolonged ageing time and high temperatures.
β	Al_3Zr	Dispersoid

7.6 APPENDIX C – Potentiostatic polarization test

In order to find the polarization condition to generate IGC in the different regions of the weld, the T34 and the T8 (72h) conditions were selected and current vs time measurements were made at constant potential (determined below the breakdown potential measured in section 4.6.2.1. for these post weld heat treatments) in acidified (pH 2.75) 0.01 M NaCl naturally-aerated solution. Measurements were taken at -650 mV, value below the lower breakdown potential determined for the T8 (72h), for both under-aged and over-aged conditions (Fig. 6.1). Following the measurements, the corrosion morphology in the different regions was analysed. For the under-aged condition, this constant potential value is lower than the OCP reported in Section 4.6.2.1., the measured currents density were about 30 times lower than in the over-aged and, following the test, no sign of attack was observed. Further measurements at -550 mV, value below the lower breakdown potential determined for the T34, were therefore taken (Fig. 6.2).

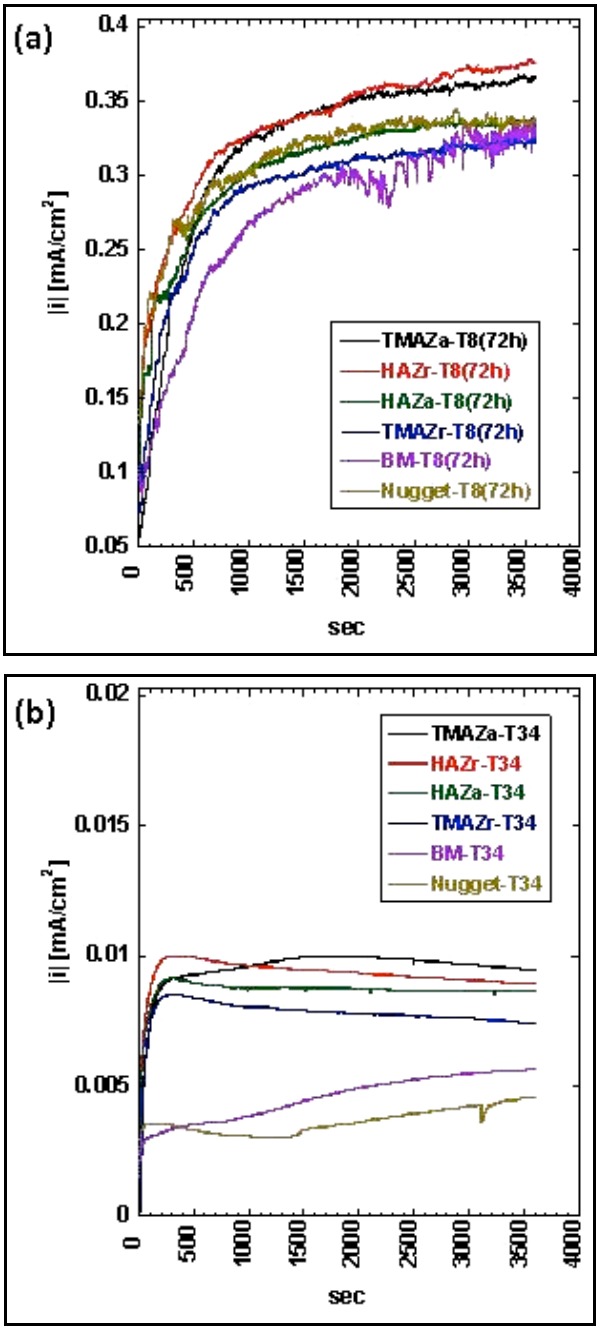

Figure 6.1 Potentiostatic measurements at -650 mV in 0.01 M NaCl acidified at pH 2.75 with HCl. (a) T8 (72h); (b) T34

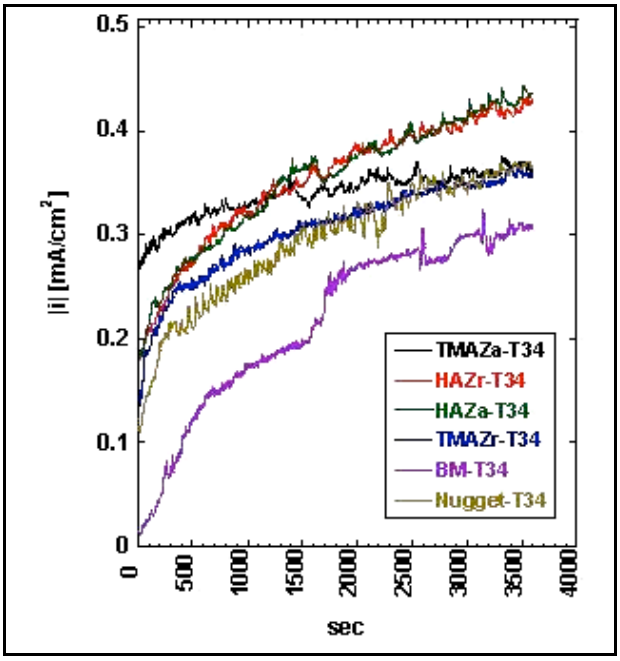

Figure 6.2 Potentiostatic measurements at -550 mV in 0.01 M NaCl acidified at pH 2.75 with HCl for the AA2050-T34 FSW

Fig. 6.3 and 6.4 showed the corrosion morphology following potentiostatic measurements for the over-aged condition, Fig. 6.5 and 6.6 for the under-aged condition. All regions, for both conditions show attack at grain boundaries and, for this reason, through this test, rank the susceptibility of intergranular attack is not possible. Nevertheless from the natural ageing condition to the T8 (72 h) condition an increase in the corrosion attack is visible in all regions. In the weld regions, in the natural condition the attack is essentially confined at grain boundaries, while, after 72 h temper, the attack become present both as intergranular and intragranular corrosion

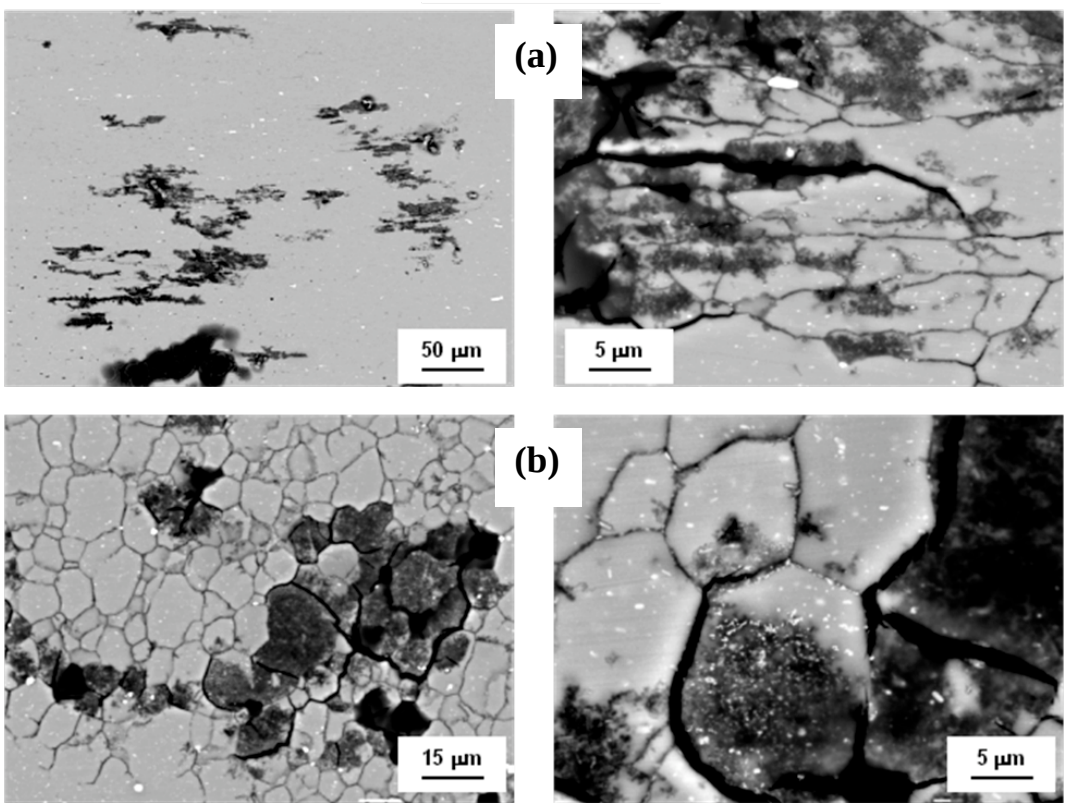

Figure 6.3 Backscattered FEG/SEM images of the top surface of AA2050-T34 FSW T8 (72h) after potentiostatic polarization for 1h at -650 mV (Ag/AgCl) mV in 0.01 M NaCl acidified at pH 2.75 with HCl. (a) Base metal; (b) Nugget

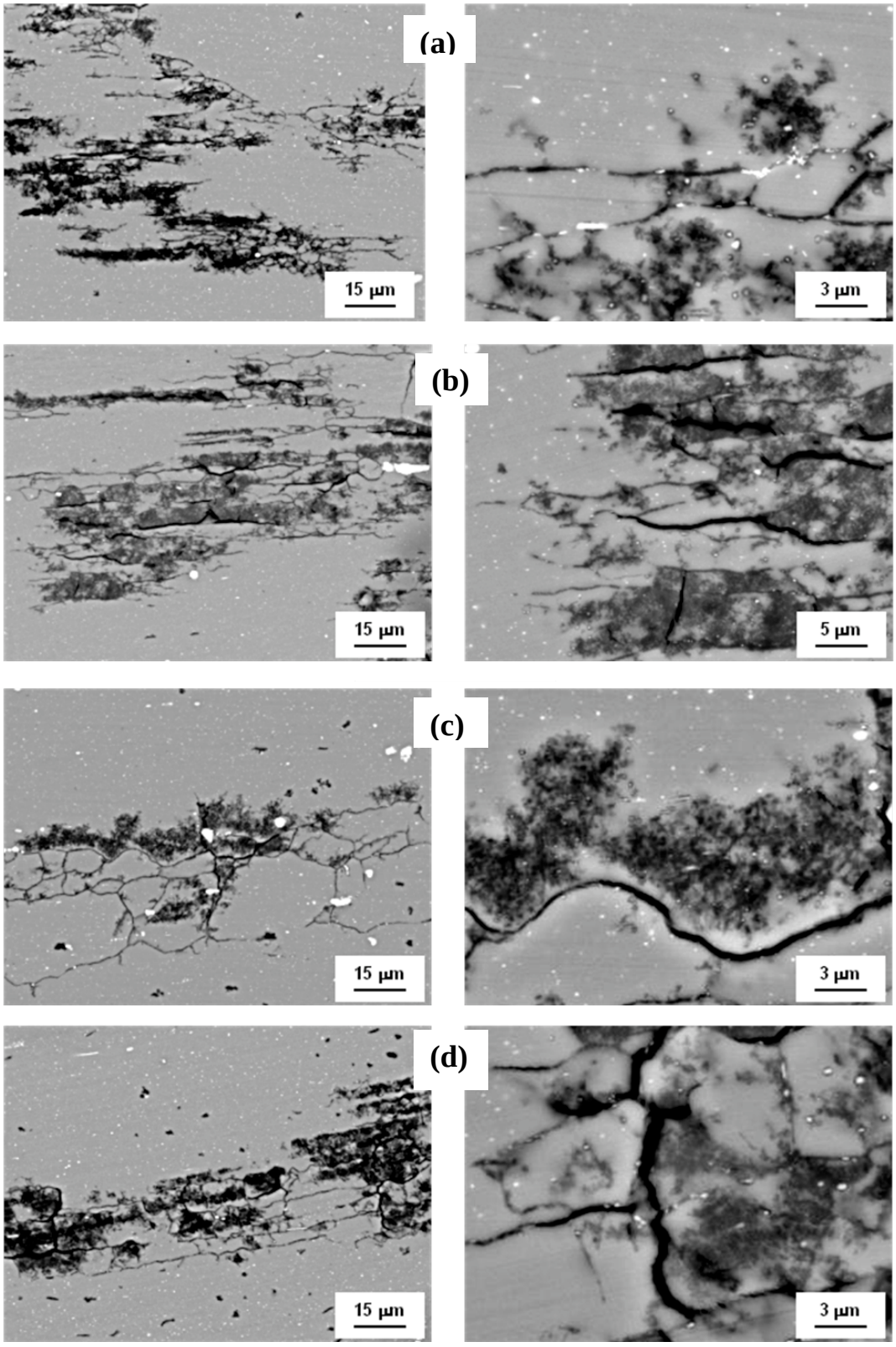

Figure 6.4 Backscattered FEG/SEM images of the top surface of AA2050-T34 FSW T8 (72h) after potentiostatic polarization for 1h at -650 mV (Ag/AgCl) mV in 0.01 M NaCl acidified at pH 2.75 with HCl. (a) HAZ advancing side; (b) HAZ retreating side; (c) TMAZ advancing side; (d) TMAZ retreating side

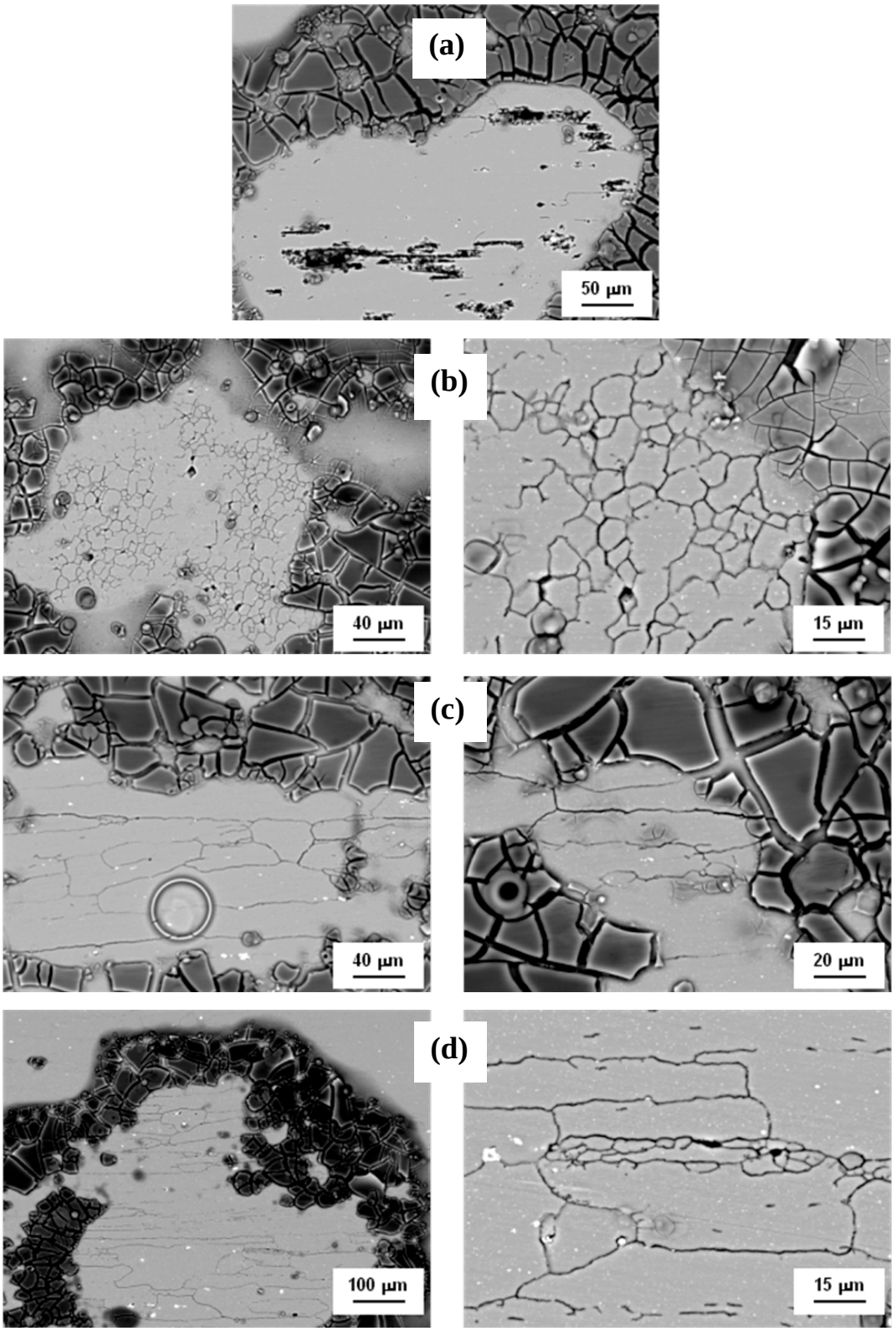

Figure 6.5 Backscattered FEG/SEM images of the top surface of AA2050-T34 FSW after potentiostatic polarization for 1h at -650 mV (Ag/AgCl) mV in 0.01 M NaCl acidified at pH 2.75 with HCl. (a) Base metal; (b) nugget;
(c) HAZ advancing side; (d) HAZ retreating side

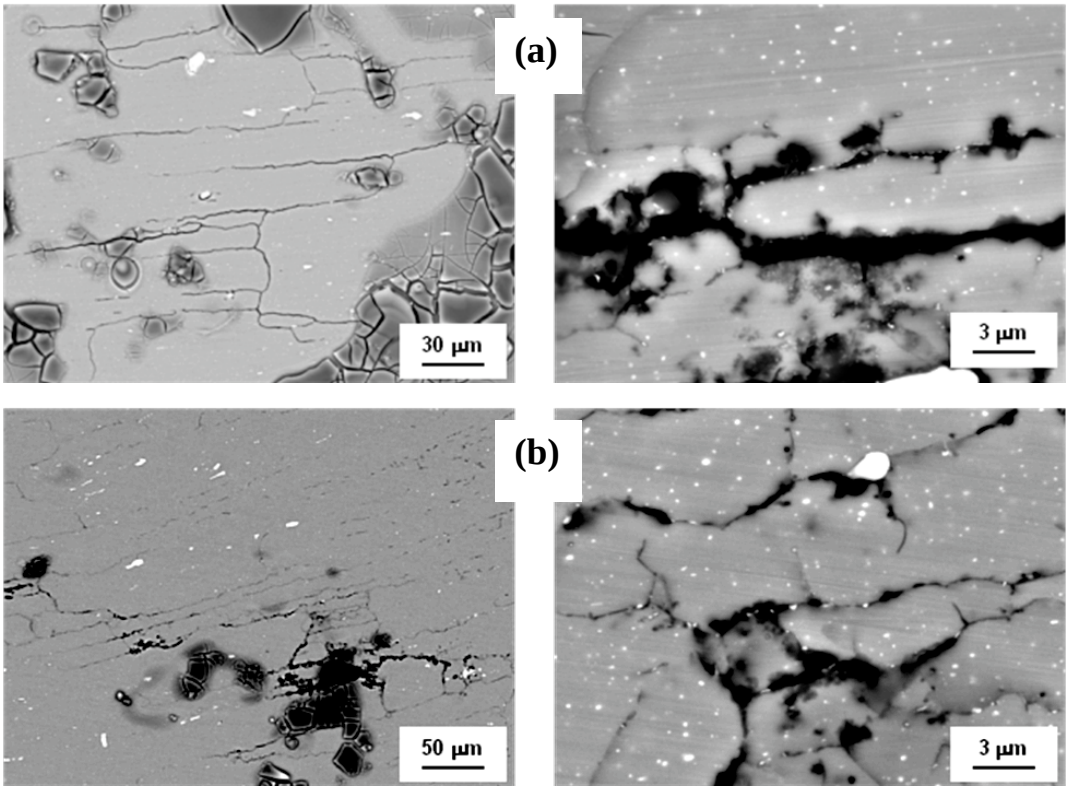

Figure 6.6 Backscattered FEG/SEM images of the top surface of AA2050-T34 FSW) after potentiostatic polarization for 1h at -650 mV (Ag/AgCl) mV in 0.01 M NaCl acidified at pH 2.75 with HCl. (a) TMAZ advancing side; (b) TMAZ retreating side

CHAPTER 8 - References

1. Polmear, I.J., *Wrought aluminium alloys*, in *Light Alloys (Fourth Edition)*. 2005, Butterworth-Heinemann: Oxford. p. 97-204.
2. Nasa - *Super Lightweight External Tank* - NASA Facts - April 2005 - Pub 8-40341. **www.nasa.gov**
3. Starke Jr. , E.A. and J.T. Staley, *Application of modern aluminum alloys to aircraft.* Progress in Aerospace Sciences, 1996. **32**(2-3): p. 131-172.
4. *www.world-aluminium.org*.
5. Campbell, F.C., *Manufacturing Technology for Aerospace Structural Materials*. 2006: Elsevier.
6. Dorward, R.C. and T.R. Pritchett, *Advanced aluminium alloys for aircraft and aerospace applications.* Materials & Design, 1988. **9**(2): p. 63-69.
7. Wanhill, R.J.H., *Status and prospects for aluminium-lithium alloys in aircraft structures.* International Journal of Fatigue, 1994. **16**(1): p. 3-20.
8. Bickley, F.S., Robert J. , *NASA Experience with the Shuttle External Tank* - **www.nasa.gov**
9. Knuwer, M., et al. (2006) *2198-Advanced Aluminum-Lithium alloy for A350 Skin Sheet Application*. **AIRBUS Publication - May 2006**
10. Silcock, J.M., *The structural ageing characteristics of aluminum-copper-lithium alloys.* Journal of Institute of Metals, 1959. **88**.
11. Cassada, W.A., G.J. Shiflet, and W.A. Jesser, *Heterogeneous nucleation and growth of [delta]' in Al--- at.% Li.* Acta Metallurgica et Materialia, 1992. **40**(9): p. 2101-2111.
12. Sanders Jr. , T.H. and E.A. Starke Jr. , *The effect of slip distribution on the monotonic and cyclic ductility of Al---Li binary alloys.* Acta Metallurgica, 1982. **30**(5): p. 927-939.
13. Venables, D., L. Christodoulou, and J.R. Pickens, *On the δ' --> δ transformation in Al-Li alloys.* Scripta Metallurgica, 1983. **17**(10): p. 1263-1268.
14. Christodoulou, L., L. Sruble, and J.R. Pickens, *Stress-Corrosion cracking in Al-Li binary alloys*, in *Aluminium-Lithium Alloys II*, J. E. A. Starke and J. T. H. Sanders, Editors. 1983: Monterey, California. p. 561-579.
15. Vasudevan, A.K., et al., *Fracture behavior in Al-Li alloys: role of grain boundary [delta]*. Materials Science and Engineering, 1985. **72**(2): p. 25-30.
16. Sanders Jr. , T.H., E.A. Ludwiczak, and R.R. Sawtell, *The fracture behavior of recrystallized Al-2.8% Li-0.3% Mn sheet.* Materials Science and Engineering, 1980. **43**(3): p. 247-260.
17. Jha, S.C., T.H. Sanders Jr, and M.A. Dayananda, *Grain boundary precipitate free zones in Al-Li alloys.* Acta Metallurgica, 1987. **35**(2): p. 473-482.
18. Gu, B.P., et al., *Coarsening of δ' precipitates in an Al-2.8Li0.3Mn alloy*. Materials Science and Engineering, 1985. **70**: p. 217-228.
19. Mahalingam, K., et al., *Coarsening of δ' precipitates in binary Al-Li alloys.* Acta Metallurgica, 1987. **35**(2): p. 483-498.
20. Starke Jr., E.A. and T.H. Sanders Jr., *Overview of the physical metallurgy in the Al-Li-X system*, in *Aluminium-Lithium Alloys II*, J. E. A. Starke and J. T. H. Sanders, Editors. 1983: Monterey, California. p. 1-15.

21. Starke Jr. , E.A. and W.E. Quist, *The Microstructure and Properties of Aluminum-Lithium Alloys*, in *New Light Alloys, AGARD Lecture Series No. 174*. 1990: Neuilly Sur Seine, France. p. 1-23.
22. Gregson, P.J. and H.M. Flower, *Microstructural control of toughness in aluminium-lithium alloys.* Acta Metallurgica, 1985. **33**(3): p. 527-537.
23. Gregson, P.J. and H.M. Flower, Journal Matererial Science Letters, 194. **3**: p. 829-834.
24. Polmear, I.J. and R.J. Chester, *Abnormal age hardening in an Al-Cu-Mg alloy containing silver and lithium.* Scripta Metallurgica, 1989. **23**(7): p. 1213-1217.
25. Pickens, J.R., et al. in *Aluminum-Lithium Alloys V*. 1989. Birmingham.
26. Tack, W.T., F.H. Heubaum, and J.R. Pickens, *Mechanical property evaluations of a new, ultra-high strength Al-Cu-Li-Ag-Mg alloy*. Scripta Metallurgica et Materialia, 1990. **24**(9): p. 1685-1690.
27. Kumar, K.S. and F.H. Heubaum, *The effect of Li content on the natural ageing response of Al-Cu-Li-Mg-Ag-Zr alloys.* Acta Materialia, 1997. **45**(6): p. 2317-2327.
28. Wang, Z.M. and R.N. Shenoy, *Microstructural Characterization of Aluminum-Lithium Alloys 1460 and 2195* 1988, Langley Research Center p. 44.
29. Gayle, F.W., et al., *Composition and anisotropy in Al-Cu-Li-Ag-Mg-Zr alloys.* Scripta Metallurgica et Materialia, 1994. **30**(6): p. 761-766.
30. Huang, B.-P. and Z.-Q. Zheng, *Effects of Li Content on Precipitation in Al-Cu-(Li)-Mg-Ag-Zr Alloys.* Scripta Materialia, 1998. **38**(3): p. 357-362.
31. Association, T.A., *International Alloy designation and chemical composition limits for wrought aluminum and wrought aluminum alloys*. 2006: Washington.
32. Ryum, N., *Precipitation and recrystallization in an A1-0.5 WT.% Zr-alloy.* Acta Metallurgica, 1969. **17**(3): p. 269-278.
33. Sanders Jr., R.E. and E.A. Starke Jr., *The effect of grain refinement on the low cycle fatigue behavior of an Al-Zn-Mg-Zr alloy*. Materials Science and Engineering, 1977. **28**(1): p. 53-68.
34. Wu, L.-M., et al., *Effects of homogenization treatment on recrystallization behavior and dispersoid distribution in an Al-Zn-Mg-Sc-Zr alloy*. Journal of Alloys and Compounds, 2008. **456**(1-2): p. 163-169.
35. Gu, B.P., et al., *The influence of zirconium on the coarsening of δ' (Al3Li) in an Al-2.8 wt.% Li-0.14 wt.% Zr alloy*. Materials Science and Engineering, 1985. **76**: p. 147-157.
36. Muddle, B.C. and I.J. Polmear, *The precipitate Ω phase in Al-Cu-Mg-Ag alloys.* Acta Metallurgica, 1989. **37**(3): p. 777-789.
37. Huang, B.P. and Z.Q. Zheng, *Independent and combined roles of trace Mg and Ag additions in properties precipitation process and precipitation kinetics of Al-Cu-Li-(Mg)-(Ag)-Zr-Ti alloys.* Acta Materialia, 1998. **46**(12): p. 4381-4393.
38. Cassada, W.A., G.J. Shiflet, and E.A. Starke Jr. , *The effect of plastic deformation on Al_2CuLi (T1) precipitation.* Metallurgical Transaction A, 1991. **22A**: p. 299-306.
39. Gayle, F.W., F.H. Heubaum, and J.R. Pickens, *Structure and properties during ageing of an ultra-high strength Al-Cu-Li-Ag-Mg alloy*. Scripta Metallurgica et Materialia, 1990. **24**(1): p. 79-84.

40. Kumar, K.S., S.A. Brown, and J.R. Pickens, *Effect of a prior stretch on the ageing response of an Al-Cu-Li-Ag-Mg-Zr alloy.* Scripta Metallurgica et Materialia, 1990. **24**(7): p. 1245-1250.
41. Kumar, K.S., S.A. Brown, and J.R. Pickens, *Microstructural evolution during ageing of an Al-Cu-Li-Ag-Mg-Zr alloy.* Acta Materialia, 1996. **44**(5): p. 1899-1915.
42. Chen, P.S. and B.N. Bhat, *Time-Temperature-Precipitation Behavior in Al-Li alloy* 2195. NASA thecnical report. Febraury 2002.
43. Chen, P.S. and W.P. Stanton, *Artificial Ageing Effects on Cryogenic Fracture Toughness of the Main Structural Alloy for the Super Lightweight Tank* February 2002
44. Chen, P.S. and W.P. Stanton, *A New Ageing Treatment for Improving Cryogenic Toughness of the Main Structural Alloy of the Super Lightweight Tank* Nov. 1996
45. Shukla, A.K. and W.A. Baeslack III, *Study of Microstructural evolution in friction-stir welded thin-sheet Al-Cu-Li alloy using transmission-electron microscopy.* Scripta Materialia, 2007, January. **56**: p. 513-516.
46. Rhodes, C.G., et al., *Effects of friction stir welding on microstructure of 7075 aluminum.* Scripta Materialia, 1997. **36**(1): p. 69-75.
47. *www.TWI.co.uk*
48. Mishra, R.S. and Z.Y. Ma, *Friction stir welding and processing.* Materials Science and Engineering: R: Reports, 2005. **50**(1-2): p. 1-78.
49. Mahoney, M.W., et al., *Proprieties of friction stir welded 7075 T651 aluminum.* Metallurgical and Material Transaction A, 1998. **29A**(1): p. 1955-1964.
50. Frigaard, Grong, and O.T. Midling, *A process model for friction stir welding and age hardening aluminium alloys.* Metallurgical and Material Transaction A, 2001. **32A**: p. 1189-1200.
51. Jariyaboon, M., et al., *The effect of welding parameters on the corrosion behaviour of friction stir welded AA2024-T351.* Corrosion Science, 2007. **49**(2): p. 877-909.
52. Hartley, D., *FSW Implementation on the Space Shuttle's External Tank* 2001.
53. *www.eclipseaviation.com*
54. Liu, G., et al., *Microstructural aspects of the friction-stir welding of 6061-T6 aluminum.* Scripta Materialia, 1997. **37**(3): p. 355-361.
55. Li, Y., L.E. Murr, and J.C. McClure, *Flow visualization and residual microstructures associated with the friction-stir welding of 2024 aluminum to 6061 aluminum.* Materials Science and Engineering A, 1999. **271**(1-2): p. 213-223.
56. McQueen, H.J., M. Cabibbo, and E. Evangelista, *Piercing / extrusion and FSW nugget microstructure formation in al alloys.* Material Science and Technology, 2007. **23**(7): p. 803-809.
57. Su, J.Q., et al., *Microstructural investigation of friction stir welded 7050-T651 aluminium.* Acta Materialia, 2003. **51**(3): p. 713-729.
58. Sato, Y.S., M. Urata, and H. Kokawa, *Parameters controlling microstructure and hardness during FSW of precipitation-hardenable aluminum alloy 6063.* Metallurgical and Material Transaction A, 2002. **33A**: p. 625-635.
59. Benavides, S., et al., *Low-temperature friction-stir welding of 2024 aluminum.* Scripta Materialia, 1999. **41**(8): p. 809-815.

60. Ma, Z.Y., R.S. Mishra, and M.W. Mahoney, *Superplastic deformation behaviour of friction stir processed 7075Al alloy.* Acta Materialia, 2002. **50**(17): p. 4419-4430.
61. Heinz, B. and B. Skrotzki, *Characterization of a Friction-Stir-Welded Aluminium Alloy 6013.* Metallurgical and Material Transaction B, 2002. **33B**: p. 489-498.
62. Jata, K.V., K.K. Sankaran, and J.J. Ruschau, *Friction-Stir Welding effect on Microstructure and Fatigue of Aluminium Alloy 7050-T7451.* Metallurgical and Material Transaction A, 2000. **31A**: p. 2181-2192.
63. Booth, D.P.P., M.J. Starink, and I. Sinclair, *Analysis of local microstructure and hardness of 13 mm gauge 2024-T351 AA friction stir welds.* Material Science and Technology, 2007. **23**(3): p. 276-284.
64. Schneider, J.A., et al., *TEM study of the FSW nugget in AA2195-T81.* Journal of Materials Science, 2005. **40**(16): p. 4341-4345.
65. Oertelet, G., et al., *Effect of Thermal Cycling on Friction Stir Welds of 2195 Aluminium Alloy.* Welding Research Supplement, 2001. **7-2001**: p. 71-79.
66. Lockwood, W.D., B. Tomaz, and A.P. Reynolds, *Mechanical response of friction stir welded AA2024: experiment and modeling.* Materials Science and Engineering A, 2002. **323**(1-2): p. 348-353.
67. Dechamps, A., *Personal communication - Voreppe June 2008 - A. Dechamps* 2008: Voreppe.
68. Sato, Y.S., et al., *Microstructural Evolution of 6063 Aluminium during Friction-Stir Welding.* Metallurgical and Material Transaction A, 1999. **30A**: p. 2429-2437.
69. Hatamleh, O., *Effects of peening on mechanical properties in friction stir welded 2195 aluminum alloy joints.* Materials Science and Engineering: A, 2008. **492**(1-2): p. 168-176.
70. Pouget, G. and A.P. Reynolds, *Residual stress and microstructure effects on fatigue crack growth in AA2050 friction stir welds.* International Journal of Fatigue, 2008. **30**(3): p. 463-472.
71. Vargel, C., *Corrosion of Aluminium*. First Edition ed. 2004: Elsevier.
72. *www.corrosion-doctor.org*
73. ASM, *Metals handbook. Vol. 13 - Corrosion*. Vol. 13. 1987: ASM International.
74. Ambat, R., et al., *Effect of iron-containing intermetallic particles on the corrosion behaviour of aluminium.* Corrosion Science, 2006. **48**: p. 3455-3471.
75. Muller, I.L. and J.R. Gavele, *Pitting potential of high purity binary aluminium alloys II. Al-Mg and Al-Zn alloys.* Corrosion Science 1977. **17**: p. 995-1007.
76. Birbilis, N. and R.G. Buchheit, Journal of the Electrochemical Society, 2005. **152**: p. B140-B151.
77. Schweitzer, P.A., *Fundamental of Metallic Corrosion* 2007: CRC Press.
78. Gavele, J.R. and S.M. De Micheli, *Mechanism of intergranular corrosion of Al-Cu alloys.* Corrosion Science, 1970. **10**: p. 795-807.
79. Ketcham, S.J. and I.S. Shaffer, *Exfoliation corrosion of aluminum alloys*. ASTM, STP, ed. ASTM. Vol. 516. 1972.
80. Kelly, D.J. and M.J. Robinson, *Influence of heat treatment and grain shape on exfoliation corrosion of Al-Li alloy 8090.* Corrosion 1993. **49**(10): p. 787-795.

81. Li, J.-f., et al., *Exfoliation corrosion and electrochemical impedance spectroscopy of an Al-Li alloy in EXCO solution.* Materials and Corrosion, 2007. **54**(4): p. 273-279.
82. Kertz, J.E., P.I. Gouma, and R.G. Buchheit, *Localized corrosion susceptibility of Al-Li-Cu-Mg-Zn alloy AF/C458 due to interrupted quenching from solutionizing temperatures.* Metallurgical and Material Transaction A, 2001. **32A**: p. 2561-2573.
83. Stoudt, M.R., A.K. Vasudevan, and R.E. Ricker, *Examination of the influence of lithium on the repassivation rate of aluminum alloy*. New Methods for Corrosion Testing of Aluminum Alloys, ASTM STP 1134. 1992, Philadelphia.
84. Niskanen, P., et al., *Corrosion of aluminum alloys containing lithium.* Corrosion Science, 1982. **22**(4): p. 283-293, 295-304.
85. Kumai, C., et al., *Influence of Ageing at 200 °C on the Corrosion Resistence of Al-Li and Al-Li-Cu alloys.* Corrosion, 1989. **45**(4): p. 294-302.
86. Wall, F.D. and G.E. Stoner, *The evaluation of the critical electrochemical potentials influencing environmentally assisted cracking of Al-Li-Cu alloys in selected environments.* Corrosion Science, 1997. **39**(5): p. 835-853.
87. Buchheit, R.G., J.P. Moran, and G.E. Stoner, *Electrochemical Behavior of the T1 Intermetallic Compound and its Role in Localized Corrosion of Al- 2% Li-3% Cu Alloys.* Corrosion, 1994. **50**(2): p. 120-130.
88. J. G. Rinker, J.G., M. Marek, and R.E. Sanders Jr., in *Aluminium-Lithium Alloys II*, J. E. A. Starke and J. T. H. Sanders, Editors. 1983: Monterey, California. p. 527.
89. Li, J.F., et al., *Corrosion mechanism associated with T1 and T2 precipitates of Al-Cu-Li alloys in NaCl solution.* Journal of Alloys and Compounds, 2007: p. 1-6.
90. Li, J.F., et al., *Study on localized corrosion mechanism of 2195 Al-Li alloy in 4.0% NaCl solution (pH 6.5) using a three-electrode coupling system.* Materials and Corrosion, 2005. **56**(3): p. 192-6.
91. Li, J.F., et al., *Simulation study on function mechanism of some precipitates in localized corrosion of Al alloys.* Corrosion Science, 2007. **49**: p. 2436-2449.
92. Li, J.-F., et al., *Simulation on function mechanism of T1(Al2CuLi) precipitate in localized corrosion of Al-Cu-Li alloys.* Transactions of Nonferrous Metals Society of China, 2006. **16**(6): p. 1268-1273.
93. Buchheit, R.G., J.P. Moran, and G.E. Stoner, *An anodic dissolution-based mechanism for the rapid cracking, "pre-exposure" phenomenon demonstrated by Al-Li-Cu alloys.* Corrosion, 1995. **51**(6): p. 417-428.
94. Buchheit, R.G., J.P. Moran, and G.E. Stoner, *Measurements and Mechanisms of Localized Aqueous Corrosion in Aluminum-Lithium Alloys*. 1994.
95. Li, H., et al., *Effect of ageing time on strength and microstructures of an Al-Cu-Li-Zn-Mg-Mn-Zr alloy.* Materials Science and Engineering: A, 2008. **498**(1-2): p. 314-320.
96. Liang, W., et al., *Effect of ageing on the mechanical properties and corrosion susceptibility of an Al-Cu-Li-Zr alloy containing Sc.* Rare Metals, 2008. **27**(2): p. 146-152.
97. Meletis, E.I., *Microstructure and Stress-Corrosion Cracking Relationship in an AI-Li-Cu-Zr Alloy.* Materials Science and Engineering, 1987. **93**(235-245).
98. Li, H.-y., et al., *Exfoliation corrosion of T6- and T8-aged AlxCuyLiz alloy.* Transactions of Nonferrous Metals Society of China, 2008. **18**(4): p. 778-783.

99. Lumsden, J.B., et al., *Intergranular corrosion following friction stir welding of aluminium alloy 7075-T651*. Corrosion, 1999. **55**(12): p. 1127-1135.
100. Wadeson, D.A., et al., *Corrosion behaviour of friction stir welded AA7108 T79 aluminium alloy*. Corrosion Science, 2006. **48**(4): p. 887-897.
101. Paglia, C.S. and R.G. Buchheit, *The time-temperature-corrosion susceptibility in a 7050-T7451 friction stir weld*. Materials Science and Engineering A, 2008. **492**(1-2): p. 250-254.
102. Padgett, B.N., C.S. Paglia, and R.G. Buchheit, *Characterization of Corrosion Behavior in Friction Stir Weld Al-Li-Cu AF/C458 Alloy*, in *Symposium on Friction Stir Welding and Processing II*. 2003: SAN DIEGO CALIFORNIA
103. Corral, J., et al., *Corrosion of friction-stir welded aluminum alloys 2024 and 2195*. JOURNAL OF MATERIALS SCIENCE LETTERS, 2000. **19**: p. 2117-2122.
104. ASTM, *Standard Pratice for Evaluating Intergranular Corrosion Resistance of Heat Treatable Aluminum Alloy by Immersion in Sodium Chloride + Hydrogen Peroxide Solution* in *G110 - 92*. 2003.
105. Padovani, C., *Corrosion Protection of Friction Stir Welds in Aerospace Aluminium Alloys*, in *Metallurgy and Materials*. 2007, University of Birmingham: Birmingham.
106. Jata, K.V. and S.L. Semiatin, *Continuous dynamic recrystallization during friction stir welding of high strength aluminum alloys*. Scripta Materialia, 2000. **43**(8): p. 743-749.
107. Sutton, M.A., et al., *Microstructural studies of friction stir welds in 2024-T3 aluminum*. Materials Science and Engineering A, 2002. **323**(1-2): p. 160-166.
108. Reynolds, A.P., et al., Science and Technology of Welding and Joining, 2005. **10**(2): p. 190-199.
109. Reynolds, A.P., *Understanding Process and Property Relationships in Aluminum Alloy Friction Stir Welds*. Materials Science Forum 2007. **539-543**: p. 207-214.
110. ASM, *Metals handbook. Vol. 2 - Properties and selection: nonferrous alloys and special-purpose materials*. Vol. 2. 1990: ASM International.